

**IONIZING-RADIATION-INDUCED COLOR CENTERS IN YAG,
ND:YAG, AND CR:ND:YAG:
DEVELOPING AND ANALYZING A RADIATION-HARD LASER
GAIN MEDIUM**

by
Boris L. Glebov

A Dissertation Submitted to

COLLEGE OF OPTICAL SCIENCES

In Partial Fulfillment of the Requirements
for the degree of

DOCTOR OF PHILOSOPHY

In the Graduate College of
THE UNIVERSITY OF ARIZONA

2010

**THE UNIVERSITY OF ARIZONA
GRADUATE COLLEGE**

As members of the Dissertation Committee, we certify that we have read the dissertation prepared by Boris L. Glebov entitled Ionizing-Radiation-Induced Color Centers in YAG, Nd:YAG, and Cr:Nd:YAG: Developing and Analyzing a Radiation-Hard Laser Gain Medium, and recommend that it be accepted as fulfilling the dissertation requirement for the Degree of Doctor of Philosophy.

Kelly S. Potter (11/16/2010)
Joseph H. Simmons (11/16/2010)
Harold Parks (11/16/2010)

Final approval and acceptance of this dissertation is contingent upon the candidate's submission of the final copies of the dissertation to the Graduate College. I hereby certify that I have read this dissertation prepared under my direction and recommend that it be accepted as fulfilling the dissertation requirement.

Dissertation Director: Kelly S. Potter (11/16/2010)

STATEMENT BY AUTHOR

This dissertation has been submitted in partial fulfillment of requirements for an advanced degree at The University of Arizona and is deposited in the University Library to be made available to borrowers under rules of the Library.

Brief quotations from this dissertation are allowable without special permission, provided that accurate acknowledgement of source is made. Requests for permission for extended quotation from or reproduction of this manuscript in whole or in part may be granted by the head of the major department or the Dean of the Graduate College when in his or her judgment the proposed use of the material is in the interests of scholarship. In all other instances, however, permission must be obtained from the author.

SIGNED: Boris L. Glebov

DEDICATION

This is dedicated to my loving parents and my dear friends.

*Without you, this would have been nothing
but a sad and lonely whimper.*

Thank you.

TABLE OF CONTENTS

List of Figures	8
List of Tables	14
Abstract	16
Chapter 1: Introduction	16
1.1. Research objectives	17
1.2. Choice of experimental conditions	15
1.2.1. Primary test	17
1.2.2. Secondary tests	18
Chapter 2: Literature Review	26
2.1. Development of YAG material	28
2.2. Development of Nd:YAG and Cr,Nd:YAG lasers	33
2.3. Review of work on color centers in YAG	37
2.4. Summary of background information	46
Chapter 3: Experimental Sample Suite	48
3.1. Origin and physical description of samples	49
3.2. Optical absorption spectroscopy	52
3.2.1. Method	52
3.2.1.1. Physical setup and data collection	52
3.2.1.2. Sources and mitigation of error – sample positioning	56
3.2.1.3. Sources and mitigation of error – instrumental “steps” and “stitching”	57
3.2.2. Results and discussion	59
3.2.2.1. Undoped YAG	60
3.2.2.2. Nd:YAG	61
3.2.2.3. Cr ³⁺ :YAG	64
3.2.2.4. Cr,Nd:YAG	69
3.3. Mass spectroscopy	71
3.3.1. Method	72
3.3.1.1. Glow-discharge mass spectroscopy	72
3.3.1.2. Secondary ionization mass spectroscopy	76
3.3.1.3. Combining GDMS and SIMS data	81
3.3.1.4. Uncertainty of reported data	82
3.3.2. Results and discussion	83
Chapter 4: Results of Gamma Irradiation at HERMES III	85
4.1. Method	86
4.1.1. Experimental setup at HERMES III	86
4.1.1.1. Description of HERMES III	87
4.1.1.2. Physical setup	88
4.1.1.3. Data collection	94
4.1.1.4. Data processing	95
4.1.1.5. Modified Savitzky-Golay smoothing algorithm	98
4.1.2. Differential absorption spectroscopy	99

TABLE OF CONTENTS, continued

4.2. Data and results from HERMES III	101
4.2.1. Transient response to gamma irradiation	102
4.2.1.1. Undoped YAG	102
4.2.1.2. Nd:YAG	107
4.2.1.3. Cr ³⁺ :YAG	114
4.2.1.4. Cr ³⁺ ,Nd:YAG	116
4.2.2. Permanent response to gamma irradiation	120
4.2.2.1. Undoped YAG	120
4.2.2.2. Nd:YAG	122
4.2.2.3. Cr ³⁺ ,Nd:YAG	124
4.3. Data analysis	128
4.3.1. Correlation of dose and induced absorption	129
4.3.1.1. Undoped YAG	131
4.3.1.2. Nd:YAG	134
4.3.2. Modeling of transient response	136
4.3.2.1. Undoped YAG	137
4.3.2.2. Nd:YAG	141
4.3.2.3. High-chromium Cr ³⁺ ,Nd:YAG	148
4.3.2.4. Low-chromium Cr ³⁺ ,Nd:YAG	150
4.3.3. Summary of numerical data analysis	152
4.4. Discussion	155
4.4.1. Identification of radiation-hard composition	155
4.4.2. Physical interpretation of observations	157
4.4.2.1. Identification of <i>F</i> -type centers	158
4.4.2.2. Identification of <i>Fe</i> ³⁺ / <i>Fe</i> ²⁺ conversion	162
4.5. Conclusions	166
Chapter 5: Results of UV Irradiation Tests	168
5.1. Method	170
5.1.1. Experimental setup of the UV/NIR Pump/Probe test	170
5.1.1.1. Physical setup	171
5.1.1.2. Data collection	179
5.1.1.3. Data processing	180
5.1.1.4. Data accuracy	181
5.2. Data and results	182
5.2.1. Transient response to UV irradiation	183
5.2.1.1. Undoped YAG	183
5.2.1.2. Nd:YAG	186
5.2.1.3. Cr ³⁺ :YAG	188
5.2.1.4. Cr ³⁺ ,Nd:YAG	191

TABLE OF CONTENTS, continued

5.2.2. Permanent response to UV irradiation:	193
5.2.2.1. Undoped YAG	193
5.2.2.2. Nd:YAG	196
5.2.2.3. Cr ³⁺ :YAG, Cr ³⁺ ,Nd:YAG	198
5.3. Numerical data analysis	199
5.3.1. Correlation of fluence and induced absorption	200
5.3.2. Re-examination of HERMES III Cr ³⁺ :YAG data	202
5.3.2.1. Method of quasi-derivatives	203
5.3.2.2. Results of analysis	205
5.4. Interpretation and discussion	210
5.4.1. Physical interpretation of data	211
5.4.1.1. Identification of Cr ⁴⁺ centers	211
5.4.2. Comparison with HERMES III transient data	215
5.4.2.1. Undoped YAG	216
5.4.2.2. Nd:YAG	219
5.4.2.3. Cr ³⁺ :YAG	222
5.4.2.4. Cr ³⁺ ,Nd:YAG	223
5.4.3. Comparison with HERMES III permanent data	225
5.4.3.1. Undoped YAG and Nd:YAG	225
5.4.3.2. Cr ³⁺ :YAG and Cr ³⁺ ,Nd:YAG	229
5.5. Conclusions	230
Chapter 6: Conclusions	233
6.1. Summary and review of results	234
6.2. Proposed mechanism of radiation hardness	236
6.3. Future work	240
6.4. Report summary and conclusions	242
References	244

LIST OF FIGURES

- FIGURE 2.1. Relative arrangement of the cation sites in YAG. Letter indices (*a*, *c*, *d*) refer to the cation site designations. Numerical indices refer to specific anion-anion distances (see Table 2.1). (Reproduced from Euler and Bruce 1965, Figure 1.)_____ 29
- FIGURE 2.2. Absorption induced in a YAG sample via x-ray irradiation at 77 K. Of importance are curves 1 and 4. Curve 1 is actual absorption at 77 K. Curve 4 is actual absorption at room temperature. (Figure reproduced from Bernhardt 1976, Figure 1.)__ 41
- FIGURE 3.1. Schematic layout of the optical spectrometer (Perkin Elmer Lambda 950) used in these experiments. Diagram based on the technical documents shipped with the instrument. _____ 53
- FIGURE 3.2. Thickness-normalized absorbance of undoped YAG samples. “AL” stands for Airtron-Litton. ”SM” stands for Scientific Materials. Labels “avg” and “high” refer to relative purity of the sample. _____ 60
- FIGURE 3.3. Representative optical absorption spectra of various Nd:YAG compositions. A: 0.5 at% Nd:YAG from United Crystals. B: 1.0 at% Nd:YAG from Scientific Materials. C: 1.2 at% Nd:YAG from United Crystals. Number labels in A refer to groups of transitions associated with Nd level structure. These associations are listed in Table 3.1. _____ 61
- FIGURE 3.4. Representative optical absorption spectra of various Nd:YAG compositions. A: 0.5 at% Cr:YAG from United Crystals. B: 1.5 at% Cr:YAG from Scientific Materials. C: 2.0 at% Cr:YAG from United Crystals. Number labels in A refer to specific transitions of the Cr_{oct}^{3+} ions. These transitions are listed below in Table 3.2. _____ 64
- FIGURE 3.5. Absorption observed in a nominally Cr^{3+} :YAG sample in the NIR. _____ 67
- FIGURE 3.6. An example of Cr_{tet}^{4+} optical absorption bands. A comparison of the group of bands near 10,000 1/cm to the bands shown in Figure 3.5 supports the assignment of these bands to Cr_{tet}^{4+} . (Figure reproduced from Feldman et al. 2003.) _____ 67
- FIGURE 3.7. Representative optical absorption spectra of various Cr, Nd:YAG compositions. A: 0.13 at% Cr, 1.0 at% Nd:YAG from Airtron-Litton. B: 0.5 at% Cr, 1.0 at% Nd:YAG from Scientific Materials. C: 1.0 at% Cr, 1.2 at% Nd:YAG from Scientific Materials. _____ 70

LIST OF FIGURES, continued

- FIGURE 3.8. A general schematic representing operation of Glow Discharge Mass Spectrometer. _____ 72
- FIGURE 3.9. Schematic representation of a Secondary Ionization Mass Spectrometer.
_____ 76
- FIGURE 4.1. Experimental setup in the shielded room at HERMES III. _____ 90
- FIGURE 4.2. Experimental setup in the test cell at HERMES III. _____ 91
- FIGURE 4.3. Time dependence of absorption at 1064 nm in undoped YAG induced by a single fast pulse of 2 MeV photons. A – data presented in the relative transmittance form. B – data recalculated as induced coefficient of absorption. _____ 102
- FIGURE 4.4. Time dependence of absorption at 1064 nm in undoped YAG induced by a single fast pulse of 2 MeV photons, presented on shorter time scales. Plots **A** and **B** are presented on linear-linear scales, while plot **C** is presented as log-linear. _____ 104
- FIGURE 4.5. Time dependence of absorption at 1064 nm in Nd:YAG samples induced by a single fast pulse of 2 MeV photons. Figures **A** and **B** present the data on two different time scales. “UC” stands for United Crystals, while “SM” stands for Scientific Materials. _____ 107
- FIGURE 4.6. Different modes of behavior observed in the United Crystals Nd:YAG samples. The difference is the relatively negative deviation observed most clearly from the onset of absorption and until approximately 0.2 ms. Data curve labels refer to specific samples of the same nominal composition. **A**: 0.5 at% Nd:YAG. **B**: 1.2 at% Nd:YAG.
_____ 110
- FIGURE 4.7. Log-linear plots of the induced absorption curves from Nd:YAG samples in response to an individual pulse of 2 MeV photons. Samples and data are the same as used in Figure 4.6. _____ 112
- FIGURE 4.8. Time dependence of absorption at YAG samples doped with various quantities of Cr. Oscillations in the 1.5 at% Cr:YAG sample (light grey curve in the background) are attributed to instrumental noise. _____ 114
- FIGURE 4.9. Time dependence of absorption at 1064 nm Cr, Nd:YAG samples induced by a single fast pulse of 2 MeV photons. Reported negative absorption corresponds to induced gain at 1064 nm. **A**: Data on the seconds scale. **B**: Data on the milliseconds scale. _____ 117

LIST OF FIGURES, continued

- FIGURE 4.10. A log-linear plot of the data from Figure 4.9. Induced absorption response of Cr,Nd:YAG samples to a pulse of 2 MeV photons. _____ 118
- FIGURE 4.11. Differential absorption spectroscopy data showing permanent induced absorption in undoped YAG samples due to gamma irradiation at HERMES III. _____ 121
- FIGURE 4.12. Differential absorption induced in Nd:YAG samples by gamma irradiation at HERMES III. _____ 122
- FIGURE 4.13. Differential absorption in Cr,Nd:YAG due to pulsed gamma irradiation at HERMES III. _____ 125
- FIGURE 4.14. Sampling of differential absorption induced by gamma irradiation in a Scientific Materials Cr,Nd:YAG sample. The three regions tested had differing amount of striations detected, with the core region most heavily affected, and the outer region least affected. _____ 126
- FIGURE 4.15. False-color representation of a shadow image of a Scientific Materials co-doped Cr,Nd:YAG sample. Blue represents dark regions, red represents the bright, and black represents no change in brightness. Central core and radial striations are clearly visible indicating radial variation in the index of refraction of the sample. _____ 127
- FIGURE 4.16. A plot of $\Delta\alpha$ (summed over the first 0.2 ms) vs. shot dose. Data points correspond to the three samples tested – Airtron-Litton (AL), Scientific Materials average purity (SM avg), Scientific Materials high purity (SM high). A general positive correlation between induced absorption and dose are noted. _____ 132
- FIGURE 4.17. Experimental data from undoped YAG (SM, avg) and its model are compared on two different time scales. A: compliance with the slow process. B: compliance with the fast process. _____ 139
- FIGURE 4.18. Examples of the three modes of behavior used in modeling of the transient response data. The black curve represents the slow absorption process. The dark gray curve exhibits both the slow and the fast processes. The light gray curve includes all three components – fast and slow absorption processes, as well as the gain process. These traces are actual experimental data. “Slow” and “Slow, Fast”: 1.2 at% Nd:YAG (UC) (two different samples). “Slow, Fast, Gain”: 0.5 at% Nd:YAG (UC). _____ 142
- FIGURE 4.19. Experimental data and its model are compared on two different time scales. A: compliance with the slow process. B: compliance with the fast process. Fits are based on a 1.2 at% Nd:YAG (UC) sample. _____ 144

LIST OF FIGURES, continued

- FIGURE 4.20. Experimental data and the model are compared on two different time scales. A: compliance with the slow process. B: compliance with the fast and the gain process. Fits are based on a 0.5 at% Nd:YAG (UC) sample. _____ 146
- FIGURE 4.21. Thermoluminescence of nominally pure undoped YAG exposed to x-rays at liquid nitrogen temperature. Dashed and solid lines represent results of different experiments. Observation carried out at two wavelengths (644 nm and 775 nm). (Reproduced from Bernhardt 1976) _____ 159
- FIGURE 4.22. Thermoluminescence of several materials exposed to x-rays at 10 K. Curves are artificially vertically offset. Curves obtained by integrating wavelength-resolved measurements from 280 nm to 715 nm. (Reproduced Vedda et al. 2004) _____ 160
- FIGURE 4.23. Differential absorption for an undoped YAG sample irradiated with an unfiltered xenon flash lamp. Solid line indicates the spectrum. Dashed lines represent modeled components. (Reproduced from K. Mori 1977). _____ 162
- FIGURE 4.24. Differential absorption for an undoped YAG sample. Changes induced by a reducing anneal. (Reproduced from Akhmadulin et al. 1992). _____ 163
- FIGURE 5.1. Physical layout of the UV/NIR Pump/Probe experiment. _____ 172
- FIGURE 5.2. Main circuit diagram of the analog mixer used in the UNPP experiment. GND_isol connects to an isolated ground reference, shown in Figure 5.3. _____ 175
- FIGURE 5.3. The isolated ground sub-circuit of the analog mixer device. _____ 176
- FIGURE 5.4. Induced absorption at 1064 nm due to a pulse of UV in undoped YAG samples. _____ 184
- FIGURE 5.5. A log-linear plot of data from Figure 5.4. _____ 185
- FIGURE 5.6. Induced absorption at 1064 nm due to a pulse of UV in Nd:YAG. _____ 186
- FIGURE 5.7. A log-linear plot of the data from Figure 5.5. _____ 187
- FIGURE 5.8. Induced absorption at 1064 nm due to a pulse of UV in Cr:YAG. _____ 188
- FIGURE 5.9. Differential absorption induced in 0.5 at% Cr³⁺:YAG (UC) by irradiating with 248 nm UV light. Spectrum taken approximately five minutes after exposure. _____ 189

LIST OF FIGURES, continued

- FIGURE 5.10. Induced absorption at 480 nm due to UV irradiation in Cr:YAG. Origin of the time axis corresponds to the end of UV irradiation. _____ 190
- FIGURE 5.11. Induced absorption at 1064 nm due to a pulse of UV in Cr,Nd:YAG. Negative induced absorption indicates gain. _____ 191
- FIGURE 5.12. Transient differential absorption in Cr,Nd:YAG samples due to pulsed UV irradiation at 248 nm. _____ 192
- FIGURE 5.13. Differential absorption in undoped YAG due to pulsed UV irradiation at 248 nm. Data shown are from an Airtron-Litton sample (black curve), average purity Scientific Materials sample (dark gray curve), and the high-purity Scientific Materials sample (light gray curve). Data for the YAG (SM high) sample was vertically shifted to compensate for an erroneous offset in the raw data. _____ 194
- FIGURE 5.14. Additional absorption in Nd:YAG due to pulsed UV irradiation at 248 nm. _____ 197
- FIGURE 5.15. Dependence of maximum UV-induced absorption in 0.5 at% Nd:YAG (UC) on pulse energy of the UV laser. _____ 201
- FIGURE 5.16. Quasi-derivatives calculated for 0.5 at% Cr:YAG (UC). Averaging included 200 data points (approximately 0.4 ms). _____ 206
- FIGURE 5.17. Normalized quasi-derivative for 1.5 at% Cr:YAG (SM). _____ 207
- FIGURE 5.18. Normalized quasi-derivative for 2.0 at% Cr:YAG (UC). _____ 208
- FIGURE 5.19. UV-induced differential absorption in chromium-bearing YAG samples. "AL" stands for Airtron-Litton, "SM" for Scientific Materials, and "UC" for United Crystals, referring to the sample manufacturer. _____ 212
- FIGURE 5.20. Experimental data and the model for absorption in 0.5 at% Cr:YAG. Peak positions from Feldman et al. (2003). Fit peak positions: 482 nm, 406 nm, 361 nm. Peaks were modeled as Gaussians. Positions were fixed, while widths and amplitudes were left adjustable. _____ 213
- FIGURE 5.21. Relative comparison of UV and gamma transient induced absorption data. UV data, shown in black, is from the same sample Airtron-Litton sample as the gamma data shown in dark gray. Scientific Materials sample of average purity is shown in light gray. _____ 216

LIST OF FIGURES, continued

- FIGURE 5.22. Samples and data set are the same as in Figure 5.20, but presented on a shorter time scale. _____ 217
- FIGURE 5.23. A side-by-side comparison of UV and gamma irradiation tests. Data were scaled and then normalized to appear on the same scale. _____ 219
- FIGURE 5.24. Same data as in Figure 5.23. A shorter time scale is used to highlight behavior near the irradiation event. Data for gamma irradiation of 0.5 at% Nd:YAG has been omitted from this figure. _____ 221
- FIGURE 5.25. Comparison of transient response data for the co-doped samples, from two types of irradiation. The Airtron-Litton (AL) sample's composition was 0.13 at% Cr, 1.0 at% Nd:YAG. The Scientific Materials (SM) sample's composition was 1.0 at% Cr, 1.2 at% Nd:YAG. _____ 223
- FIGURE 5.26. Comparison of room-temperature-stable differential absorption in undoped YAG due to gamma irradiation (the black curve) and UV (the light gray curve). Data used are from the Scientific Materials sample of average purity. _____ 225
- FIGURE 5.27. Comparison of the amplitude of induced permanent changes in undoped YAG samples, plotted against concentration of the iron impurity. _____ 227
- FIGURE 5.28. Comparison of room-temperature-stable differential absorption in Nd:YAG due to gamma irradiation (the black curve) and UV (the light gray curve). Data used are from the United Crystals samples doped with 0.5 at% Nd. _____ 228

LIST OF TABLES

- TABLE 2.1. Calculated cation-anion (segments 4, 6, 8) and anion-anion (all other segments) distances in a nominal YAG cell. Segment numbers refer to labels in Figure 2.1 above. (Data reproduced from Euler and Bruce 1965, Table 4.) _____ 29
- TABLE 2.2. List of ions commonly doped into YAG crystals. **Note 1:** Chromium ions only occupy the tetravalent state in presence of divalent charge compensators, such as Mg^{2+} or Ca^{2+} . **Note 2:** Iron only occupies the divalent state in presence of tetravalent charge compensators, such as Si^{4+} . _____ 30
- TABLE 2.3. Values of ionic radii for several atomic species for various coordination numbers. **Note 1:** as several estimations were available for the ionic radii, values provided here are averages. Values are omitted for coordination sites not occupied by the given ion. (Data reproduced from Shannon and Prewitt 1969.) _____ 32
- TABLE 3.1. Some of the Nd optical transitions that can be identified in the samples' optical absorption spectra. Label # column refers to the labels in Figure 3.3A. Transitions are between the indicated states and the ground state ($^4I_{9/2}$). _____ 63
- TABLE 3.2. Optical transitions that can be identified in the optical absorption spectra of the Cr:YAG samples. Numbers refer to the labels in Figure 3.4A. These transitions initiate in the ground state (4A_2). (Wood 1963, Feldman 2003) _____ 66
- TABLE 3.3. Tabulated results of GDMS analysis of a sample taken from a crystal boule grown by Scientific Materials Corp. **Note 1:** aluminum, oxygen, and yttrium were listed as major constituents, and therefore not tracked in this analysis. **Note 2:** the elements marked in bold were considered especially relevant, and special attention was paid to tracking their concentrations in the SIMS data (see Section 3.3.1.3 below) **Note 3:** GDMS is intended for trace analysis, therefore its reporting of elements present in high concentrations is unreliable. _____ 74
- TABLE 3.4. Integrated signal values from SIMS data for several representative samples. Where values are omitted, integration was not performed because signal was indistinguishable from background. Values in boldface indicate that background was subtracted from this number. _____ 79
- TABLE 3.5. Concentrations (in ppma) of various contaminants in the experimental sample suite. Data were derived from a combination of SIMS and GDMS tests. **Note 1:** the element is below the detectability threshold in the particular sample. **Note 2:** values for this sample from the GDMS test. All other samples' values are from the SIMS test. **Note 3:** "AL" stands for Airtron-Litton. **Note 4:** "SM" stands for Scientific Materials. **Note 5:** "UC" stands for United Crystals. _____ 83

LIST OF TABLES, continued

TABLE 4.1. Oscilloscope settings. _____	94
TABLE 4.2. A summary of the extrema of induced absorption in undoped YAG samples, along with the total dose received by these samples. Minima are stated for the wavelengths above 230 nm. _____	121
TABLE 4.3. A summary of the extrema of induced absorption in undoped YAG samples, along with the total dose received by these samples. _____	123
TABLE 4.4. P-correlation values for undoped YAG, describing dependence of induced absorption on shot dose. _____	131
TABLE 4.5. Correlation values between indicated sums over data points for given samples and corresponding shot doses. _____	134
TABLE 4.6. Averaged results of modeling transient response of undoped YAG samples to pulses of gamma radiation. Material labels correspond to those used previously, as in Figure 4.3. Variable labels correspond to those used in Equation 4.11. _____	140
TABLE 4.7. Average values of model fitting parameters describing transient response of Nd:YAG samples to pulsed gamma radiation. 1.2 at% Nd:YAG samples S01 and S18 had a negligible gain contribution, 1.2 at% Nd:YAG sample S02 was used as the slow process reference; none of the other components were fitted to its data. _____	147
TABLE 4.8. Average values of model fitting parameters describing transient response of high-chromium Cr, Nd:YAG samples to pulsed gamma radiation. _____	149
TABLE 4.9. Average values of model fitting parameters describing transient response of low-chromium Cr, Nd:YAG (AL) samples to pulsed gamma radiation. _____	151
TABLE 4.10. Summary of fitting results from modeling of the transient response of materials tested at HERMES III. Crossed-out cells corresponded to values not used to fit the particular composition. The sample used as a reference data set in the modeling of the Nd:YAG data was omitted from this table. _____	153
TABLE 5.1. Comparison of fitting results from the fit presented in Figure 5.19 and those published by Feldman et al. In the fitting procedure used here, band positions were fixed, while peak amplitude and widths were varied. _____	213

ABSTRACT

This report presents results from a series of experiments in which YAG samples (undoped, as well as doped with Nd and Cr³⁺) were exposed to ionizing radiation (gamma rays and UV). These experiments were performed for the purpose of investigating the various photodarkening processes taking place in these materials in response to the ionizing radiation. The purpose of this investigation was to establish whether and how co-doping YAG with Cr³⁺ improves the material's resistance to photodarkening due to the ionizing radiation. The experiments tracked time-resolved transmittance of the samples at 1064 nm in immediate response to a pulsed exposure to the ionizing radiation, as well as steady-state spectrally-resolved changes in the samples' optical absorption after the irradiation. The investigation revealed a number of photodarkening processes occurring in the samples in response to the ionizing radiation, both transient and permanent. It was further revealed that inclusion of Cr³⁺ ions in YAG significantly reduces these photodarkening processes, improving the material's radiation resistance. It was observed that materials containing at least 0.5 at% Cr³⁺ are essentially radiation-hardened, resisting both transient and steady-state changes in transmittance observed in the materials not containing Cr³⁺.

Chapter 1 - Introduction

Section 1.1

Research Objectives

The increased penetration of technology into an ever-widening range of environments is a hallmark of the modern era. This means that devices of increasing complexity and function are introduced into more and more aggressive environments, where they are expected to survive and continue to operate for extended periods of time. Consequently, there is a constant need to improve the robustness of technologies so deployed.

One such environment, in which there has been a rapid proliferation of optical devices and components in recent years, and which presents harsh ionizing radiation conditions for device operation, is the Earth orbit. Applications of optics technologies such as remote sensing, communication, and data storage are some of the most common in space-borne devices.

Ionizing radiation presents a fundamental difficulty for optical devices because many optical materials, such as glasses and crystals, fail in such an environment. The most common mode of failure is loss of transmission (radiation-induced photodarkening) via color center formation.

Formation of color centers can be summarized in the following model. When an ion interacts with ionizing radiation, one of its electrons is removed into the conduction band of the material. This creates an excited electron and a hole. If the electron and its hole recombine, then the band structure of the material is unchanged. However, it is

possible for either the electron or the hole to become stabilized in a different location. In this case, there is one ion which has gained an electron (electron trap), and one which has lost an electron (hole trap). In both cases, the ions' charge distribution – and, accordingly, their band structure – changes, thus resulting in changes in the material's polarizability and frequently in corresponding changes in the material's optical absorption properties. This introduces parasitic absorption, and generally leads to loss of transmittance across portions of the optical spectrum. Clearly, an optical element whose transmission has been reduced has the potential to impact component performance to the extent that the whole system may malfunction or cease functioning altogether.

The prevention of color center formation, then, becomes a fundamental problem to be solved if the exploration and utilization of outer space is to continue and expand. There is a need to develop systems that are radiation-hardened, and this means developing radiation-hard materials.

In expanding utilization of a given new area, it is preferable to use technologies already available, but applied in a new context. Wide adoption of a technology requires methods that are commercially available – an approach frequently termed “Commercial Off The Shelf” (COTS) technology. This means that solutions proposed must be based on existing materials and technologies in order to be readily adopted. Therefore, rather than synthesizing a wholly new material, the research focuses on optical material systems that are already known.

The particular subset of the general “optical devices” category addressed in the present work is laser gain medium materials. Radiation-induced increases in loss in the

gain medium of a laser lead to increased operating threshold, decreased lasing efficiency, and excessive heating. In turn, these can lead to power overload issues, thermal breakdown, and complete cessation of lasing.

One of the most common solid-state laser materials employed today is Yttrium Aluminum Garnet doped with Neodymium (Nd:YAG). This material system has been known since 1964 (Geusic), and continues to be widely used today. Usually emitting at 1064 nm, Nd:YAG lasers have high efficiency, narrow-band operation without the need for external wavelength stabilization, and YAG itself provides good mechanical, and optical characteristics (Geusic et al. 1964). Furthermore, production technology for this material is well established, contributing to the material's lasting appeal. However, previous work has shown Nd:YAG to suffer from radiation-induced darkening (Bass and Paladino 1967, Compton and Cesena 1967).

The majority of work to date has dealt with the observation of color-center formation and the identification of the underlying physical processes involved. However, some previously published reports suggest that co-doping Nd:YAG with Cr^{3+} (Rose et al. 1995) can, in fact, increase this material's radiation hardness. Similar to Nd:YAG, Cr,Nd:YAG is also a material that has been known for a long time (Kiss and Duncan 1964), though its radiation-resistive properties have not received wide attention. The co-doped material has been popular since early in the history of the use of Nd lasers because of the ability of the Cr^{3+} dopant to significantly increase the gain medium pumping efficiency relative to singly-doped (Nd:YAG) material as a result of a $\text{Cr}^{3+} \rightarrow \text{Nd}^{3+}$ energy transfer mechanism (Kiss and Duncan 1964, Murphy et al. 1964).

The objective of the current research is to further examine behavior of Cr,Nd:YAG in an ionizing radiation environment, and to refine our understanding of how the addition of chromium increases the material's radiation resistance. Specifically, this will be done by investigating the materials' behavior in response to gamma and UV modes of irradiation, where the response will be defined in terms of changes in the material's optical absorption, both permanent and transient. The effectiveness of the chromium co-doping will be examined in comparison to YAG materials not doped with chromium.

Section 1.2

Choice of Experimental Conditions

A number of researchers who have previously studied the effects of ionizing radiation on Nd:YAG have observed that common types of radiation (both particle and high-energy photon) produce similar changes in the material (Compton and Cesena 1964, Mori 1973, Bernhardt 1976, Karaseva et al. 1985). Primarily, what they found is that changes in the material that are relevant to its optical properties are confined to the creation of color centers via trapped holes and ionized electrons. The effects of gamma irradiation on Nd:YAG-based devices are of a particular interest when extraterrestrial applications are considered. This is largely because energetic particle radiation is easier to shield than gamma radiation and also because the interaction of energetic particles with shielding materials is known to produce secondary gamma rays, making gamma exposure a significant concern in space environments. Therefore, the focus of the present study will be on effects of gamma radiation.

Previous work by other research groups that studied the effects of gamma radiation analyzed only the post-irradiation condition of the material (e.g., Bass and Paladino 1967, Compton and Cessena 1967, Mori 1977; see Section 2.3 for a more complete review of previous studies). The dynamic response of Nd:YAG during irradiation by high-energy photons has not previously been studied. The current work, therefore, will report on the use of pulsed irradiation sources, combined with novel experimental techniques, in the examination of both the in-situ and the post-irradiation effects arising in optical materials due to ionizing radiation.

Tracking changes in the broad optical absorption spectrum of a material can be challenging, especially in presence of intense pulsed gamma radiation. However, as Compton and Cesena (1967) point out, most of performance degradation of Nd:YAG is due to absorption at the lasing wavelength, not due to changes in excited state lifetimes or absorption at the pumping wavelength. Hence we can limit measurements of dynamic response to absorption at the main lasing wavelength – 1064 nm.

Section 1.2.1

Primary Test

Tests of the response of YAG-based laser materials to the pulsed ionizing radiation consist of the in-situ observation of the dynamics of the material's transmittance at 1064 nm. If the co-doped materials exhibits losses similar to those of undoped YAG or of singly-doped Nd:YAG, then we can conclude that the material modification offers no significant benefits. However, if the reduction in transmittance is noticeably less for the co-doped material, then this serves as evidence of useful improvement in material radiation hardness.

Measurements carried out at the HERMES III facility at Sandia National Laboratory, described in detail in the Experiment section of Chapter IV (Section 4.1.1), fit these requirements. These experiments measured in-situ sample transmittance at 1064 nm, providing exactly the information that would strongly indicate whether a given material is radiation-hard within the boundaries of this research.

Section 1.2.2

Secondary Tests

Experiments at HERMES III, while providing the most direct and authentic test of the materials, had practical constraints on what kind of data could be collected, and how the experiment could be modified. Hence, there was a need to design an experiment that would collect similar data, but that was suitable for routine use under conditions that could be more finely controlled. This experiment was the ultraviolet-near-infrared (UV/NIR) Pump-Probe experiment (described in detail in Chapter V, Section 5.1.1). This experiment collected the same data as the HERMES III experiment, except the source of ionizing radiation was a pulsed UV laser. This platform was also used to collect data on a system being simultaneously pumped and irradiated with ionizing radiation.

A survey of the literature shows that the various color centers that can arise in YAG due to ionizing radiation have different spectroscopic absorption signatures and correspond to some very specific contaminants. For this reason, it is further useful to track changes in materials' stable optical absorption and composition. The former was measured using a UV-Vis spectrometer. The latter was evaluated using Secondary Ionization Mass Spectroscopy (SIMS) and Glow-Discharge Mass Spectroscopy (GDMS) techniques, which can identify contaminants with concentrations as low as 1 atomic ppm (ppma).

The combination of these experiments allowed for identification of specific impurities and color centers in the samples. This information expanded on the induced absorption data collected at the lasing wavelength. Furthermore, an alternative to the

HERMES III experiment was designed that enabled the replication of the effects of a short pulse of ionizing radiation on YAG-based samples.

Lastly, the study of stationary and dynamic color centers in YAG as a function of some specific dopants and contaminants was used to develop compositional guidelines for the fabrication of lasing elements suitable for long-term use in ionizing radiation environments, such as the Earth orbit.

Chapter 2 - Literature Review

Chapter Summary

The literature review is organized into three subsections discussing the development of YAG materials, the development of Nd:YAG lasers, and an analysis of previous research on color centers in YAG-based crystals.

Yttrium aluminum garnet ($\text{Y}_3\text{Al}_5\text{O}_{12}$), or YAG, was first synthesized in experiments studying a solid solution series of naturally-occurring garnet compositions (Yoder and Keith 1951). A closely related yttrium iron garnet (YIG) brought this material wider attention, as it was discovered that YIG possessed net bulk magnetization (Bertaut and Forrat 1956, Gilleo and Geller 1957). This led to more detailed studies of YAG, as well as to the development of more advanced crystal growth techniques that yielded larger, higher quality samples, such as by Lefever (1961) and Linares (1962).

The development of Nd:YAG rested on a body of experimental and theoretical work studying spectroscopy of rare-earth elements (Judd 1962). Rare earth elements – neodymium amongst them – were the subject of decades of research because of the sharply resolved luminescence and absorption lines they produced (Anderson 1907, King 1933, Paul 1936).

Work surrounding color centers in YAG focused mostly on the effects of UV radiation. Early on, it was observed that flash lamps, which are commonly used to pump Nd:YAG lasers and whose spectrum includes the UV, caused a reduction in the system's lasing efficiency (Bass and Paladino 1967). A concurrent body of work studying the effects of other types of radiation – high-energy photons and energetic particles – found

that they produced the same types of effects as UV (Compton and Cesena 1967). A complete discussion of this work and the correlated color-center studies will be provided in the sections below.

Section 2.1

Development of YAG Material

YAG is a crystal in the garnet family, a metal-oxide series of minerals belonging to the $Ia\bar{3}d$ space group (Gilleo and Geller 1958). Garnets are both naturally occurring and synthetically manufactured. The YAG crystal's unit cell is body-centered cubic (BCC). Three of the YAG crystal sites are occupied by cations (the rest are occupied by oxygen ions). Relative concentrations of these sites are expressed in the site composition formula: $C_3A_2D_3O_{12}$. In this formula, c-sites have a dodecahedral shape with point symmetry 222 , while a-sites have an octahedral shape with point symmetry $\bar{3}$. Finally, d-sites have a tetrahedral shape with point symmetry $\bar{4}$ (International Tables for Crystallography).

It should be noted that while the garnet structure falls under the BCC category, this refers to the overall symmetry of the cell. Each node of the reference cube is composed of multiple sites. Therefore the ordinary approach of visualizing a BCC structure by placing anions at the nodes and the cations in the spaces thus formed is not directly applicable to YAG. However, relative arrangements of the individual sites can be visualized, as in the work by Euler and Bruce (1965). Their work is reproduced below in Figure 2.1 and in Table 2.1.

Oxygen sites are generally labeled as h-sites. While the local arrangement of bonds at h-sites varies, they generally have no particular symmetries of importance associated with them.

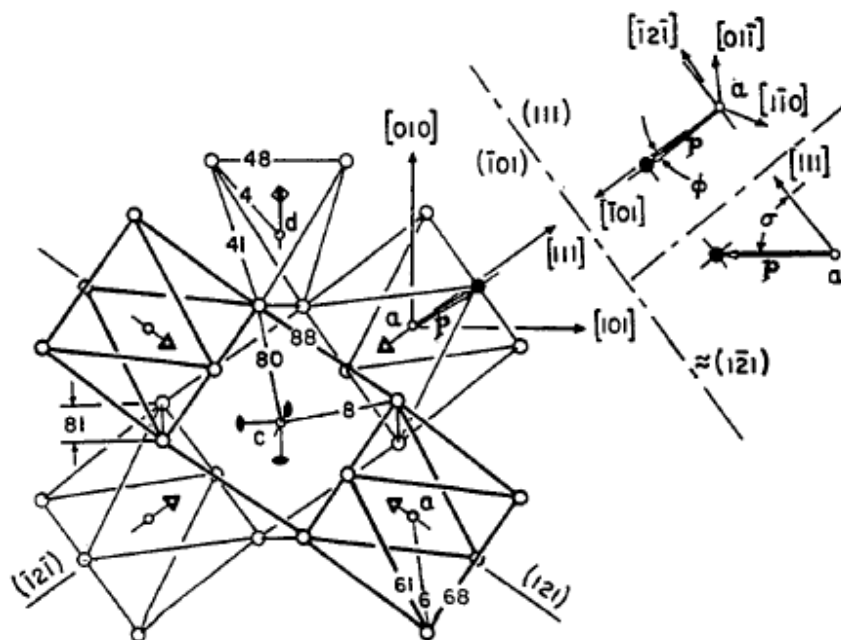


Figure 2.1. Relative arrangement of the cation sites in YAG. Letter indices (a , c , d) refer to the cation site designations. Numerical indices refer to specific anion-anion distances (see Table 2.1). (Reproduced from Euler and Bruce 1965, Figure 1.)

Segment	Length (Å)
4	1.761
6	1.937
8	2.432
80	2.303
41	2.961
48	2.696
61	2.818
68	2.658
81	2.917
88	2.837

Table 2.1. Calculated cation-anion (segments 4, 6, 8) and anion-anion (all other segments) distances in a nominal YAG cell. Segment numbers refer to labels in Figure 2.1 above. (Data reproduced from Euler and Bruce 1965, Table 4.)

Table 2.2 lists several ions that are commonly found in YAG (as either main host lattice constituents, dopants, or contaminants). Naturally occurring garnets are generally orthosilicates. The first yttrium aluminum garnet was obtained by Yoder and Keith in 1951, who were studying solutions series starting with spessartite ($\text{Mn}_3\text{Al}_2(\text{SiO}_4)_2$), continually substituting yttrium for manganese and aluminum for silicon, until complete substitution was achieved. They obtained small fragments (measuring only a few microns in size) of what they considered the other end member of the series – pure YAG. These provided some of the first measurements of x-ray diffraction and index of refraction for YAG (Yoder and Keith 1951).

Ion	Site	Reference
Al^{3+}	a, d	Yoder and Keith 1951
Ca^{2+}	c	Feldman 2003
Ce^{3+}	c	Gui 1996
Cr^{3+}	a	Wood 1963
Cr^{4+} (1)	d	Feldman 2003
Fe^{2+} (2)	c	Smyth 2001
Fe^{3+}	a, d	Gilleo and Geller 1958
Nd^{3+}	c	Kanchanavaleerat 2004
Si^{4+}	d	Smyth 2001
Y^{3+}	c	Yoder and Keith 1951

Table 2.2: List of ions commonly doped into YAG crystals where, again, the site designations c, a and d indicate dodecahedral, octahedral and tetrahedral symmetry respectively. **Note 1:** Chromium ions (specifically Cr^{4+}) only occupy the tetravalent state in the presence of divalent charge compensators, such as Mg^{2+} or Ca^{2+} . **Note 2:** Iron (specifically Fe^{2+}) only occupies the divalent state in the presence of tetravalent charge compensators, such as Si^{4+} .

This new material (which they termed yttrogarnet) received relatively little attention. Synthetic garnets, however, soon became the focus of intense research, when it was discovered that yttrium iron garnet (YIG) was ferrimagnetic (Bertaut and Forrat 1956, Gilleo and Geller 1957).

Gilleo and Geller (1958) were also the first to incorporate Cr^{3+} into a synthetic garnet (they produced Cr:YIG), and to analyze its site preference, finding that it almost exclusively occupied the octahedral a-sites. Chromium's strict site preference meant that there were fewer cases of anti-alignment in the material, increasing its net magnetization. Bertaut and Forrat (1956, 1957) were also the first to incorporate neodymium ions into a synthetic garnet. Similar to Gilleo and Geller, they were not looking for specific optical properties of neodymium, rather they were looking to improve bulk magnetization of the material.

Observing optical properties of high-purity YIG, Lefever and Chase (1960) were the first to make an observation that had important consequences more than a decade later in understanding induced color centers in YAG. They determined that YIG samples contaminated with silicon exhibited a significantly red-shifted absorption edge when compared to YIG samples of greater purity. They attributed the difference to the fact that in pure YIG, iron occupied the trivalent state. While in silicon-contaminated YIG, iron was reduced to the divalent state, which had different absorption properties. Absorption differences between tri- and divalent iron ions were later discovered to be one of the main radiation-induced color centers in YAG (Mori 1977).

Lefever (1961) and Linares (1962) were among the first to produce YAG samples of significant size. They both reported growing samples with cross-section size on the order of 5 mm (a substantial increase compared to the original crystals grown by Yoder and Keith). The interest in the aluminum garnets grew out of studies of optical properties

of rare-earth ions in the garnet structure, such as an early analysis of ytterbium band structure by Wickersheim and White (1960).

At the time, such studies contributed substantially to the on-going research of band structure of rare earth ions. As pointed out by Judd (1962), most of spectroscopic data available at that time was of solutions of rare earth salts, not of solids containing such ions.

In addition to the geometrical structure and site occupation in YAG, information about ionic sizes can also be useful in understand the influence of substitutional dopants. A number of ionic radii for the key species in various coordination sites have been summarized by Shannon and Prewitt (1969). Their data are included below in Table 2.3.

Ion	Ionic Radius (\AA) ¹		
	d-site IV	a-site VI	c-site VIII
Al ³⁺	0.43	0.57	
Y ³⁺			1.09
Ca ²⁺			1.19
Cr ³⁺		0.67	
Cr ⁴⁺	0.51	0.62	
Fe ²⁺	0.70	0.68	
Fe ³⁺	0.56	0.62	
Mg ²⁺			0.96
Si ⁴⁺	0.33	0.45	

Table 2.3. Values of ionic radii for several atomic species for various coordination numbers. **Note 1:** as several estimations were available for the ionic radii, values provided here are averages. Values are omitted for coordination sites not occupied by the given ion. (Data reproduced from Shannon and Prewitt 1969.)

Section 2.2

Development of Nd:YAG and Cr,Nd:YAG Lasers

The widely-cited report by Geusic (1964) of the first operational Nd:YAG laser relied, of course, on a great body of previous work which studied spectroscopic properties of Nd in various material systems.

Perhaps the earliest work on the spectroscopic properties of Nd is by Bahr and Bunsen (1866), in which they studied incandescent fluorescence of neodymium oxide. These early observations were refined over the years. In 1907, Anderson published a report detailing observations of not only luminescent properties of neodymium oxide, but also its absorption properties. He also studied solutions of neodymium salts. These early works, however, bore mostly a qualitative perspective. While these researchers were able to calculate wavelengths of specific bands, no exact tabulation of absorption and luminescence spectra had been accomplished.

Such exact measurements of absorption and luminescence lines of neodymium were carried out by King (1933) and Paul (1936), who worked with vapors of neodymium atoms. Early observations of neodymium in a solid were published by Judd in 1959. What the early research established was that the optical band structure of neodymium was a complex system of narrowly defined energy levels.

At this point, research appeared to accelerate to a tremendous pace. Over the next few years, the understanding of the band structure of neodymium went from a tabulation of individual lines to the development of a thorough theoretical model, and lasers based on its luminescence were developed.

Judd (1962) was the first to publish a mathematical model predicting available energy levels of a trivalent neodymium ion, basing his calculations on previous reports observing neodymium salts in solutions. Koningstein and Geusic (1964) soon improved upon these results by correlating them with data for Nd:YAG crystals, and further refining the model by adding Stark splittings.

One of the first publications demonstrating the lasing operation of neodymium was a report by Snitzer (1961), who described a Nd-doped glass system which operated at room temperature. The first crystal host with neodymium was demonstrated by Johnson et al. (1962) using Nd-doped calcium tungstate (CaWO_4). Geusic et al. (1964) reported on the first Nd:YAG laser in 1964.

Early devices operated using a flash lamp as the pump source, and Allen and Scalise (1969) were the first to report an operating Nd:YAG laser that used a narrow-band diode as its pumping source. Though their work demonstrated the concept, it had to operate at cryogenic temperatures (and, furthermore, used thermal tuning of the diode source), making this early iteration of the mechanism impractical.

Concurrent with developments in understanding of neodymium band structure, luminescence, and lasing properties, there was ongoing research into chromium's optical properties. Similar to works by Judd (1962), Wood et al. (1963) reported on the spectroscopic band structure of trivalent chromium. Substitution of chromium into a garnet structure was investigated by Gilleo and Geller (1958), who studied chromium-doped yttrium-iron garnets. These researchers found that chromium exclusively occupies the octahedral sites in the host lattice. They were studying YIG because of its

ferromagnetic properties due to anti-alignment of iron in tetrahedral and octahedral sites. The research showed that the substitution of chromium in octahedral sites (Cr^{3+}) caused iron to preferentially concentrate in tetrahedral sites (Fe^{3+}), boosting the material's degree of magnetization.

At the same time as the neodymium-based lasers were being developed, two research groups observed that chromium is able to transfer absorbed energy to neodymium – Heitmann et al. (1964) working with powders of aluminum oxide doped with chromium and neodymium, and Murphy et al. (1964), working directly with Cr, Nd:YAG. These groups observed that even if excitation wavelengths are limited to those absorbed exclusively by chromium, neodymium luminescence was nonetheless observed, suggesting that an energy transfer mechanism between chromium and neodymium ions was occurring.

Shortly following these studies, Kiss and Duncan (1964) demonstrated a Cr, Nd:YAG laser operating in continuous and pulsed regimes. They observed that for the case of pumping with a mercury lamp, the pumping threshold was halved compared to that of crystals with the same amount of neodymium but lacking chromium. However, they also noted several major disagreements with Murphy's findings. First, they reported that the luminescence lifetime of chromium was shortened in the presence of neodymium (Murphy reported the luminescence lifetime to be unchanged). Second, the two groups identified different bands of chromium at which energy transfer was said to happen. Murphy et al. identified ${}^4\text{T}_2$, while Kiss and Duncan pointed at ${}^2\text{E}$.

None of these early authors studying effects of co-doping with chromium ions reported any observations on the influence of chromium upon color center formation in these crystals.

Section 2.3

Review of Work on Color Centers in YAG

Soon after Geusic's proof-of-concept work in 1964, further research revealed the susceptibility of Nd:YAG lasers to various forms of ionizing radiation. Most of the early work focused on studying the effects of UV radiation on YAG and Nd:YAG. This was because the most common configuration of a Nd:YAG laser used a gas discharge lamp (such as xenon or krypton) as the pump source, which produced a significant amount of UV light. As such, developing an understanding the behavior of YAG under UV irradiation was an immediate technological imperative. Early work in this area includes publications by Bass and Paladino (1967), Willis and Dixon (1968), Zeidler (1968), and Mori (1973).

Specifically, Bass and Paladino observed that the UV spectral components from a xenon flash lamp created room-temperature-stable color centers. Absorption peaked at 322 nm, but extended over much of the visible and UV spectrum. However, their report was purely empirical, and did not assign these spectroscopic changes to any specific physical processes.

Willis and Dixon (1968) improved upon these findings. They found that the amplitude of the induced absorption – which they found to peak at 330 nm – was connected with a crystal's susceptibility for color center formation. They concluded that the peak was caused by an impurity, though they did not identify a specific culprit. They were also the first to observe transient induced absorption, which differed in form (peaking at 625 nm), and had a lifetime of less than 1 sec.

Finally, Zeidler performed measurements of lasing efficiency for a krypton-arc-pumped system. In this work, a system in which pump light with wavelengths shorter than 500 nm was filtered out was compared to a system which used no filtering. He found that for pulsed operation, lasing efficiency doubled for a system that filtered the pump's light output. The research concluded, then, that the impact of the UV wavelengths in the pump spectrum was to induce color centers that inhibited pumping of the longer-wavelength pump bands. In 1973, this finding was furthered by Mori, who observed that for the case of the unfiltered system, the lasing threshold was also increased.

The findings of this first group of researchers can be summarized in the following form: optical UV irradiation at wavelengths shorter than 500 nm creates at least two types of color centers. One type is stable at room temperature (absorption peaking near 320-330 nm), and the second type is not (absorption peaking near 625 nm). These types have different spectroscopic profiles. Both types of color centers interfere with a Nd:YAG laser's operation by raising the lasing threshold and reducing the lasing efficiency. These color centers are likely caused by uncontrolled impurities. The fact that stable and unstable color centers differ in their spectroscopic features (such as absorption peaks positions and widths) suggests that these color centers are indeed fundamentally different color centers, not simply extremes of a continuum of the same defect type.

The effects of a broader range of ionizing radiation – such as particle and high-energy photons (such as x-ray or gamma radiation) – received significantly less attention in early studies. An important early work in this area is a report by Compton and Cesena (1967). They were motivated less by the immediate technological applications of

Nd:YAG, but rather by the potential of using lasers in space-borne instruments, where they would have to survive a broader range of radiation types. Some of the findings of Compton and Cesena mirrored those of the effects of UV irradiation on the YAG materials. Compton and Cesena found that all types of radiation they studied (accelerated electrons, protons, and gamma rays) increased the lasing threshold and lowered the lasing efficiency of Nd:YAG. They also found that radiation-induced absorption changes partially annealed at room temperature. Furthermore, all types of radiation were seen to cause similar modes of degradation in Nd:YAG.

Their observations went further, however. They measured the excited-state lifetime for Nd, and also induced absorption at pumping and operating wavelengths. For all cases of radiation they studied, the excited lifetime did not change appreciably. Furthermore, radiation-induced absorption at the lasing wavelength was seen to contribute to performance degradation much more significantly than was induced absorption at the pumping wavelengths.

In summary, early work focused on how ionizing radiation affected system performance. Little became known about the physical processes underlying the radiation-induced changes in the materials. All studied types of ionizing radiation – UV, high-energy photon, electron, and protons – caused increases in the lasing threshold, reduction of lasing efficiency, and created color centers (some of which were stable at room temperature, and some were not). Finally, studies showed that uncontrolled impurities hastened the material degradation.

The next major step in the analysis of the effects of ionizing radiation on YAG and Nd:YAG came in the works of Bernhardt (1976) and Mori (1977). The former focused on the effects of x-ray radiation, and the latter continued to work with a xenon flash-lamp. In these studies the authors were able to ascertain greater detail about the photodarkening processes taking place in Nd:YAG.

Specifically, in a series of works, Bernhardt (1974, 1976, 1980) exposed YAG and YAlO_3 (yttrium orthoaluminate) doped with Nd to x-rays at 77 K (the temperature of liquid nitrogen). Gradually warming the samples and observing their thermoluminescence and the evolution of optical absorption, enabled the identification of at least four different types of color centers by their annealing temperature. Corresponding temperature groups were 140 K, 210 K, 240 K, and above room temperature. The latter was attributed to samples contamination with Mn ions.

An important feature in Bernhardt's optical absorption data (1976) must be pointed out, contained in the graph reproduced below in Figure 2.2.

The data show that as the sample warms up, UV absorption (most clearly seen near 200 nm) increases. There are two possible explanations for this increase. The first is that as color centers formed at the cryogenic temperature decay away, a new type of color center is formed. The second explanation is that the Urbach tail absorption comes in toward the longer wavelengths at the higher temperatures – as the material expands with increasing temperatures, inter-atomic distances increase, and the energy gap between the valence and the conduction bands shrinks (Singleton 2006).

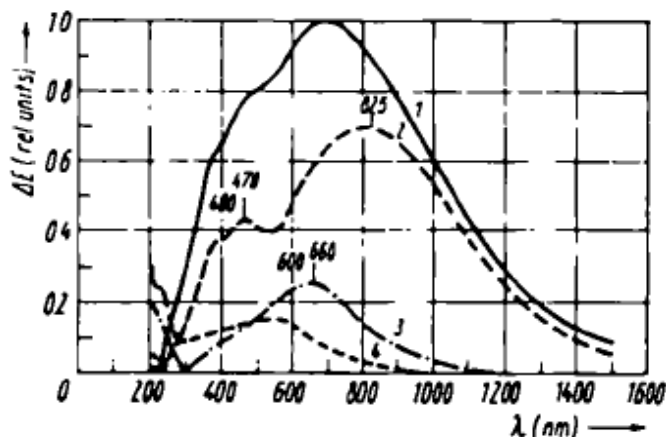


Figure 2.2. Absorption induced in a YAG sample via x-ray irradiation at 77 K. Of importance are curves 1 and 4. Curve 1 is actual absorption at 77 K. Curve 4 is actual absorption at room temperature. (Figure reproduced from Bernhardt 1976, Figure 1.)

In his 1977 work, Mori used absorption spectroscopy coupled with electron-spin resonance (ESR) to analyze bands arising from impurities. By correlating absorption in the 255 nm peak to Fe concentration, he showed that this peak was caused by Fe^{3+} ions. He then co-doped crystals with Si^{4+} (imitating naturally-occurring garnet called almandine, $\text{Fe}_2\text{Al}_3\text{Si}_2\text{O}_{12}$, in which Si ions act as electron donors, reducing Fe ions to a permanent Fe^{2+} state). By correlating Si^{4+} content with increases in absorption at 310 nm, it was shown that this peak – previously observed by Willis and Dixon as well as Bass and Paladino – belong to Fe^{2+} ions. This suggested that recharging of Fe impurity ions was one of the major mechanisms of stable color center formation in YAG.

Mori was also among the first to point out that oxygen vacancies (VO) played a role in capturing electrons on the iron impurities. In particular, it was suggested that as the *F*-type centers (electrons trapped on VO) decay, they can feed electrons to Fe impurities (Mori 1977).

Work by Karaseva et al., which followed in 1985, provided further depth of detail pertaining to color-center structure, and also unified some previous work. In this work, the sources of ionizing radiation used were gamma rays, electrons, and UV radiation from a 337 nm nitrogen laser. The work showed that all three types of radiation produced the same color centers in Nd:YAG. This was the first work that unified the bodies of work based on UV, high-energy photons, and particle radiation.

Karaseva et al. looked at absorption spectroscopy and ESR at temperatures ranging from cryogenic to elevated (from 77 K to 700 K). They were able to identify four specific color centers, along with their associated annealing temperatures:

1. F^+ color center. Its temperature of anneal was 120 K (similar to the lowest reported by Bernhardt), $\lambda_{\text{peak}} = 370, 455, \text{ and } 770 \text{ nm}$. It was identified because its feature resembled F centers in alkali halides – its structure resembled a hydrogen atom (a single electron in a potential).
2. Polarone color center (a self-trapped electron). Its temperature of anneal was 200 K (again, similar to one of the centers identified by Bernhardt), with $\lambda_{\text{peak}} = 650 \text{ nm}$ (similar to Willis and Dixon as well as Mori).
3. O^- center near a divalent cation impurity. Its temperature of anneal was 450 K. It was optically active in 400-650 nm region.
4. O^- center near a cation vacancy. Its temperature of anneal was 700 K, and it was optically active in 280-400 nm region.

This work has summarized color center formation in Nd:YAG in fairly complete detail. However, efforts continued to further understand and explore these processes.

In 1988, Chakrabarti published research in which YAG samples were subjected to neutron radiation and their optical absorption spectra were examined. While the room-temperature-stable spectroscopic changes he observed were very similar to those reported by others, he attributed them to F and F⁺ centers instead of Fe ion impurities, in disagreement with the work of Karaseva and Mori.

This was followed by a fairly derivative work by Čermák et al. in 1989. This group observed in-situ absorption induced in Nd:YAG by a pulsed unfiltered xenon lamp. They reported that the induced coloration (peaking at 525 nm) was reduced if the sample was heated up above room temperature.

The next major step in understand dynamics of color centers in YAG was accomplished by Rose et al. in 1991. They conducted a study of Nd:YAG and Cr,Nd:GSGG samples exposed to gamma radiation from a ⁶⁰C source, by measuring absorption and EPR spectra before and after irradiation. Their first major finding was that the local environment of the Nd ions was not affected by the radiation – since the surrounding potential of Nd ions was not changed by gamma radiation. In their analysis of the Cr,Nd:GSGG samples, they saw the Cr-bearing sample remained essentially unperturbed. This provided some of the earliest evidence suggesting that Cr-doping could increase radiation hardness of YAG.

Rose et al. pursued this idea further in their 1995 work. Here, they studied Cr, Nd:YAG and Nd:YAG under gamma and proton radiation. In agreement with other researchers before them, they found that both types of radiation induced similar changes in Nd:YAG. They also showed that Cr, Nd:YAG (doped with 1 at% Cr) had significantly

reduced susceptibility to radiation (tested with doses up to 500 krad (Si) from a ^{60}Co gamma-ray source).

Akhmadulin et al. published a study in 1992 in which they examined, in closer detail, the mechanism of recharging of Fe ions in YAG. They found that it was possible to change the valence states of Fe ions by illumination with incident photons, though the direction of change depended on the wavelength of the optical exposure. An annealing temperature of 700 K was reported for the Fe color centers.

Karaseva et al. reported the same annealing temperature for the color center they identified as a cation vacancy. This color center, however, increased absorption in the 280-400 nm spectral region, similar to the Fe^{2+} color center, suggesting that Akhmadulin et al., Karaseva et al., and many others may have been referring to the same color center – Fe^{2+} .

Akhmadulin et al. reported that for wavelengths below 310 nm (higher photon energy), Fe ions captured electrons, changing to the Fe^{2+} state. Photons at wavelengths above 310 nm (lower energy) reversed by process, relaxing these color centers. Mierczyk et al., publishing in 1995, contradict this threshold – according to their research, the cutoff wavelength was 450 nm.

Kaczmarek et al., publishing in 1999, studied the effects of several types of radiation (UV light from a xenon flash lamp, gamma, proton, and electron) on Nd:YAG and Ce, Nd:YAG. Again, they observed that all four types of radiation produce similar changes in the materials. They further made two new observations.

The first was that the Ce-bearing sample (containing 0.05 at% Ce) actually performed worse than the sample without Ce, developing a greater concentration of color centers. The second was that UV radiation appeared to have reversed the effects of gamma radiation, photo-bleaching at least some of the gamma-created color centers.

The body of relevant work is rounded out by publications by Matkovskii et al., in 1996 and 2000. They focused their work on YAG doped with Nd, Ce, and Cr^{4+} (via addition of Mg^{2+}). While observing the Fe re-charging process, they also noted an increase in concentration of Cr^{4+} , suggesting that gamma radiation can ionize Cr^{3+} into the four-valent state (co-doping Cr^{3+} :YAG with divalent compensators does not provide complete conversion of Cr). They also confirmed that in small concentrations, Ce co-doping increased radiation-induced losses in the visible.

Section 2.4

Summary of Background Information

YAG is a member of the garnet series, which are complex metal oxides whose atomic arrangement belongs to the $Ia\bar{3}d$ space group. Cation sites available in this space group include sites with dodecahedral (c-sites), octahedral (a), and tetrahedral symmetry (d). The material's general composition formula is $C_3A_2D_3O_{12}$. Naturally occurring garnets usually have silicon occupying the tetrahedral sites. For this reason, garnets are often classified as orthosilicates. However, in general, cation sites can be occupied by a wide variety of alkali metals, transition metals (in particular the iron group), semi-metals, and rare-earth metals.

Nd:YAG lasers are based on the band structure of neodymium, which consists of a series of narrowly defined energy levels. In the most common use of this system, lasing takes place from $^4F_{3/2}$ level to $^4I_{11/2}$ level. The latter is the top splitting of the ground state; $^4I_{9/2}$ is the bottom splitting, the one solely occupied at room temperature. Pumping is possible either by a flash lamp, which takes advantage of many neodymium absorption lines across the visible and NIR regions of the optical spectrum, or directly into one of the bands with a narrow-band source, such as a light-emitting diode.

Color center formation in YAG is mostly due to anion vacancies and contaminants. Oxygen vacancies can trap electrons, forming F and F^+ centers, which are unstable at room temperature. Contaminants – most notably iron and manganese – can form stable color centers by capturing electrons and reducing their oxidation number from +3 to +2. It is thought that oxygen vacancies play a role in formation of permanent

color centers by capturing ionized electrons and then transferring them to deep impurity traps. All types of ionizing radiation – high-energy photons (from UV to gamma), protons, electrons, and neutrons – create similar color centers.

The role of chromium co-doping was explored early in the history of Nd:YAG. In these materials, there exists an energy transfer mechanism, by which energy absorbed by chromium ions can be transferred to the neodymium ions, improving lasing efficiency and lowering the lasing threshold. Later, there was some exploratory research that showed that co-doping with chromium may improve the material's resistance to ionizing radiation. However, the mechanism of improved radiation hardness was not explored in full detail.

Chapter 3 – Experimental Sample Suite

Chapter Summary

The sample suite used in this experiment consisted of a variety of single crystal YAG samples. These were either undoped, or doped with chromium, neodymium, or a combination of these two elements. A number of trace contaminants have also been identified and are hereby described. The presence of iron, the most optically active contaminant, was detected via optical absorption spectroscopy. Iron, along with a number of other impurities (such as alkali elements and silicon), were identified via Glow-Discharge Mass Spectroscopy (GDMS) and Secondary Ionization Mass Spectroscopy (SIMS). In most cases, contaminants were present in concentrations of 10 ppma or less.

Section 3.1

Origin and Physical Description of Samples

Undoped YAG. Undoped samples of yttrium aluminum garnet (YAG) came from Airtron-Litton, Inc. (AL) and from Scientific Materials Corp. (SM). Undoped YAG samples with two purity levels were obtained from SM and will be subsequently identified as YAG (SM avg) and YAG (SM high). Samples were cylindrical, with diameters of approximately 12 mm and thickness of approximately 2 mm. The Airtron-Litton sample was polished at the Center for Research and Education in Optics and Lasers (CREOL), University of Central Florida (UCF). Samples from Scientific Materials were polished at the point of origin. No coatings were applied to these samples.

Nd:YAG. Neodymium-doped samples came from United Crystals (0.5 at% Nd and 1.2 at% Nd) and from Scientific Materials Corp. (1.0 at% Nd). The former supplied samples in square rods (7 mm by 7 mm on a face). The latter supplied samples in round rods (7 mm diameter face). Samples used for ionizing-radiation experiments conducted at the HERMES III accelerator (see Chapter IV) had lengths of approximately 12 mm. Samples used in UV irradiation experiments (see Chapter V) and in optical absorption measurements were cut from the as-delivered rods, with slice thickness varying from 0.8 mm to 2.7 mm. As-delivered rods were polished at their respective points of origin. No coatings were applied to these samples. Slices were polished at CREOL as discussed above.

Cr³⁺:YAG. Chromium-doped samples came from United Crystals (0.5 at% Cr and 2.0 at% Cr) and from Scientific Materials Corp. (1.5 at% Cr). Samples provided by

United Crystals were supplied in the form of square rods (7 mm x 7 mm x 12 mm). Scientific Materials provided cylindrical slices of 2 mm thickness and 12 mm diameter. Original samples were polished at the point of origin. No coatings were applied to these samples. Rods from United Crystals were sliced into thinner samples (with thicknesses varying from 0.8 mm to 2.7 mm), and then polished at CREOL.

$Cr^{3+}, Nd:YAG$. Co-doped samples came from Airtron-Litton Inc. (0.13 at% Cr, 1.0 at% Nd) and from Scientific Materials Corp. (0.5 at% Cr, 1.0 at% Nd; and 1.0 at% Cr, 1.2 at% Nd). Samples from Airtron-Litton were supplied as cylindrical rods (7 mm in diameter and 10 mm in length), and originally had an anti-reflection coat (at 1064 nm), which was removed by polishing at CREOL. Samples from Scientific Materials with the lower Cr and Nd dopant levels came as round rods (5 mm in diameter and 10 mm in length), uncoated and polished at the point of origin. Samples from Scientific Materials with the higher Cr and Nd dopant levels came as a raw crystal boule (with an irregular, tapered rod diameter of approximately 25 mm for most of the rod x 150 mm in length). This sample was sectioned into thinner rods (thicknesses from 1 mm to 9 mm) and polished at CREOL. These were further cut into smaller squares (7 mm x 7 mm).

It is important to note that when the crystal boule was ordered from Scientific Materials, the chromium concentration was specified as “0.5 at% in the melt,” while the neodymium concentration was specified as “1.2 at% in the crystal.” Since the incorporation rate for chromium is greater than one, its actual concentration in the crystal is expected to be higher than it is in the melt (approximately by a factor of 2). Therefore,

its dopant concentration is stated as 1.0 at% Cr, 1.2 at% Nd. This concentration was confirmed via SIMS measurements, as will be discussed below.

Section 3.2

Optical Absorption Spectroscopy

Optical absorption spectroscopy was used to verify sample composition. These spectra were collected from all samples upon receipt, and used as a reference for subsequent measurements.

Section 3.2.1

Method

Section 3.2.1.1

Physical Setup and data Collection

Absorption measurements were carried out using a Perkin-Elmer Lambda 950 spectrophotometer. A general layout and operation of this instrument is show below in Figure 3.1.

The instrument uses two selectable light sources a deuterium (D₂) and a tungsten lamp. The deuterium lamp is primarily used as the source of UV light (default operating range is from 190 nm to 320 nm). The tungsten lamp provides the rest of the spectrum.

A number of selectable optical filters are used to choose portions of the spectrum before the light goes to the monochromator. The choice of filters is not customizable.

The monochromator selects the current wavelength being used to interrogate a sample by rotating a grating. The monochromator can select from two gratings. One is used primarily for the UV and visible portion of the spectrum (default operating range from 190 nm to 860 nm). The second grating is used for the IR portion of the spectrum.

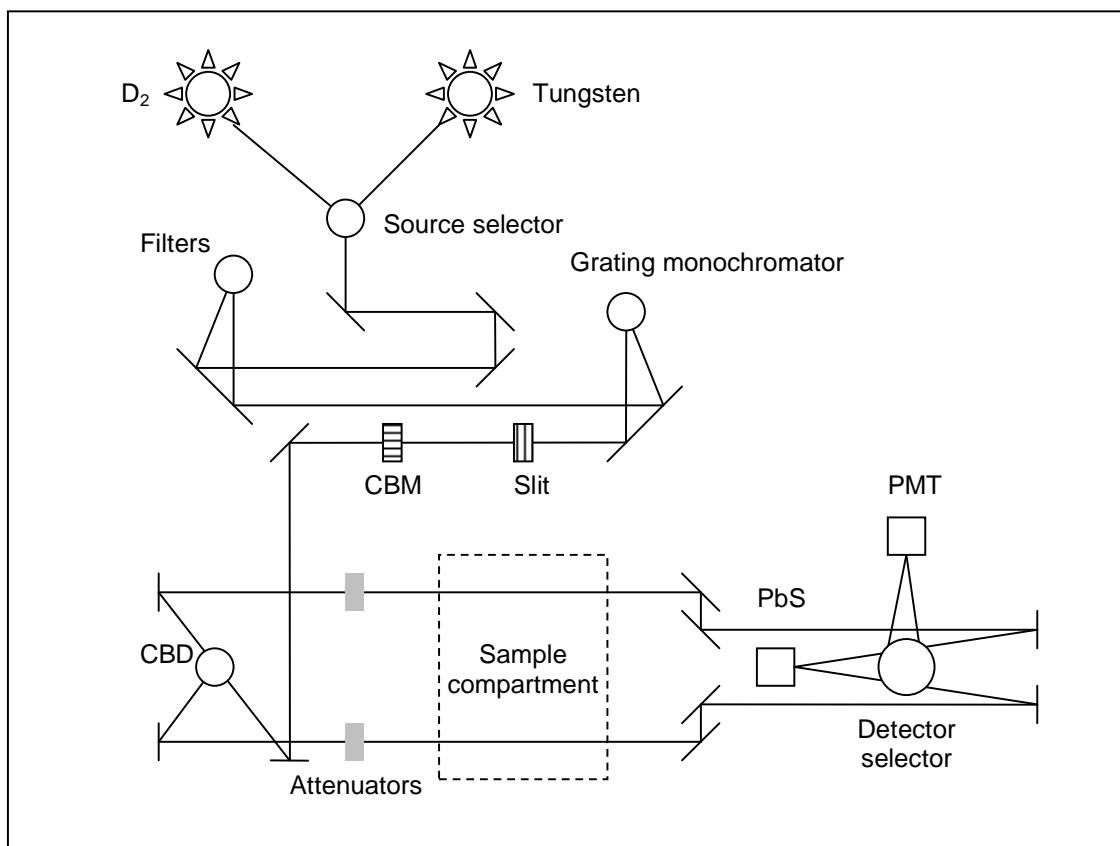


Figure 3.1. Schematic layout of the optical spectrometer (Perkin Elmer Lambda 950) used in these experiments. Diagram based on the technical documents shipped with the instrument.

The light from the source then passes through a programmable slit, which sets spectral resolution (offset by intensity available for sample interrogation), as well as the horizontal dimension of the probe spot in the sample space. The Common Beam Mask (CBM) sets the vertical dimension of the probe spot.

The Common Beam Depolarizer (CBD) assembly optionally depolarizes the light, as well as splits the light between the two channels – one for the sample, and one for active referencing. The depolarization was activated for all measurements.

Before entering the sample compartment, the two beams pass through optional variable attenuators. These attenuators were not used in any measurements as they were set for 100% nominal transmission for both channels.

After passing through the sample compartment, the two beams enter the detector assembly. Either of the two detectors is used. The Photo-Multiplier Tube (PMT) is used primarily for the UV and visible portion of the spectrum (default operating range is from 190 nm to 860 nm). The lead sulfide (PbS) detector is used for the IR portion of the spectrum. The wavelength position of the detector switch is also selectable.

Measurements were taken at room temperature and in the ambient atmosphere.

Data were collected over a broad spectral window, generally from 200 nm to 2000 nm. However, features of interest were usually identified in the narrower window 230 nm to 850 nm. Generally, data were sampled every 0.5 nm, with an integration time of 0.5 sec and a nominal resolution of 1 nm.

The instrument reported the value of a sample's absorbance at a specific wavelength:

$$A(\lambda) = -\log\left(\frac{I_{trans}(\lambda)}{I_{inc}(\lambda)}\right) = -\log(T(\lambda)) \quad (3.1)$$

This value included all sources of loss within the sample – internal material absorption, scattering, and Fresnel reflections. Scattering was assumed to be negligible. Losses due to Fresnel reflections were not corrected for, since only absorption peak positions and relative intensities were considered of importance. Since the coefficient of absorption is the value of importance in the rest of this report, its values are presented in

this chapter, calculated per the equation derived below in Equation 3.2 in which z represents the physical length of the sample, α is the absorption coefficient in units of $(\text{unit length})^{-1}$, and A is the measured absorbance (also called optical density, or OD) of the sample.

$$T(\lambda) = \exp(-\alpha(\lambda)z)$$

$$A(\lambda) = -\log(T(\lambda))$$

$$A(\lambda) = -\log(\exp(-\alpha(\lambda)z)) = \alpha(\lambda)z \log(e)$$

$$\alpha(\lambda) = \frac{A(\lambda)}{z \log(e)} \quad (3.2)$$

While the rest of the report deals with differential absorption data – in which case the Fresnel contribution is implicitly subtracted out – data presented in this chapter are from a single measurement, and therefore include the Fresnel contribution. Furthermore, no effort was made to remove this contribution from the data here presented, since only position and relative peak amplitudes are of interest, not their absolute values. However, since the value of the absorption coefficient in the following graphs includes this contribution, it is labeled as α^* .

Section 3.2.1.2

Sources and Mitigation of Error – Sample Positioning

It was found that measurements could be affected by sample positioning, since small inhomogeneities in surface quality and sample tilt or wedge affected the magnitude of the surface Fresnel reflections, thereby impacting the measured loss in optical transmittance of the samples by the spectrometer. To counter this inconsistency, special sample holders were designed to fit into the spectrometer in a repeatable fashion such that very little alignment of the samples was required (physical parts of the instrument were utilized as hard references). The same sample holders could also be used in the UV irradiation experiments. Thus samples did not need to be removed from the sample holders while a cycle of irradiations and measurements was taking place.

Section 3.2.1.3

Sources and Mitigation of Error – Instrumental “Steps” and “Stitching”

It was observed that this spectrophotometer, like many others, sometimes displayed “steps” in its data output. “Steps” are sudden changes in signal level associated with internal instrument changes. As such, they are measurement artifacts and do not represent real data. For example, the instrument uses different lamps for different parts of the spectrum. It switches between the lamps using a mirror. However, since the mirror does not re-position perfectly every time, the overall system alignment can change slightly from the calibration run to the data collection run. One of the channels effectively, then, has more or less light than it did during the calibration run. This results in a step in the data. Essentially, portions of the data include small random offsets – positive or negative – added to the real data.

A procedure that removes these steps is here referred to as “stitching.” Stitching involves identifying, with great certainty, the real value of the measured absorbance at some point. This point can then be used as reference to remove offsets from the rest of the data.

Through multiple observations of instrument behavior, it was found the UV part of the spectrum changed the least over multiple measurements. Therefore, it was deemed the most stable, and was used as the reference region in stitching the data.

Stitching was carried out in sequence, first equalizing the visible spectral data to the UV, and then NIR to visible. At each point where a step occurred, the following automatic procedure was used.

Stitching was carried out using an automated Python script (with Numpy and Scipy optimization routines). A small sub-sample of the spectrum was taken, which included several points prior to and after the wavelength at which the changeover took place (the source change, the detector change, or the grating change). A third order polynomial was fit to the interval. The fit's error was used as the value to be minimized by the optimization function. A variable that was added to or subtracted from the region being adjusted was used the optimized parameter.

The script read ASCII files provided by the spectrometer's software, extracting raw data values, as well as wavelength positions of relevant changeovers.

The unstitched steps in raw data have been observed to be as large as 0.07 optical density units. For a sample with thickness of 0.2 cm (a common thickness used in this report), this would translate to a false coefficient of absorption value of 0.8 cm^{-1} . Considering most real changes observed in differential absorption measurements were on the order of 1 cm^{-1} or less, unstitched steps would, therefore, represent a major source of error.

Section 3.2.2

Results and Discussion

Optical absorption measurements were carried out on all applicable samples in the experimental sample suite following the methodologies outlined above. This section presents a summary of the preliminary data taken on the samples, before they were subjected to any further experimental procedures. Some limited analysis, identifying major compositional components (both dopants and contaminants) is also here presented.

It should be noted that the optical transitions described in the following sections are mostly between the same orbitals for a given ion. For example, for the case of transition metals (spectra of Fe^{3+} and Cr^{3+} will be discussed), optical transitions are predominantly between d orbitals.

Such transitions are forbidden under potentials that have inversion symmetry. Of the two sites ordinarily occupied by these ions, the octahedral site (occupied exclusively by Cr^{3+} and some Fe^{3+}) has inversion symmetry, which in principle should largely preclude these ions' optical activity.

However, let us compare the various ionic sizes for the particular coordination number VI (refer to Table 2.3). Both Cr^{3+} and Fe^{3+} are significantly larger than the Al^{3+} ion they are replacing. Because of the size discrepancy, some site distortion is to be expected. This distortion relaxes the inversion symmetry of the site, permitting optical activity to some extent.

Particulars of the site distortions due to Cr^{3+} and Fe^{3+} have been described by Wood et al. 1963 and Dong et al. 2005, respectively.

Section 3.2.2.1

Undoped YAG

The optical absorption coefficient data from three samples (one of each manufacturer and purity level) are depicted below in Figure 3.2.

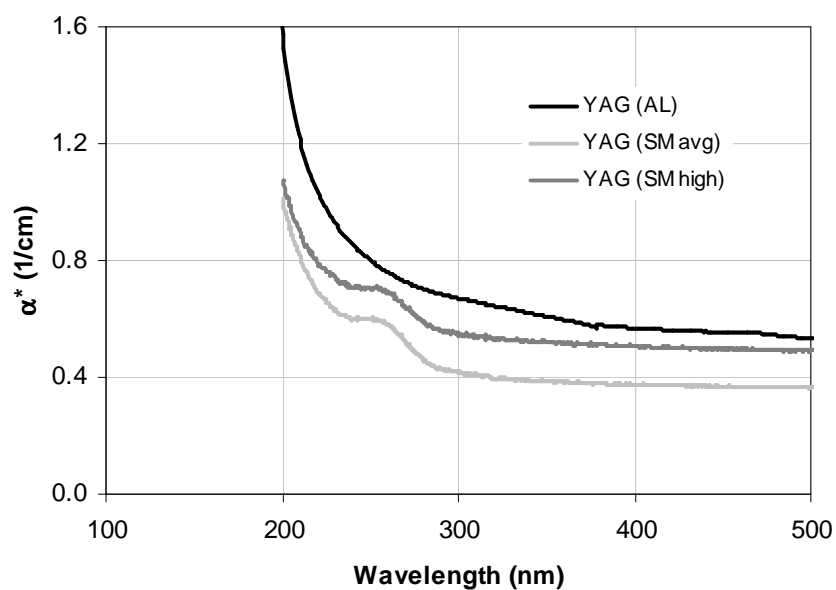


Figure 3.2. Thickness-normalized absorbance of undoped YAG samples. “AL” stands for Airtron-Litton. “SM” stands for Scientific Materials. Labels “avg” and “high” refer to relative purity of the sample.

As can be seen from the data, all of the samples were nominally transparent in the visible, with fundamental absorption edges near 190 nm. Absorption across the represented spectral range is due to uncorrected Fresnel losses. Spectra remain essentially flat and featureless out to 2000 nm (this portion not shown in the Figure 3.2.)

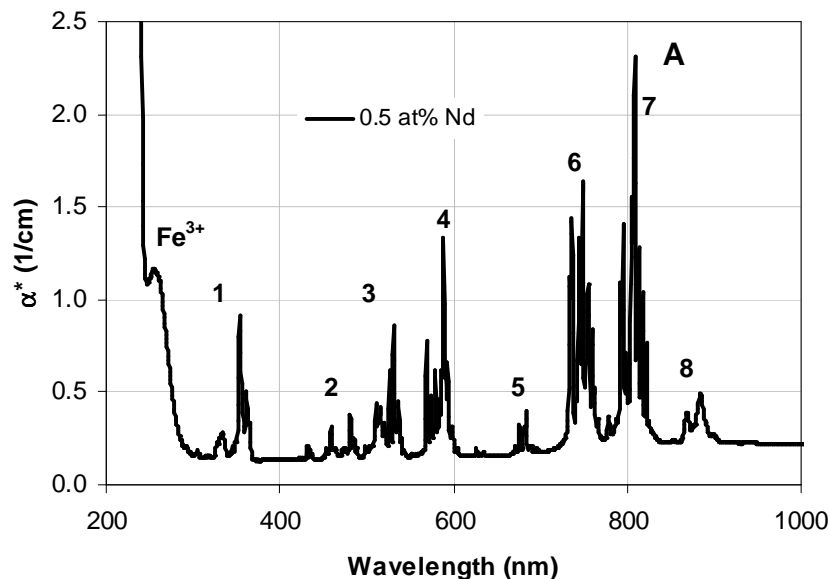
The peak near 250 nm, most clearly seen in the Scientific Materials samples, is attributed to the trivalent iron impurity (Mori 1977).

Section 3.2.2.2

Nd:YAG

Representative optical absorption spectra of various Nd:YAG samples are shown in Figure 3.3 below.

The representative spectra in Figure 3.3 above show a combination of known features due to neodymium (sharp lines) and contamination (broad peak near 250 nm, similar to undoped YAG). A description of neodymium's level structure is discussed in greater detail in literature (Judd 1962, Konigsten and Geusic 1964, Weber and Varitomos 1971). Table 3.1 below lists some of the transitions that could be identified in the optical absorption spectra of the Nd:YAG samples.



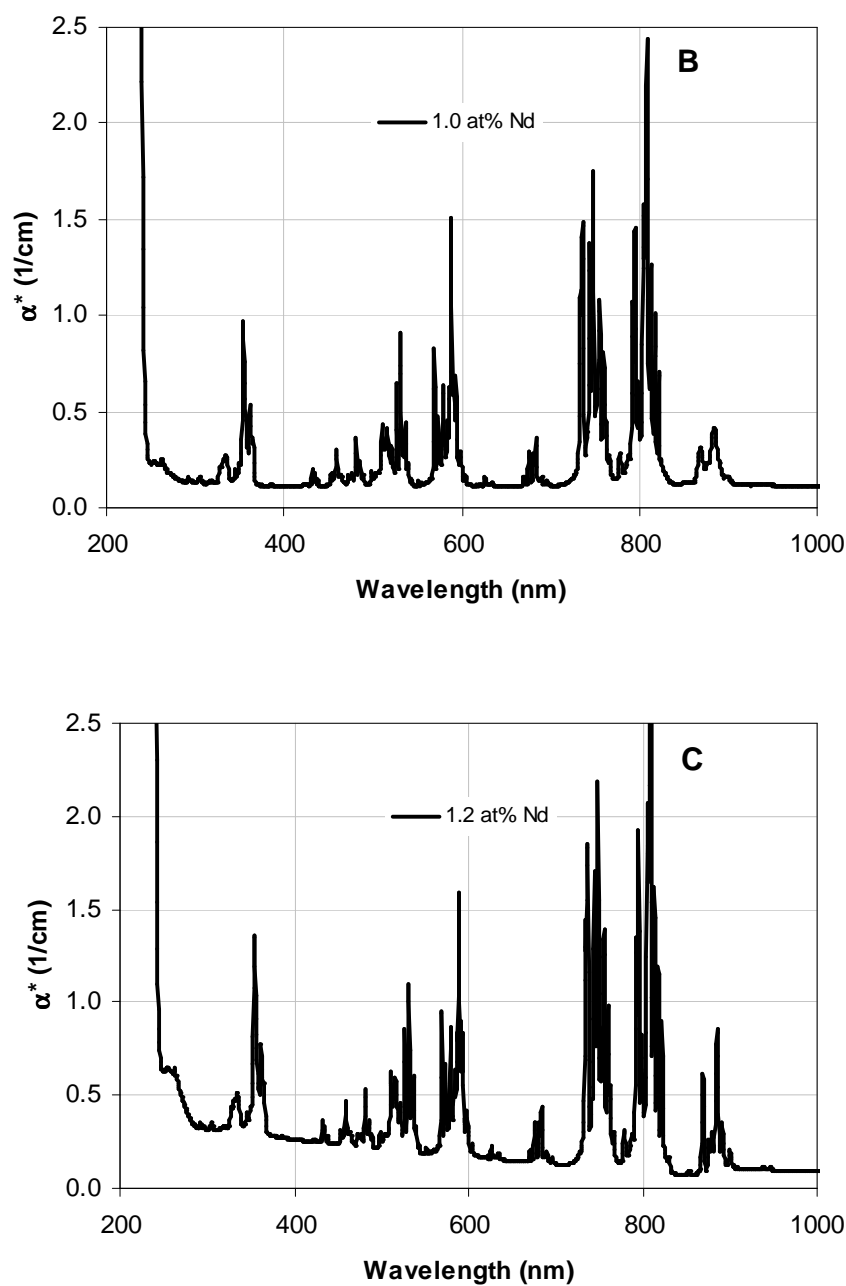


Figure 3.3. Representative optical absorption spectra of various Nd:YAG compositions. A: 0.5 at% Nd:YAG from United Crystals. B: 1.0 at% Nd:YAG from Scientific Materials. C: 1.2 at% Nd:YAG from United Crystals. Number labels in A refer to groups of transitions associated with Nd level structure. These associations are listed in Table 3.1.

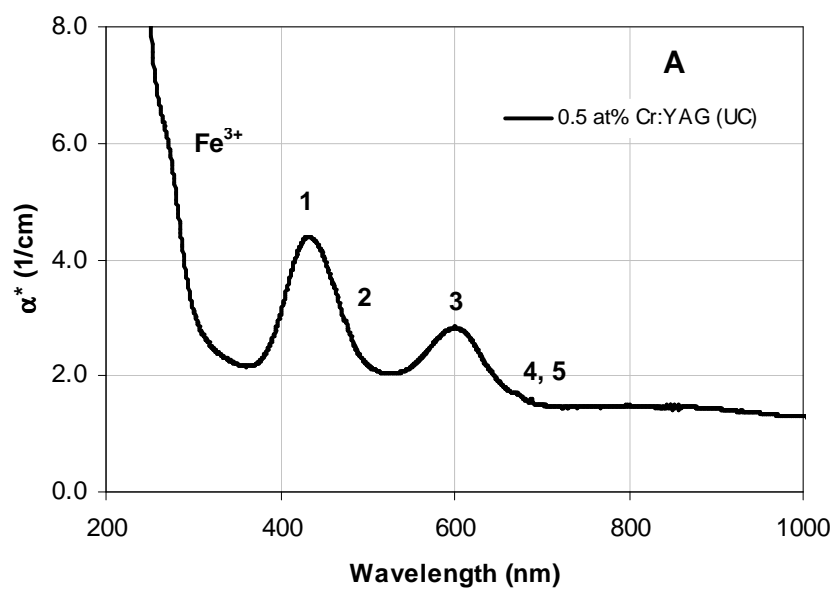
It is interesting to examine the relative magnitude of the short-wavelength iron peak, located at ~250 nm in Figures 3.3. A comparison of the figures shows that the amplitude of the peak varies significantly from sample to sample such that this peak appears to be much smaller in the Scientific Materials' sample than in the United Crystals' samples. This indication of the lower concentration of iron is confirmed by mass spectroscopy analysis (see Section 3.3 of this Chapter) and suggests that the Scientific Materials samples were higher purity.

Label #	Nd transitions
1	$^4D_{3/2}, ^4D_{5/2}, ^2D_{1/2}, ^4D_{1/2}, ^2L_{15/2}$
2	$^4G_{9/2}, ^3D_{3/2}, ^2K_{15/2}$
3	$^4G_{7/2}, ^2G_{9/2}, ^2K_{13/2}$
4	$^4G_{5/2}, ^2G_{7/2}$
5	$^4F_{9/2}$
6	$^4F_{7/2}, ^4S_{3/2}$
7	$^2H_{9/2}, ^4F_{5/2}$
8	$^4F_{3/2}$

Table 3.1. Some of the Nd optical transitions that can be identified in the samples' optical absorption spectra. Label # column refers to the labels in Figure 3.3A. Transitions are between the indicated states and the ground state ($^4I_{9/2}$).

Section 3.2.2.3 **Cr^{3+} :YAG**

Figure 3.4 below contains representative spectra of the various compositions of Cr^{3+} :YAG tested in this report.



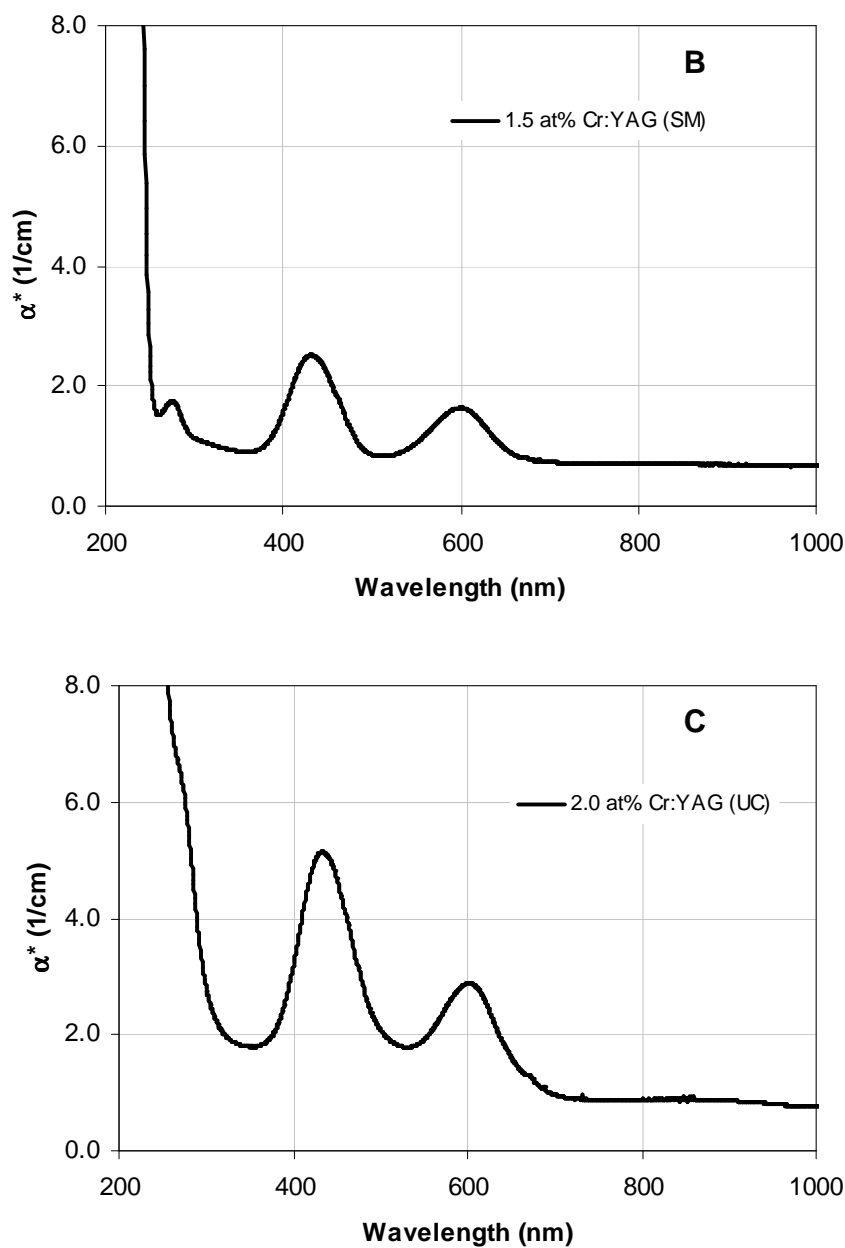


Figure 3.4. Representative optical absorption spectra of various Cr³⁺:YAG compositions. A: 0.5 at% Cr³⁺:YAG from United Crystals. B: 1.5 at% Cr³⁺:YAG from Scientific Materials. C: 2.0 at% Cr³⁺:YAG from United Crystals. Number labels in A refer to specific transitions of the Cr_{oct}³⁺ ions. These transitions are listed below in Table 3.2. In addition, the Fe³⁺ absorption band at ~250 nm is indicated in A.

An examination of the data reveals the presence of broad peaks located near 425 nm and 590 nm. These peaks may be associated with the trivalent chromium ion. For an in-depth discussion of the band structure of octahedral trivalent chromium in YAG, see Wood et al. 1963.

Label #	Cr transition
1	4T_1
2	2T_2
3	4T_1
4	2T_1
5	2E

Table 3.2. Optical transitions that can be identified in the optical absorption spectra of the Cr:YAG samples. Numbers refer to the labels in Figure 3.4A. These transitions initiate in the ground state (4A_2). (Wood 1963, Feldman 2003)

While the band structure described above is ordinarily ascribed solely to Cr_{octo}^{3+} , a closer examination of the NIR portion of the absorption spectrum reveals features not associated with this ion. This portion of the spectrum is shown below in Figure 3.5

It is apparent that the Cr^{3+} :YAG sample shown in Figure 3.5 – nominally undoped with any charge-compensating species such as Ca or Mg – displays some bands in the NIR. These bands are ordinarily assigned to Cr_{tet}^{4+} . An example of these bands can be found in Feldman et al. 2003, as shown in Figure 3.6 below.

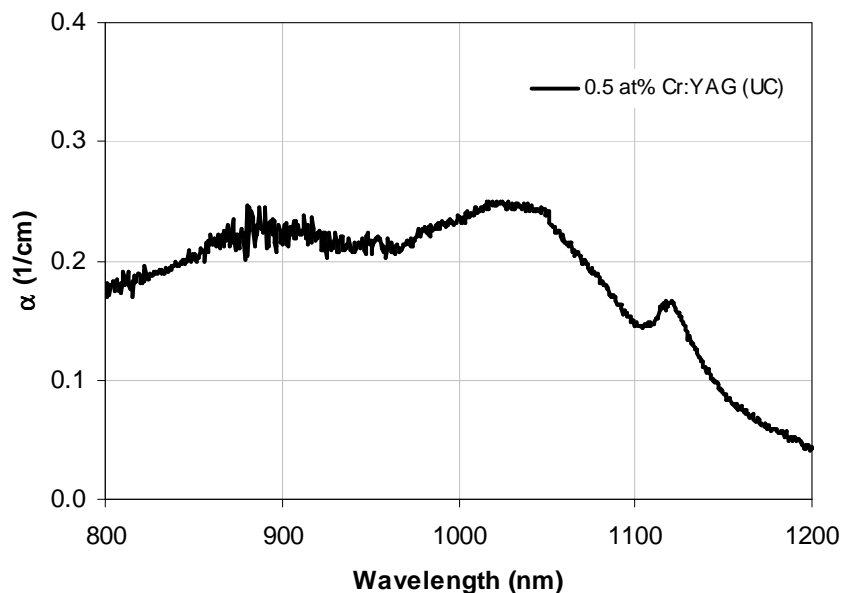


Figure 3.5. Absorption observed in a nominally Cr^{3+} :YAG sample in the NIR.

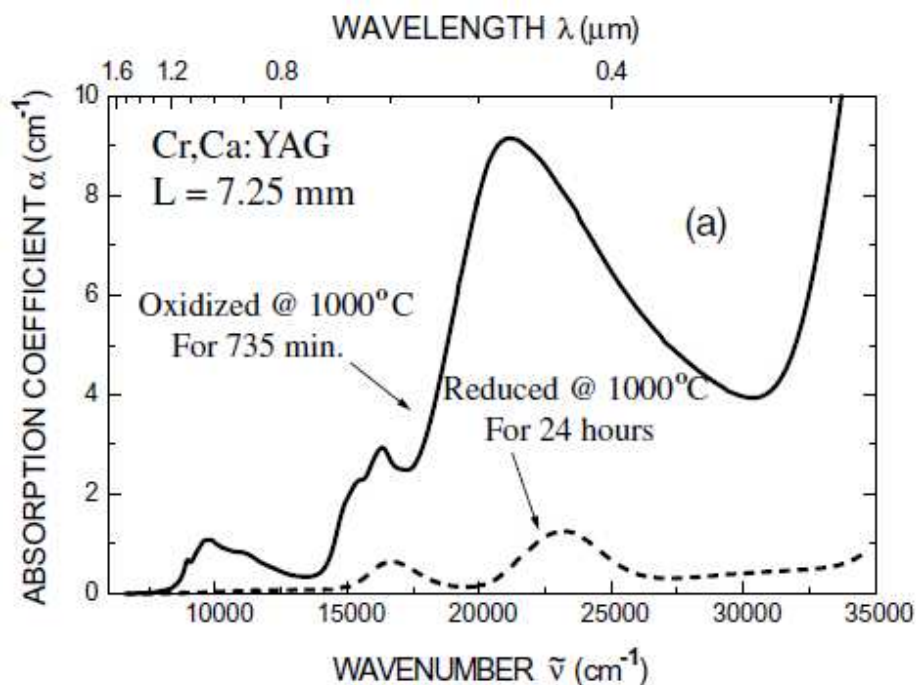


Figure 3.6. An example of $\text{Cr}_{\text{tet}}^{4+}$ optical absorption bands. A comparison of the group of bands near 10,000 $1/\text{cm}$ to the bands shown in Figure 3.5 supports the assignment of these bands to $\text{Cr}_{\text{tet}}^{4+}$ (Figure reproduced from Feldman et al. 2003).

These bands near 1 μm are explicitly assigned to Cr_{tet}^{4+} by Feldman et al. 2003 (refer to Table 1, bands 1-3, in their publication). The presence of these bands should be considered along with the fact that while the Cr^{3+} :YAG samples depicted in Fig. 3.5 are not nominally doped with divalent dopants (Ca, Mg), these elements have been found in trace amounts in every sample examined using mass spectroscopy as will be discussed below (refer to Tables 3.3 and 3.5 of this report).

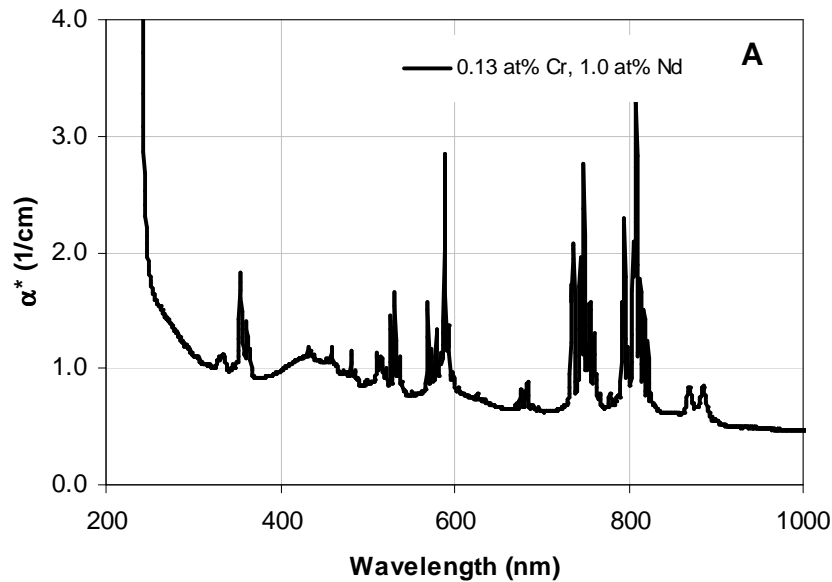
The optical absorption data presented above in Figure 3.5 therefore suggest that small quantities of chromium in the material interact with the divalent impurities such as Ca and Mg as a charge compensator. In this case, the Cr^{3+} donates an electron to the dodecahedral Ca and Mg sites (which would be undercompensated and would act as sources for oxygen vacancy defects without the electron donation), while itself occupying the tetrahedral site as Cr_{tet}^{4+} .

Section 3.2.2.4

Cr,Nd:YAG

Representative optical absorption spectra for Cr,Nd:YAG co-doped samples are shown below in Figure 3.7.

The spectra are simply composed of the features found in the previously shown, singly-doped materials. Spectrally narrow features generally belong to the neodymium ions (compare to spectra in Figure 3.3 above). The broad features near 425 nm and 590 nm are attributed to the trivalent chromium dopant (compare to spectra in Figure 3.4 above). The broad peak near 255 nm (most visible in the two Scientific Materials samples) is again attributed to the trivalent iron impurity.



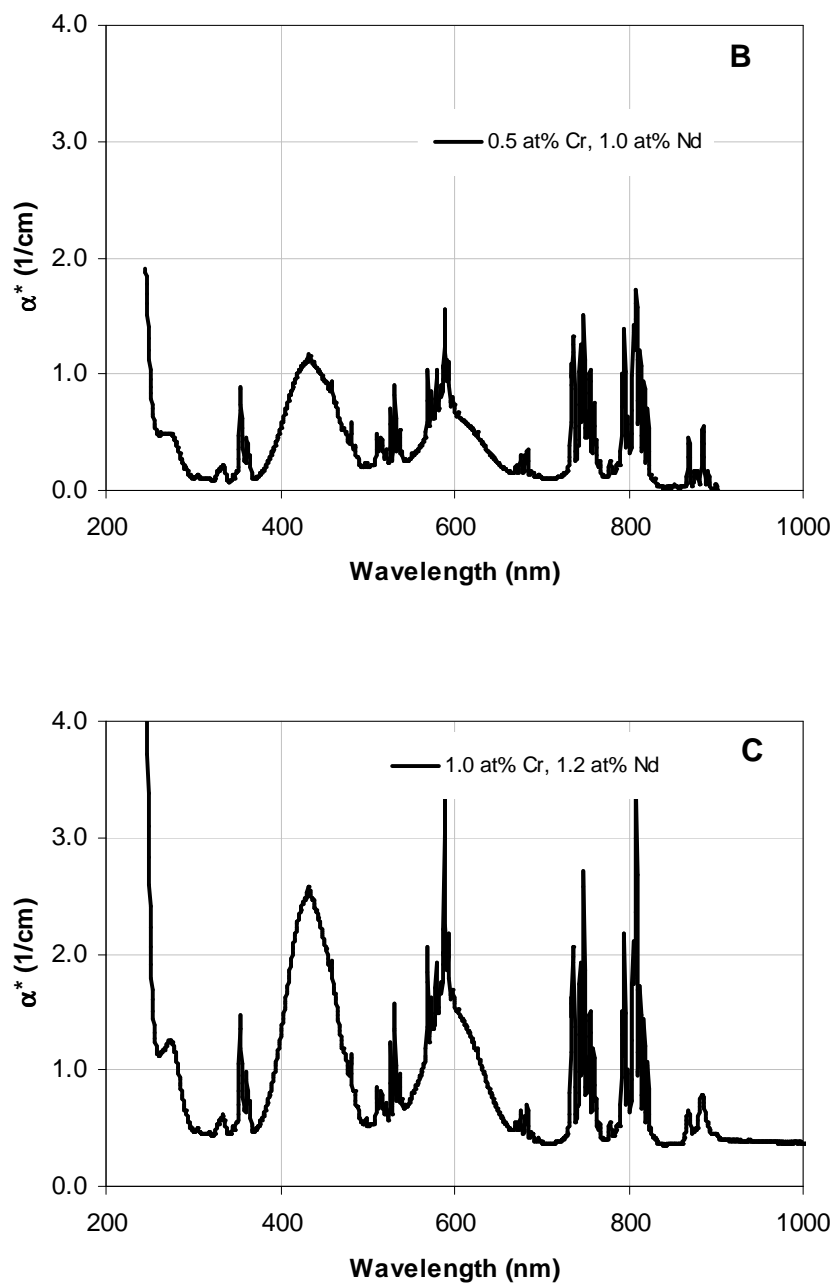


Figure 3.7. Representative optical absorption spectra of various Cr, Nd:YAG compositions. A: 0.13 at% Cr, 1.0 at% Nd:YAG from Airtron-Litton. B: 0.5 at% Cr, 1.0 at% Nd:YAG from Scientific Materials. C: 1.0 at% Cr, 1.2 at% Nd:YAG from Scientific Materials.

Section 3.3

Mass Spectroscopy

It was known from previous studies of color center formation in YAG that small (on the order of 1-10 ppma) quantities of iron contamination can drastically affect the material's behavior in the presence of ionizing radiation. For this reason, two tests were carried out to ascertain quantities of low-concentration impurities in our samples – Glow Discharge Mass Spectroscopy (GDMS) and Secondary Ionization Mass Spectroscopy (SIMS). The former was performed at Northern Analytical Laboratory, Inc. The latter was performed at Advanced Materials Processing and Analysis Center (AMPAC) at University of Central Florida (UCF).

Section 3.3.1

Method

Section 3.3.1.1

Glow Discharge Mass Spectroscopy

In this technique, the sample is bombarded with a beam of accelerated ions, such as argon, while surrounded by a low-pressure plasma. Only neutral atoms can be ejected into the plasma, where they subsequently become ionized, and can then be analyzed for quantity. This technique provides absolute concentration values for the compositional constituents of the sample. The sample is completely consumed in this test. A general schematic illustrating operation of a GDMS measurement is show below in Figure 3.8 and a more complete description of the measurement follows.

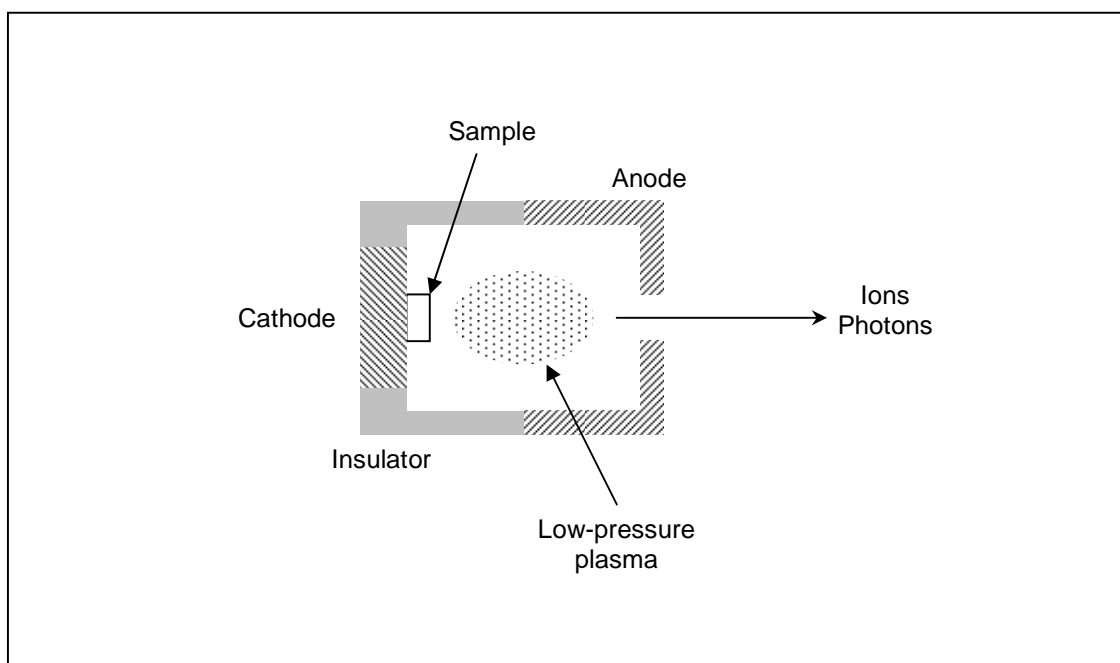


Figure 3.8. A general schematic representing operation of Glow Discharge Mass Spectrometer.

A GDMS instrument consists of a chamber in which one end is a cathode while the other end is anode. The sample is housed on the cathode. The anode end of the chamber also has a portal, through which examination can take place. The chamber is filled with a low-pressure gas.

As bias is increased and current begins to flow from the cathode to the anode, the gas is gradually ionized. Electrons are accelerated towards the anode, while the positively charged ions are accelerated toward the sample. As they impact the sample, they eject its elemental constituents into the low-pressure plasma. There, the sample's atoms become ionized. In this way, the plasma re-generates itself, even as it leaks out through the portal.

Sample ejecta, along with the photons generated by the plasma cloud, exit through the portal on the anode side of the chamber. These can be analyzed using an optical or a mass spectrometer, thus providing information about the elemental composition of the sample. This description of GDMS is based on the discussion by Barshick (2000).

Data presented by the analytical lab consisted of a table of atomic species, with their corresponding concentration in parts-per-million-weight (ppmw). These numbers were converted to parts-per-million-atomic (ppma) using Equation 3.3, shown below:

$$ppma(X) = ppmw(X) \cdot \frac{MolWt(YAG)}{20 \cdot AtWt(X)} \quad (3.3)$$

In this equation, $MolWt(YAG)$ is molecular weight of YAG (593.63 au), and $AtWt(X)$ is atomic weight in au of the species in question. The number twenty in the denominator represents the number of atoms in a chemical formula unit of YAG.

Table 3.3

Element ¹	Atomic Weight	Concentration	
		ppmw	ppma
B	11	0.11	0.3
Ca²	40	2.0	1.5
Ce	140	0.60	0.1
Cl	35	10	8.4
Cr ³	52	3000.0	1712.5
Cu	64	0.20	0.1
Dy	163	0.40	0.1
Er	167	0.30	0.1
Eu	152	0.1	0.0
Fe²	56	3.0	1.6
Ga	70	1.2	0.5
Gd	157	0.55	0.1
Ho	165	0.10	0.0
K²	39	1.0	0.8
La	139	0.25	0.1
Lu	175	0.12	0.0
Mg²	24	0.30	0.4
Mn	55	0.10	0.1
Na²	23	2.3	3.0
Nd ³	144	8000.0	1646.2
Ni	59	0.07	0.0
P	31	0.30	0.3
Pr	141	0.15	0.0
S	32	10.0	9.3
Si²	28	12	12.7
Sm	150	0.30	0.1
Ti	48	0.13	0.1
Tm	169	0.05	0.0
V	51	0.02	0.0
Yb	173	0.50	0.1
Zn	65	2.0	0.9
Zr	91	0.40	0.1

Table 3.3. Tabulated results of GDMS analysis of a sample taken from a crystal boule grown by Scientific Materials Corp. **Note 1:** aluminum, oxygen, and yttrium were listed as major constituents, and therefore not tracked in this analysis. **Note 2:** the elements

marked in bold were considered especially relevant, and special attention was paid to tracking their concentrations in the SIMS data (see Section 3.1.3 below) **Note 3:** GDMS is intended for trace analysis, therefore its reporting of elements present in high concentrations is unreliable.

Since the technique is destructive (the entire sample is consumed) and relatively expensive, only one sample (a slice of the Cr,Nd:YAG crystal boule obtained from Scientific Materials Corp.) was submitted for this analysis. The complete report, including the original numbers in ppmw as well as re-calculated ppma values, is reproduced below in Table 3.3.

Section 3.3.1.2

Secondary Ionization Mass Spectroscopy

For this experiment, the sample surface is impacted with high-energy oxygen ions. Ejected surface ions are then ionized and analyzed via a mass spectrometer. A schematic representation of a SIMS instrument is shown below in Figure 3.9. The following description is based on the discussion by Cristy (2000).

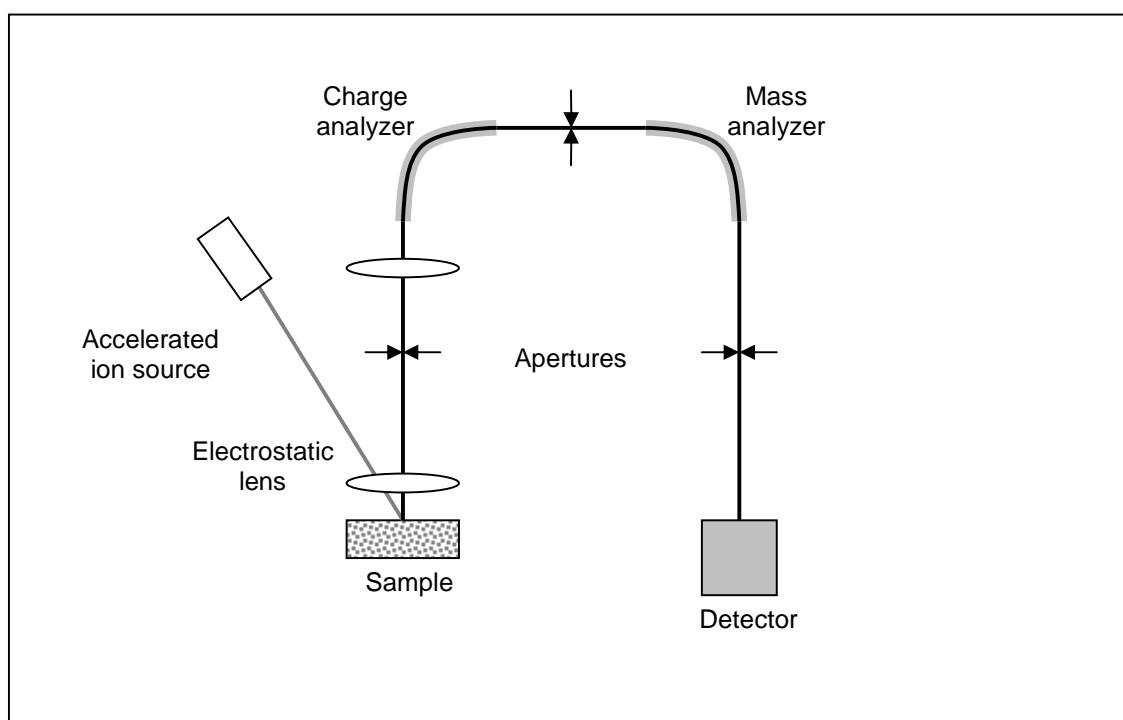


Figure 3.9. Schematic representation of a Secondary Ionization Mass Spectrometer.

The beam of ions ejected from the sample is focused using electrostatic lenses. Physical apertures are used for rejecting ions ejected along undesirable paths. The ejected ions are first screened for a uniform charge using the charge analyzer and its adjacent aperture. The ions are then separated according to their mass using the mass analyzer.

The last aperture ensures that only ions of a specific mass reach the detector (usually, a charge detector such as electron multiplier, or a fluorescent screen).

Reported data consists of physical detection counts for a range of ionic masses. Since ejection ratios and capture rates can differ for various atomic species and are not always known, this test does not provide absolute concentration values, but only relative ones.

Although this technique is also destructive, only a small portion of a sample is destroyed. This technique is also relatively inexpensive (compared with GDMS). For these reasons, it was the technique of choice in our experiments. GDMS data was used as a means of calibrating SIMS results, thus making absolute concentration values available for all samples.

Two major modes of data collection were used – depth profile and full spectrum at a specific depth. In the former, only a few masses are being tracked while the ionic beam is ablating away material layers. In the latter, a full mass spectrum scan is performed at a specific depth.

Depth profile tracking. Several isotopes were chosen for this mode of tracking. These were ^{24}Mg , ^{25}Mg , ^{28}Si , ^{56}Fe , ^{142}Nd , ^{89}Y , ^{27}Al , ^{12}C , and ^{52}Cr . Selection was based on known influence of some impurities and/or dopants (Fe, Mg, and Cr), or on their prominence in the full spectrum (Si, C).

Values obtained for contaminants (Mg, Si, C, Fe, Mg, and Cr) were normalized to values for ^{27}Al and ^{89}Y , since there was some variability in signal strength from sample to sample.

Depth profile tracking data was taken from a total of seven samples representative of the experimental sample suite.

Full spectrum. In this case, the identification of individual peaks was carried out visually. Each peak's signal strength was calculated as the area under the curve. Background correction was achieved by means of subtracting the average signal over a range where no peaks could be visually identified. Isotope assignment was carried out using known isotope masses. A naturally occurring isotope frequency distribution was used to identify and verify the atomic identity of groups of peaks.

In some cases, interferences from atom pairs were observed. For example, the peak at 54 was normally assigned to $^{27}\text{Al}x2$. Peaks for the Nd group were found to be shifted by +1 or by +16. The former group was attributed to the pairing of Nd ions with H ions. The latter to the pairing of Nd ions with O ions. The peak at 149 au showed a significant departure from the naturally occurring isotope ratio of Nd (whereas the group of Nd isotopes paired with O ions did not have the anomaly at the corresponding isotope). This was attributed to the mass peak being contaminated by ^{133}Cs and ^{16}O pairs. A peak at 149 au was observed in YAG samples not doped with Nd, suggesting a source of contamination unrelated to Nd doping.

Full spectrum data was taken from four samples. A tabulation of these data are presented below in Table 3.4. These values were obtained by numerically integrating raw SIMS data around nominal atomic mass values.

Table 3.4

Mass (a.u.)	Primary assignment	Secondary assignment	Integrated Signal (arb. units)			
			YAG (AL)	Nd:YAG (SM)	Cr,Nd:YAG (AL)	Cr,Nd:YAG (SM)
12	¹² C		4.60E+03	5.42E+02	1.83E+03	1.14E+03
13	unknown		3.21E+04	3.06E+04	7.92E+04	5.18E+04
16	¹⁶ O		2.50E+06	2.87E+06	5.57E+06	3.89E+06
17	¹⁷ O		1.14E+03	2.64E+03	9.35E+03	4.57E+03
18	¹⁸ O		4.42E+03	5.54E+03	1.09E+04	7.58E+03
23	²³ Na		6.77E+02	5.11E+03	1.51E+04	4.92E+03
24	²⁴ Mg		2.05E+03	4.92E+02	1.25E+03	5.48E+02
25	²⁵ Mg		3.56E+02	3.04E+02	3.26E+02	2.13E+02
27	²⁷ Al		6.30E+07	6.01E+07	4.39E+07	5.21E+07
28	²⁸ Si	²⁷ Al + ¹ H	4.31E+03	2.14E+03	9.27E+03	8.89E+03
29	²⁹ Si		1.62E+02	3.24E+02	1.57E+03	7.08E+02
30	³⁰ Si		2.14E+02	1.49E+02	6.43E+02	2.35E+02
32	¹⁶ O x2	³² S	3.60E+05	2.76E+05	5.39E+05	4.86E+05
34	³⁴ S		1.05E+03	1.08E+03	2.15E+03	1.58E+03
35	³⁵ Cl		6.92E+01			
39	³⁹ K				6.29E+02	1.73E+02
40	⁴⁰ Ca	⁴⁰ Ar	8.63E+02	7.39E+02	9.93E+02	1.44E+03
41	⁴¹ K				1.59E+02	8.95E+01
43	²⁷ Al + ¹⁶ O		1.18E+06	2.20E+06	4.42E+06	2.93E+06
44	unknown		1.62E+05	9.15E+04	1.60E+05	1.80E+05
45	⁴⁵ Sc		1.68E+03	2.92E+03	8.00E+03	4.21E+03
50	⁵⁰ Cr				8.95E+03	5.05E+04
52	⁵² Cr				1.38E+05	7.45E+05
53	⁵³ Cr	²⁷ Al + ²⁶ Mg	1.13E+03	1.37E+03	7.87E+03	2.86E+04
54	²⁷ Al x2	⁵⁴ Fe	5.83E+05	5.26E+05	1.03E+06	8.72E+05
56	⁵⁶ Fe		1.07E+02	4.98E+01	2.53E+02	3.26E+02
58	⁵⁸ Ni		3.15E+02	5.02E+02	1.22E+03	7.46E+02
59	⁵⁹ Co		9.54E+02	3.32E+03	6.61E+03	3.43E+03
60	⁶⁰ Ni		1.32E+02	2.45E+01	3.85E+02	9.02E+01
62	⁶² Ni		1.58E+01			
89	⁸⁹ Y		1.30E+07	1.65E+07	2.40E+07	1.97E+07
100	unknown		4.48E+03	5.34E+01	1.66E+04	1.42E+04
106	⁸⁹ Y + ¹⁶ O		8.07E+06	1.77E+07	2.84E+07	1.95E+07
107	unknown		4.46E+03	8.29E+03	2.41E+04	1.67E+04
108	unknown		1.64E+04	3.50E+04	6.38E+04	4.06E+04
117	⁸⁹ Y + ²⁷ Al		3.07E+04	2.99E+04	4.17E+04	3.72E+04
122	unknown		6.65E+03	2.27E+04	3.78E+04	2.32E+04
133	¹³³ Cs		5.44E+04	1.70E+05	2.66E+05	1.62E+05
143	¹⁴² Nd + ¹ H			3.83E+04	5.92E+04	4.69E+04
144	¹⁴³ Nd + ¹ H			1.60E+04	2.47E+04	2.05E+04
145	¹⁴⁴ Nd + ¹ H			3.00E+04	4.85E+04	3.83E+04
146	¹⁴⁵ Nd + ¹ H			1.10E+04	1.57E+04	1.37E+04
147	¹⁴⁶ Nd + ¹ H			2.10E+04	3.31E+04	2.61E+04
149	¹⁴⁸ Nd + ¹ H	¹³³ Cs + ¹⁶ O	4.05E+03	1.62E+04	6.96E+04	3.47E+04
151	¹⁵⁰ Nd + ¹ H			5.71E+03	9.58E+03	7.72E+03
159	¹⁴² Nd + ¹⁶ O			1.99E+04	3.03E+04	1.95E+04
160	¹⁴³ Nd + ¹⁶ O			8.17E+03	1.32E+04	8.54E+03
161	¹⁴⁴ Nd + ¹⁶ O			1.58E+04	2.34E+04	1.63E+04
162	¹⁴⁵ Nd + ¹⁶ O			5.26E+03	8.33E+03	5.16E+03
163	¹⁴⁶ Nd + ¹⁶ O			1.11E+04	1.56E+04	1.09E+04
165	¹⁴⁸ Nd + ¹⁶ O			4.10E+03	6.58E+03	3.81E+03
167	¹⁵⁰ Nd + ¹⁶ O			3.30E+03	4.79E+03	3.41E+03

Table 3.4. (*Previous page*) Integrated signal values from SIMS data for several representative samples. Where values are omitted, integration was not performed because signal was indistinguishable from background. Values in boldface indicate that background was subtracted from this number.

Section 3.3.1.3

Combining GDMS and SIMS Data

As previously discussed, GDMS analysis was carried out on a piece of co-doped crystal supplied by Scientific Materials. A sample from the same boule was analyzed with SIMS. Here, an assumption was made that the two pieces had the same concentrations of all impurities. By simply taking the ratio of the ppma concentrations from GDMS data and signal levels from SIMS data, a means of calibration were achieved.

It was further assumed that ionic ejection rates were the same in all samples. That is, if two samples exhibited the same normalized signal for a given contaminant, they had the same concentration of this contaminant.

For a given sample and contaminant, the SIMS signal was calculated from full spectrum and depth profile data, normalized to ^{27}Al and ^{89}Y . This provided up to four estimates of SIMS signal. If multiple isotopes were present and identifiable, signals from all isotopes were added together (since GDMS did not distinguish between isotopes). These estimates were then normalized to the corresponding signals for the reference sample, and multiplied by the atom's concentrations from GDMS data.

Section 3.3.1.4

Uncertainty of Reported Data

Northern Analytical Laboratory states that the uncertainty of GDMS data is $\pm 25\%$. The uncertainty in reported values was calculated as a standard deviation of results from the various estimates of concentration. This uncertainty varied from less than $\pm 1\%$ to almost $\pm 15\%$, in some extreme cases.

Section 3.3.2

Results and Discussion

This Section presents results of analysis that combined the GDMS data with SIMS data, in the manner outlined in the previous section. These results are shown below in Table 3.5.

Table 3.5

Sample	Ca	Fe	K	Mg	Na	S	Si
Yag (AL) ³	1.0	0.7	0.0 ¹	1.7	0.5	7.2	9.0
Yag (SM,avg) ⁴	N/A	0.4	N/A	0.4	N/A	N/A	8.9
Yag (SM, high)	N/A	0.3	N/A	0.2	N/A	N/A	7.0
Cr,Nd:YAG (AL)	1.0	1.2	2.8	0.6	8.9	12.6	14.1
Cr,Nd:YAG (SM) ²	1.5	1.6	0.8	0.4	3.0	6.5	12.7
Nd:YAG (SM)	0.8	0.6	0.0 ¹	0.4	3.1	6.5	5.2
Nd:YAG (UC) ⁵	N/A	3.9	N/A	9.0	N/A	N/A	14.4

Table 3.5. Concentrations (in ppma) of various contaminants in the experimental sample suite. Data were derived from a combination of SIMS and GDMS tests. **Note 1:** the element is below the detectability threshold in the particular sample. **Note 2:** values for this sample (doped with 1.0 at% Cr, 1.2 at% Nd) from the GDMS test. All other samples' values are from the SIMS test. **Note 3:** "AL" stands for Airtron-Litton. **Note 4:** "SM" stands for Scientific Materials. **Note 5:** "UC" stands for United Crystals (doped with 1.2 at% Nd).

From the set of undoped YAG samples, the compositional analyses clearly indicate that the Scientific Materials high-purity sample was the least contaminated, while the sample from Airtron-Litton was the most contaminated.

A similar analysis of the data for the Cr³⁺,Nd:YAG samples shows that the co-doped sample from Scientific Materials had a generally comparable level of purity to that of the Airtron-Litton co-doped sample. Concentrations of K, Na, and S were significantly lower in the Scientific Materials sample. Finally, the United Crystals 1.2 at% Nd:YAG

was significantly more contaminated than the corresponding Scientific Materials Nd:YAG sample in all categories for which data were available.

Chapter 4 – Results of Gamma Irradiation at HERMES III

Chapter Summary

A number of samples covering all compositions being tested were irradiated at the High-Energy Radiation Megavolt Electron Source III (HERMES III) facility at Sandia National Laboratory. This facility provided fast pulses of high-energy photons; a fuller description of HERMES III follows below. Tests consisted of exposing samples to fast pulses of gamma radiation. Samples' transmission at 1064 nm (the principal operating wavelength of Nd:YAG lasers) was recorded in-situ. Steady-state optical absorption was also measured and differential absorption features were identified post-exposure.

This chapter covers the experimental methods used for collecting and processing the optical absorption response data at HERMES III. The subsequent sections cover both transient and permanent response of the samples to gamma irradiation. These sections identify some core behavior modes that generally describe the optical absorption response of the samples included in the experimental sample suite.

This is followed by numerical analysis and modeling of the transient data. The dynamics of the response are quantitatively broken down into discrete processes. The resulting models were fitted to the data.

Lastly, insights about the data gleaned from the analysis are combined with existing literature on color centers in YAG materials to provide a tentative picture of gamma-radiation-induced defects observed in these experiments. Thus, a picture consisting of data, modeling, and a physical interpretation is formed in this chapter.

Section 4.1

Method

Section 4.1.1

Experimental Setup at HERMES III

The High-Energy Radiation Megavolt Electron Source (HERMES) III facility at Sandia National Laboratory provides short, intense pulses of gamma-ray-equivalent photons with energies averaging 2 MeV. Experiments at HERMES III focused on observing the time evolution of the optical transmittance of YAG-based samples at 1064 nm when exposed to pulsed gamma radiation. Following gamma exposure, irradiated samples were later studied via optical spectroscopy methods to observe permanent changes in a wider range of optical properties induced by gamma radiation. These tests are described in subsequent sections.

Section 4.1.1.1

Description of HERMES III

The following description of HERMES III is based on the paper by Ramirez et al. (1989). This paper was presented at the Pulsed Power Conference in 1989, upon commencement of the facility.

At the fundamental level, the device operates by producing bremsstrahlung radiation by impinging a beam of accelerated electrons upon a heavy metal target. As electrons experience deceleration due to collisions with atoms, they emit energetic photons.

The accelerated electron beam is conducted along an evacuated channel. Acceleration is provided by a series of high-energy capacitors, which themselves are charged by Marx generators (maximum charging capacity of 95 kV, 156 kJ). The capacitors are discharged in sequence. Synchronization is achieved by using a pulsed laser (a sole, pulsed KrF excimer laser). The trigger beam is split into several parts, and each one is delayed by a specific amount of time, providing precise timing for the triggering sequence.

Based on the dosimetry acquired during the experiments conducted for this report, HERMES III delivered pulses with total dose ranging from 20 to 60 krad (Si). Given the nominal pulse duration of 30 ns, this translates to dose rates ranging from 0.7 to 2.0×10^{12} rad (Si) / sec.

Section 4.1.1.2

Physical Setup

As stated above, HERMES III experiments consisted of measuring a sample's relative transmittance at 1064 nm in order to observe its response to intense pulses of gamma radiation. Transmission was measured using a single-beam, double-pass geometry. For a given exposure, a sample's transmission immediately prior to the radiation pulse was recorded and was used in subsequent data analysis to define unity relative transmittance.

In order to protect the experiment's electronics from both the high doses of gamma radiation and from the Electro-Magnetic Pulse (EMP) that accompanies discharge of HERMES III, the experiment was separated into two parts. The first section was housed inside a shielded room. The shielded room was separated from the test chamber by a concrete barrier that provided protection from the gamma radiation. A grounded copper shell that enclosed the shielded room, as well as surge-protected circuits provided protection from the EMP. The second section of the experiment was located in the test cell, fully exposed to the radiation pulse. Communication between the two sections was achieved by carrying optical signals through fused silica optical fibers shielded with bags of lead shot.

The shielded section contained the probe laser source, optics for steering, focusing, and collimation of the beam, detectors, and data recording equipment. All of the experiment's electronic equipment was located in the shielded room. The second section, located in the test cell, contained optics for collimating light out of and focusing

light into the signal-carrying optical fibers, samples, and retro-reflectors. Figures 4.1 and 4.2 below show the two sections in detail.

In Figure 4.1 it can be seen that the Continuous Wave (CW) laser (Amoco ALC model 1064-150P) signal generated by a single laser operating at 1064 nm was equally split into four channels using 50/50 beam splitters. Each channel was used to analyze a separate sample. This way, four samples could be analyzed for each radiation pulse from HERMES III.

In the shielded room, microscope objectives (Newport 20x, NA 0.4) were used to inject light into fused silica multi-mode fibers which carried the light to the test cell. Signal information was returned from the test cell to the shielded room by the same fibers and extracted by the same microscope objectives. Fiber heads were positioned on tip-tilt stages with x-y-z translation for the purpose of optimizing the efficiency of coupling light into and out of the fibers.

Light returned by the fibers from the test cell was picked off by 50/50 beam splitters and then focused into detectors (EG&G YAG 100, nominal bandwidth 40 MHz). Band-pass filters were used to reject stray light, and to ensure that only the spectral band of interest was passed to the detectors. This return signal also sometimes passed through neutral density filters in order not to saturate the detectors. A stack of neutral density filters (with nominal optical density values of 0.3, 0.5, and 1.0) was used. The filters could be used in any combination. In most cases, no filters were actually used.

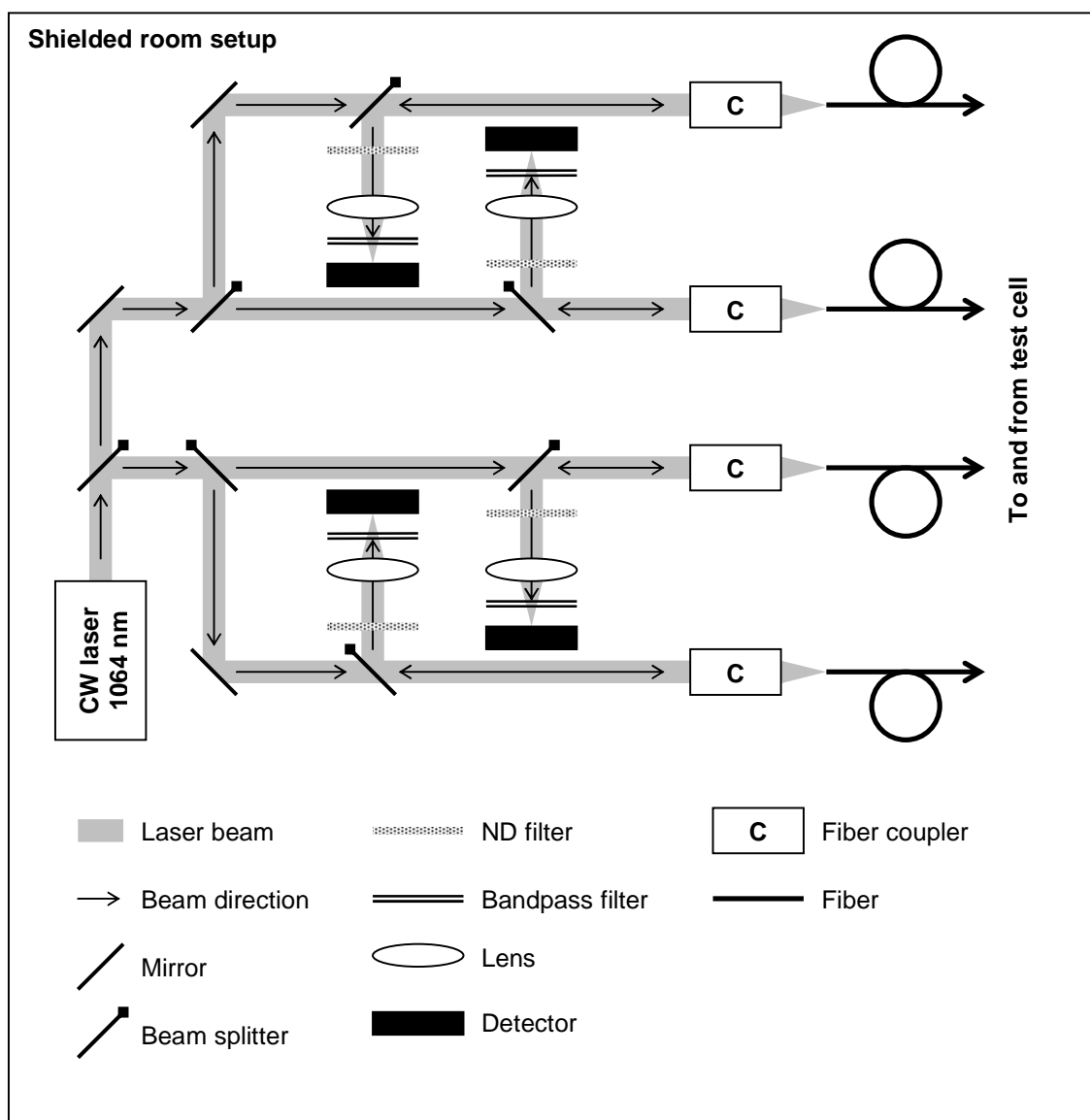


Figure 4.1. Experimental setup in the shielded room at HERMES III.

Signals from the four detectors were amplified using wide-band amplifiers (EG&G Model 5185, nominal bandwidth 100 MHz, ordinarily set to unit gain, DC coupling, zero DC offset, and 1 M Ω input impedance) and then recorded using a series of high-speed oscilloscopes (Tektronix 400 MHz 4-channel model, set to use 1 M Ω input impedance). A total of six oscilloscopes were used, each set to a different time resolution

and recording data on all four channels (resolution settings shown below in Table 4.1). Oscilloscopes were set in trigger mode. The trigger signal – synchronized with the discharge of HERMES III – was provided by the facility.

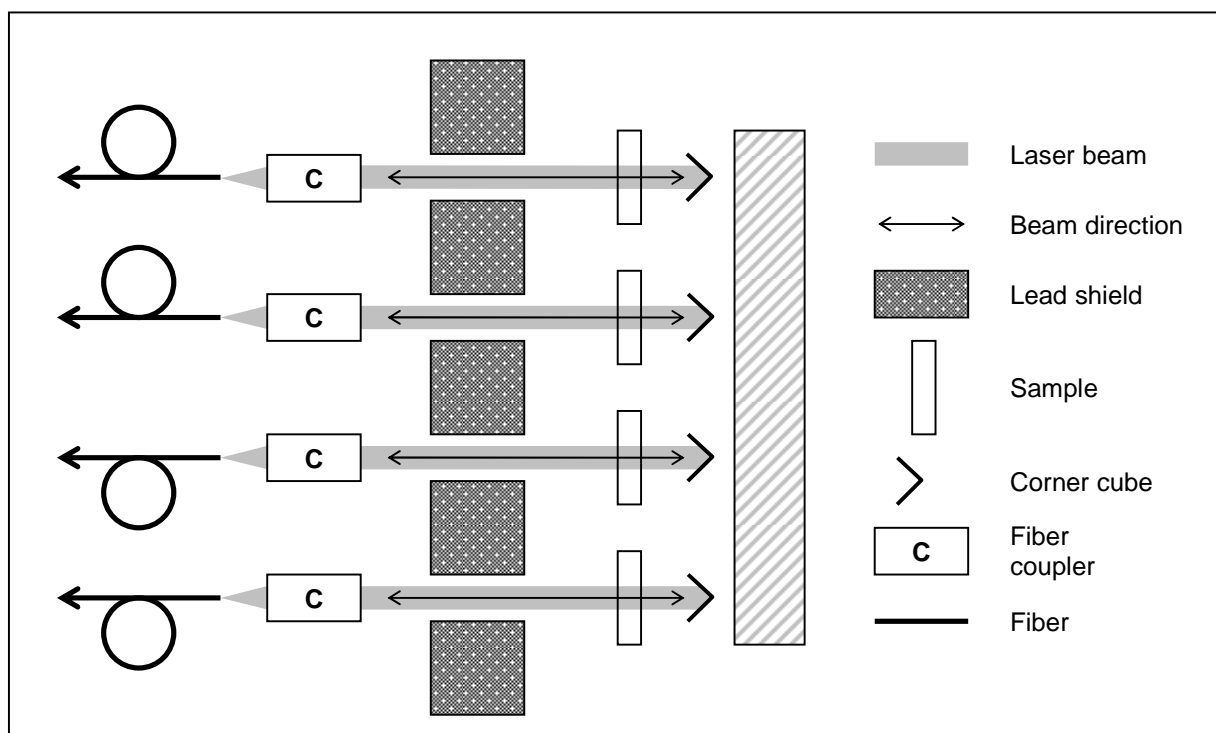


Figure 4.2. Experimental setup in the test cell at HERMES III.

The setup presented in Figure 4.1 was mounted on a movable breadboard that could be transported from one laboratory to another. This allowed for the setup to be built and pre-aligned in one laboratory, and then transported to the HERMES III facility, where only an alignment check and some minor adjustments had to be performed.

Figure 4.2 show the second half of the experiment, which was set up in the test cell, directly in front of the exit plate of the high-energy photon generator. Fiber collimators extracted light from and returned it into the optical fibers. These mounts were

set behind a shielding wall composed of lead bricks of approximately two inches in thickness. This wall protected the mounts and the optical fibers from effects of gamma radiation.

The samples were mounted on tip-and-tilt stages to allow for aligning them in the beam. Sample alignment, ensuring that the beam was optimally returned to the fiber after passing through the sample, was performed before the irradiation tests. Alignment was further checked after each discharge of HERMES III.

After exiting the fibers, laser light first passed through the collimators. The light then passed through the openings in the lead shield wall, through the samples for the first time, returned by corner-cube reflectors, through the samples for the second time, and was then injected by the collimators back into the original fibers.

The part of the experiment used in the test cell was completely mounted on a mobile breadboard, allowing for quick deployment of the experiment at the HERMES III facility. It was stored in a separate laboratory, where all major pre-experiment alignment could be completed before moving to HERMES III. Once there, only minimal alignment checks and adjustments were needed to bring the experiment to operation.

Optical fibers that ran through the test cell were covered with bags of lead shot while on the floor in order to prevent the generation of radiation-induced loss in the optical fibers that might have obscured the signal data from the test samples located on the test bed. The fibers were fed up to the test cell table through a lead pipe, with a wall thickness of approximately one half of an inch. The background system transmission during a gamma-ray pulse was tested by discharging HERMES III without any samples

in the channels, but recording transmittance data as described above. This was done in order to determine the effect of the ionizing radiation on the optical fibers and free-space alignment and coupling optics in the optical beam path. It was found, after repeated tests, that the system background transmission was unaffected by the ionizing radiation flux present in the test cell – neither gain nor loss were observed in any of the alignment/collimating optics or fibers.

Based on the data collected from the CaF_2 thermo-luminescent detectors (TLD) placed on the sample holders, total per-shot dose received by the samples ranged from approximately 8 krad (Si) to 69 krad (Si). Given the average pulse duration of 30 ns for a HERMES III pulse, this translates into average dose rates ranging from 0.3×10^{12} krad (Si) / sec to 2×10^{12} krad (Si) / sec. On average, the accuracy of the TLDs was reported to be $\pm 10\%$.

Section 4.1.1.3

Data Collection

As described above, the output of each detector in the shielded room was fed to a series of six storage oscilloscopes, each set to record data over a different time window. This produced six streams of data for each sample for each exposure event. Specifics of the data are presented in Table 4.1 below. Raw collected data consisted of voltages reported by the detectors.

Table 4.1

Oscilloscope	Time window	Time resolution
1	-4.8 ms to +20 ms	200 ns
2	-6 ms to +24 ms	2 μ s
3	-60 ms to +240 ms	20 μ s
4	-0.6 s to + 2.4 s	0.2 ms
5	-6 s to 24 s	2 ms
6	-20 s to +80 s	20 ms

Table 4.1. Oscilloscope settings.

Section 4.1.1.4

Data Processing

The raw data acquired was the signal voltage reported by the detectors. This signal needed to be converted into physically meaningful data, such as sample transmission or induced coefficient of absorption. Generally, data processing was carried out in four steps.

The first step was smoothing. Since data was also quite noisy and was significantly affected by digitization, noise reduction and smoothing was achieved by using a modified Savitzky-Golay algorithm (described below in Section 4.1.1.4). This operation is described in Equation 4.1 below. S_{raw} refers to the raw signal. SG refers to the smoothing operation. S_I refers to the output, the smoothed voltages.

$$S_I = SG\{S_{raw}\} \quad (4.1)$$

The second step was performing the DC offset correction, which is described below in Equation 4.2. The experiment used double-pass geometry in which the delivery and return path were combined. Therefore, retroreflections from all the optical components – such as fiber couplers – obscured the recorded signal. To find this DC offset, total signal levels for a given channel (DC_{sample} in Equation 4.2) and the signal level with the sample completely blocked (DC_{off} in Equation 4.2) were recorded prior to each radiation shot for each sample channel. The ratio of these two numbers was used to calculate the fractional amount of signal due to retroreflection at the time of the radiation pulse (to account for small drifts in laser's output). The detector voltage signal for $t < 0$ was, thus, divided by the above ratio to calculate the effective DC offset, which was then

subtracted from the whole data set. In Equation 4.2, S_2 represents the DC-corrected, smoothed signal. The angular brackets represent the time average.

$$S_2 = S_1 - DC_{block} \cdot \frac{\langle S_1(t < 0) \rangle_t}{DC_{sample}} \quad (4.2)$$

The third step was to calculate the relative transmittance of the sample under test (represented as T in Equation 4.3). This was calculated as simply the ratio of the time-dependent, DC-corrected signal to the averaged pre-radiation-pulse signal, as shown in Equation 4.3. Pre-irradiation sample transmittance for a given shot was taken as unity relative transmittance. Induced loss, then, would appear as transmittance values of less than one.

$$T(t) = \frac{S_2(t)}{\langle S_2(t < 0) \rangle_t} \quad (4.3)$$

In the fourth step, the induced coefficient of absorption was calculated (variable α in Equation 4.4) from the relative transmittance by using the Beer-Lambert as shown in Equation 4.4. Since the measurement was done in a double-pass geometry, the sample thickness z is doubled.

$$T(t) = \exp(-\alpha \cdot 2z)$$

$$\alpha(t) = -\frac{\ln(T(t))}{2z} \quad (4.4)$$

All of this processing was carried out automatically, using programs written in the Python programming language. The programs incorporated Python core libraries and the Numpy array computational library. The decision to use Python for processing was based on the language's ease of use and flexibility in dealing with multiple files and samples, so

that a single script could be used to process data from many samples without altering the code. Also, using this method all stages of processing could be contained in a single script, thus assuring uniformity of analysis.

Section 4.1.1.5

Modified Savitzky-Golay Smoothing Algorithm

This approach achieves reduction in signal noise by using local low-order polynomial regression. Generally, for a given point (x_n, y_n) a neighborhood of $2k+1$ points is considered: $\{(x_{n-k}, y_{n-k}) \dots (x_{n+k}, y_{n+k})\}$. A polynomial $P(x)$ of power p , such that $p < 2k + 1$, is fitted to this set of data using the least-squares parameter optimization. The value of y_n is then replaced with $P(x_n)$.

To prevent smoothing of data around $t = 0$, each data set was split into two halves, for $t < 0$ and $t \geq 0$. Had the data been treated as just one set, the application of such a neighborhood-of-points method would have artificially shifted the values of points for $t \rightarrow 0^-$ to follow the trend of data for $t \rightarrow 0^+$. This would have made it appear as though the samples were reacting to gamma radiation before the arrival of the pulse, thus violating causality. The segregation of the data in two sets segregated at the time, $t = 0$ of the discharge of the gamma radiation pulse, avoided this issue.

In addition, the Savitzky-Golay method has an ambiguity near beginning and end of data sets for the n^{th} points, such that $n < k$ and $n > N - k$ (where N is the total number of points in the set). The algorithm was modified to resolve this ambiguity. The fit centered on (x_k, y_k) was used to provide values for $x_{n < k}$ (the other end of each data set was treated in a similar manner).

Section 4.1.2

Differential Absorption Spectroscopy

Pre and post-exposure optical absorption measurements were carried out using a Perkin Elmer Lambda 950 UV-Vis-NIR spectrophotometer in the same manner as described in the Chapter III, Section 3.2. However, since in this part of the report steady-state changes in samples' absorption are of interest, a differential absorption technique is applied. As stated, before (Chapter III, Section 3.2), this instruments reports absorbance values. Differential absorbance (DA) is obtained by subtracting a pre-irradiation (reference) absorbance (or optical density) spectrum (A_{ref}) from a post-irradiation spectrum (A_{post}) taken from the same sample and over the same spectral window, as shown in Equation 4.5:

$$DA(\lambda) = A_{post}(\lambda) - A_{ref}(\lambda) \quad (4.5)$$

It was then further assumed that while absorption may have changed, Fresnel reflection contribution to the reported absorbance values were not altered significantly. Based on this assumption, Fresnel contributions in A_{post} and A_{ref} are identical, and cancel out in calculation of DA . Similarly to Equation 4.4, it is possible to use the Beer-Lambert Law to connect differential absorption to the induced coefficient of absorption ($\Delta\alpha$), as shown below in Equation 4.6. Note, that since the spectrometer works in the single-pass geometry, sample thickness z is not doubled.

$$DA(\lambda) = -\log(T(\lambda)) = -\log(\exp(-\Delta\alpha(\lambda)z))$$

$$\Delta\alpha(\lambda) = \frac{DA(\lambda)}{z \log(e)} \quad (4.6)$$

It is possible for $\Delta\alpha$ to assume both positive and negative values. When $\Delta\alpha$ is negative, it is implied that the sample has become more transparent in this spectral region. When it is positive, the sample has become less transparent in the given spectral region.

Section 4.2

Data and Results from HERMES III

Numerous samples from the available sample suite were tested at HERMES III. The samples that were tested included undoped YAG samples (of three different purity levels), Nd:YAG samples (of three different Nd concentration levels), Cr³⁺:YAG samples (of three different Nd concentration levels), and Cr³⁺,Nd:YAG samples (of three different co-dopant concentration combinations). A complete description of the sample suite is provided in Chapter III. Multiple samples of each composition were tested and multiple shots were taken on many of the samples. A representative subset of the experimental data is depicted in the chapter that follows.

Experiments consisted of in-situ tests measuring time-dependent transmittance at 1064 nm (this technique is described in Section 4.1.1 of this Chapter) and post-irradiation differential absorption measurements (this technique is described in Section 4.1.2 of this Chapter). These tests are described in the following Sections – 4.2.1 and 4.2.2, respectively – broken down by composition.

As no permanent changes were observed in the Cr³⁺:YAG samples, only their transient response is discussed in this chapter.

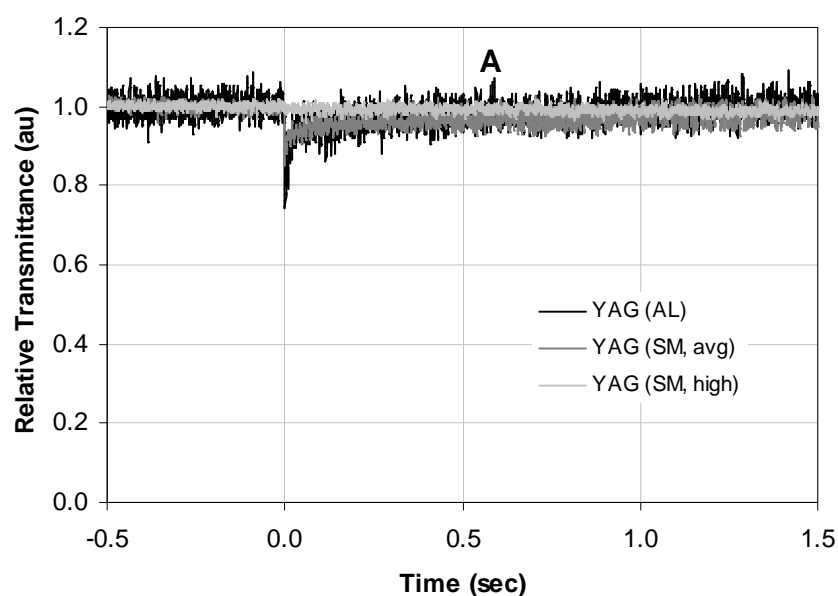
Section 4.2.1

Transient Response to Gamma Irradiation

Section 4.2.1.1

Undoped YAG

In experiments at HERMES III, it was observed that undoped YAG samples exhibited transient induced absorption at 1064 nm due to pulses of highly energetic gamma photons. These data are presented in Figure 4.3. This figure presents both the relative transmittance data (Figure 4.3A) and the induced coefficient of absorption data (Figure 4.3B). The subsequent discussion, however, will focus exclusively on the induced coefficient of absorption data, as it is length-normalized and bears greater physical significance.



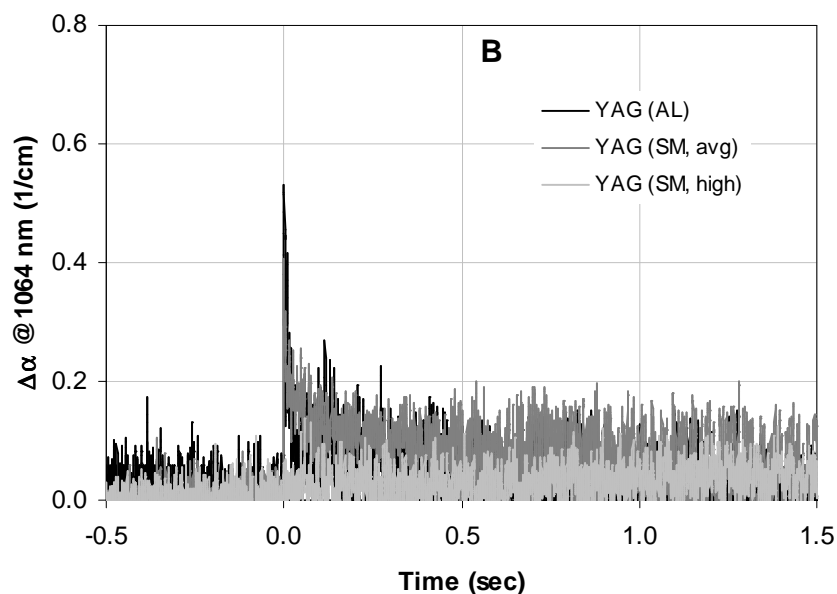
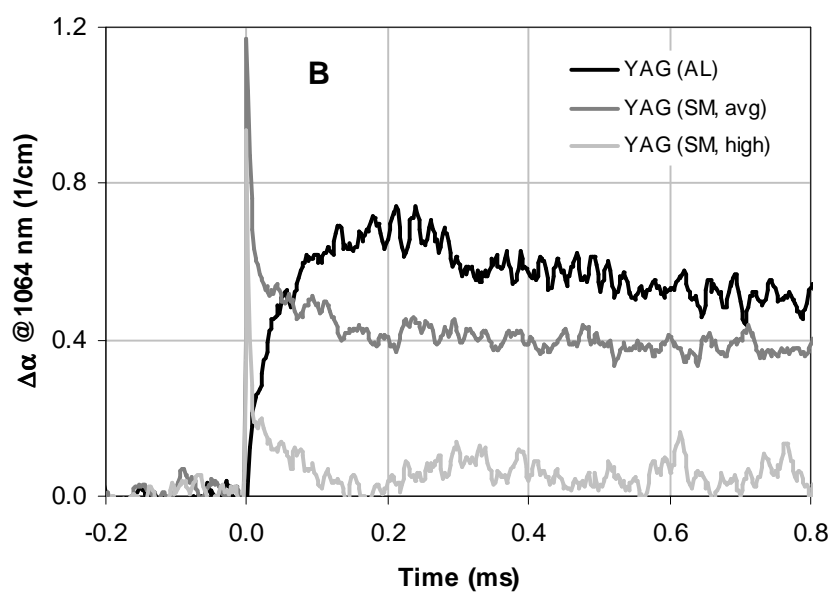
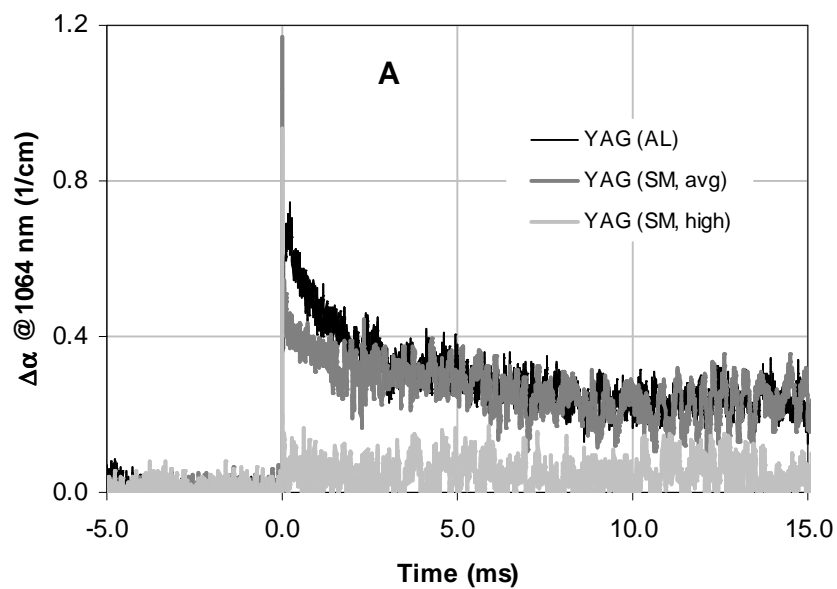


Figure 4.3. Time dependence of absorption at 1064 nm in undoped YAG induced by a single fast pulse of 2 MeV photons. A – data presented in the relative transmittance form. B – data recalculated as induced coefficient of absorption.

Figure 4.3 shows that all three undoped YAG samples experienced a loss of transmittance due to exposure to the pulse of gamma radiation. However, within less than 0.5 seconds all the samples experience a near-complete recovery. Within the time frame of the figure, the samples recover to pre-irradiation transmittance to within the experimental error.

It is instructive to examine the data on shorter time scale, as presented in Figure 4.4 below, which presents the same data on successively faster time scales.



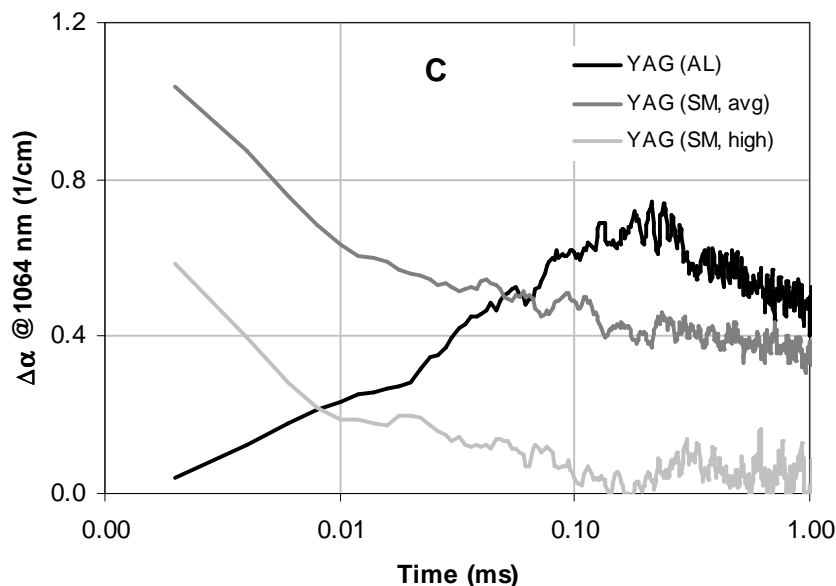


Figure 4.4. Time dependence of absorption at 1064 nm in undoped YAG induced by a single fast pulse of 2 MeV photons, presented on shorter time scales. Plots **A** and **B** are presented on linear-linear scales, while plot **C** is presented as log-linear.

The three samples presented here differ in their manufacturer and purity, as outlined previously (Section 3.3.2). For example, the Airtron-Litton sample contained 0.7 ppma of iron. The average quality Scientific Materials sample contained 0.4 ppma of iron, and the high-purity Scientific Materials sample contained only 0.3 ppma. From the data in the Figure 4.4A it is clear that the amplitude of radiation-induced absorption was significantly impacted by the sample purity. Specifically, the induced absorption (specifically, its value integrated over the time window) was seen to increase with higher levels of contamination. The Airtron-Litton sample (the least pure of the three) had the greatest amount of induced loss, while the Scientific Materials high-purity sample had the least amount of induced loss.

In addition to differing amplitudes of absorption response, Airtron-Litton and Scientific Materials' samples had functional differences in their instantaneous response to gamma radiation. These differences are exemplified in Figures 4.4B and 4.4C. In particular, it can be seen that while the onset of induced absorption in the Scientific Materials samples is essentially instantaneous (up to the experimental time resolution), the onset of absorption in the Airtron-Litton sample takes place over a finite period of time (approximately 0.2 ms).

The data in Figure 4.4B further indicates that while time-integrated induced absorption in the two Scientific Materials samples is different, the instantaneous peak values at $t = 0$ is rather close.

Upon visual examination of the data, the absorption relaxation process can be generally broken down into two components – “fast” and “slow.” This is especially evident in the log-linear plot of the data (Figure 4.4C), which shows that the data roughly consists of two straight-line segments, indicating two exponential components. The former, “fast,” component has lifetime on the order of 10 μ s. The “slow” component has lifetime on the order of 10 ms or longer.

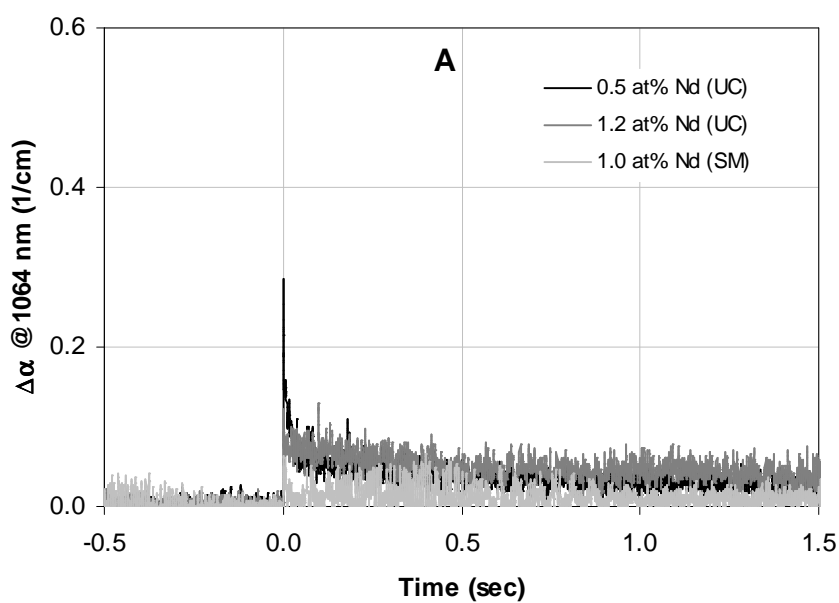
In terms of this representation, the difference between the Scientific Materials' samples and the one from Airtron-Litton is that the latter does not have the fast component. The slow component, however, appears to be very similar between all three samples, the only difference being its amplitude.

An in-depth quantitative modeling discussion of these data is carried out below, in Section 4.3.2.1.

Section 4.2.1.2

Nd:YAG

Characteristic data for the induced absorption response of the three different Nd:YAG materials tested is presented in Figure 4.5. Aside from differing manufacturers, samples obtained from United Crystals and from Scientific Materials also differed in purity (as detailed in Chapter III, Section 3.3.2), with the samples from United Crystals having significantly higher levels of contamination.



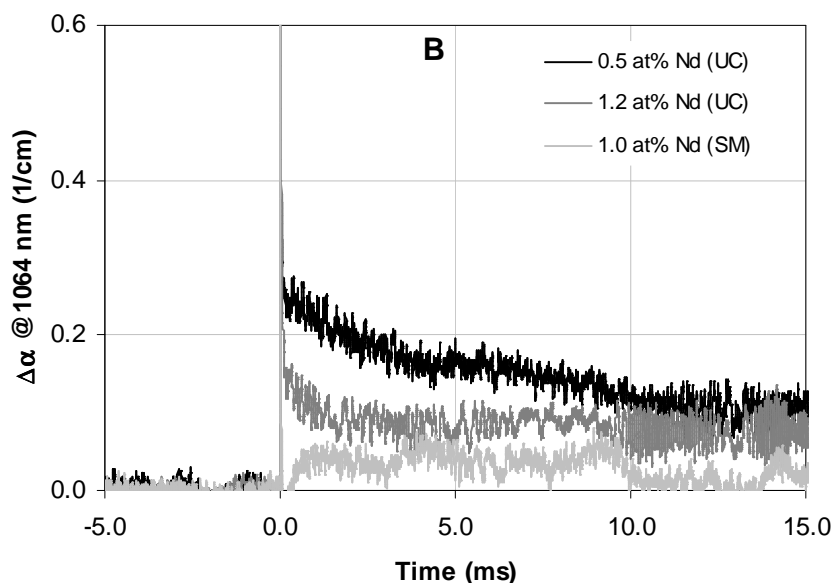


Figure 4.5. Time dependence of absorption at 1064 nm in Nd:YAG samples induced by a single fast pulse of 2 MeV photons. Figures A and B present the data on two different time scales. UC are United Crystals samples while SM indicates the Scientific Materials sample.

Figure 4.5A indicates that the Nd:YAG samples generally follow the pattern of behavior similar to the undoped YAG samples. The Nd:YAG samples respond to the flux of gamma radiation with an immediate onset of absorption at 1064 nm, peaking at approximately 0.4 cm^{-1} . The induced absorption then largely decays away within 0.5 seconds. A relatively small amount of induced absorption remains and appears permanent, contributing less than 0.04 cm^{-1} of absorption.

Examination of the data clearly shows the effect of increasing the Nd concentration in the crystal. The more highly doped Nd:YAG exhibits a significant reduction in both the magnitude and relaxation time of the transient induced absorption in the samples. This can be seen by comparing the spectra for the two compositions of

United Crystals Nd:YAG samples. The effect of contamination, however, is perhaps even more pronounced. Although the SM sample had a lower Nd concentration, its purity was much greater than that of the UC samples and its transient radiation response was pronouncedly better than that of the other samples. Thus, in agreement with the trend observed with the undoped YAG samples, the Nd:YAG samples appear to experience a greater degree of induced absorption for samples with greater levels of contamination. The Scientific Materials sample had lower levels of contamination, and accordingly remained more transparent.

In addition to variations in response amplitude, functional differences in behavior were also observed among the Nd:YAG samples. Similarly to the undoped YAG samples, some Nd:YAG samples had a near-instantaneous onset of absorption, while some had a delayed increase in absorption. In the case of the Nd:YAG samples, however, samples of the two types of behavior came from the same manufacturer (United Crystals).

A further differentiation in behavior can also be identified. This division applies exclusively to samples that had near-instant onset of absorption. In this group, samples formed two sub-groups. The difference between the two groups is that induced absorption in one group appears to dip below the other group. The first group's induced absorption then recovers to the second group's level. The two groups behave in an essentially identical manner past 0.5 ms. Representative induced absorption curves from the two groups are shown below in Figure 4.6.

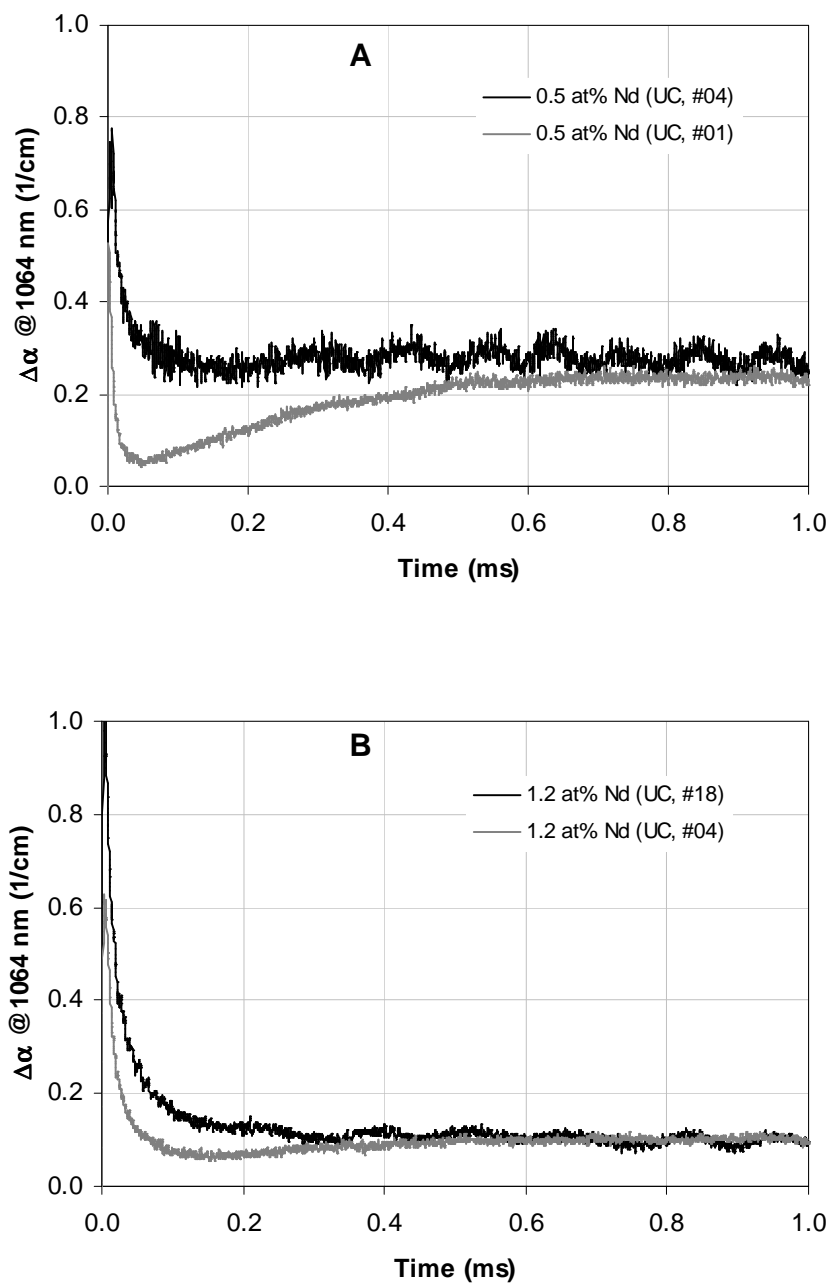


Figure 4.6. Different modes of behavior observed in the United Crystals Nd:YAG samples. The difference is the relatively negative deviation observed most clearly from the onset of absorption and until approximately 0.2 ms. Data curve labels refer to specific samples of the same nominal composition. A: 0.5 at% Nd:YAG. B: 1.2 at% Nd:YAG.

Each sample appears to display only one type of behavior described above. Analysis of experimental condition records did not establish a correlation between a mode of behavior and such conditions as dose rate, particular data collection channel, or a specific discharge of HERMES III. Therefore, these differences can fairly confidently be assigned to the samples themselves.

Based on the observed groupings of sample behaviors, it is possible to break down the overall behavior into three general processes, in a manner similar to that applied to the undoped YAG samples.

Two of the process components are the same as with undoped YAG – a fast and a slow absorption process. Although the amplitudes of these processes appear lower in the Nd:YAG samples, their lifetimes appear generally similar. The third process component – evident in the curves presented in Figure 4.6 – appears to have a negative amplitude and an intermediate lifetime (200 – 500 μ s). Because of its negative amplitude, it is not an absorption but an amplification process. Therefore, this third process component represents gain.

These processes can further be compared on log-linear plots, similar to the previous section (Figure 4.4C). The log-linear plots of the data presented in Figure 4.6 are shown below in Figure 4.7.

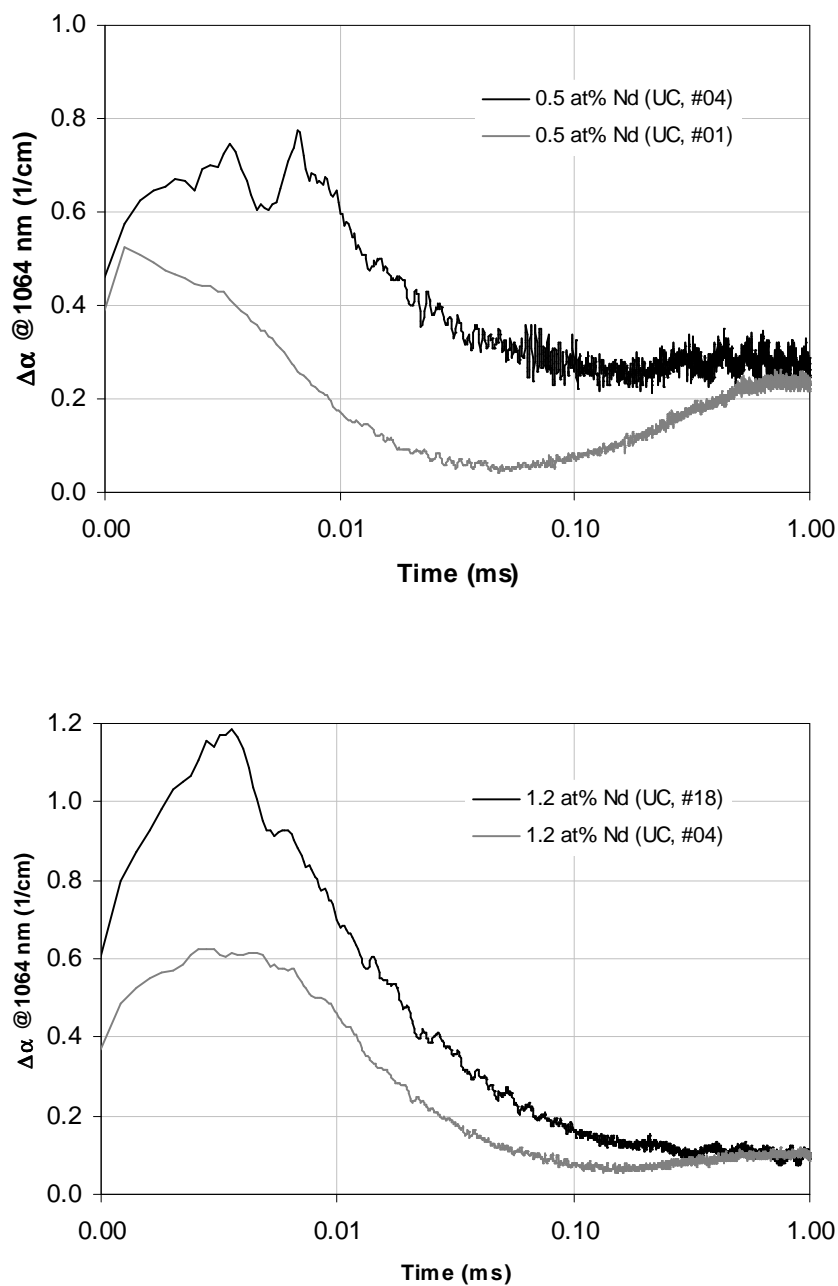


Figure 4.7. Log-linear plots of the induced absorption curves from Nd:YAG samples in response to an individual pulse of 2 MeV photons. Samples and data are the same as used in Figure 4.6.

The nature of the curves seen in Figure 4.7 is not strictly linear, which suggests that the behavior is, at least, a combination of several exponential processes, possibly overlapping in their lifetimes. As was suggested previously, the gain process and the fast absorption process may be fairly close in their lifetimes, yielding the smooth curves seen in Figure 4.7 above. An in-depth analysis of the components comprising the transient response of the co-doped samples is provided later on in Section 4.3.2.2.

Section 4.2.1.3

Cr^{3+} :YAG

Representative results of Cr:YAG data from the gamma radiation tests are presented in Figure 4.8. This group consisted of two concentration levels from United Crystals (0.5 at% Cr and 2.0 at% Cr) and one concentration level from Scientific Materials (1.5 at% Cr).

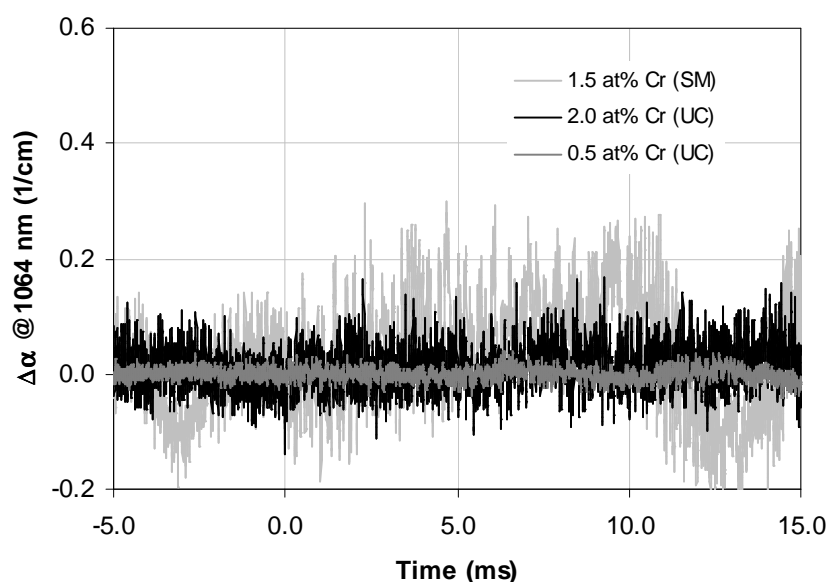


Figure 4.8. Time dependence of absorption at YAG samples doped with various quantities of Cr. Oscillations in the 1.5 at% Cr:YAG sample (light grey curve in the background) are attributed to instrumental noise.

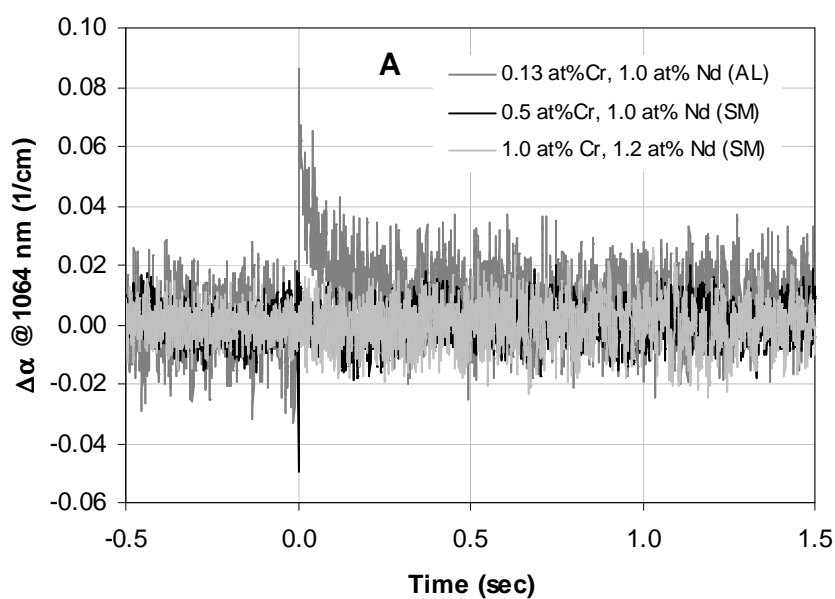
As can be seen in Figure 4.8, the behavior of all Cr:YAG samples tested was essentially identical. No significant response in the form of induced absorption at 1064 nm was detected. Optical absorption response observed in the United Crystals samples was, within experimental accuracy, a flat line. Data for the Scientific Materials sample

included strong signal oscillations. Their origin cannot be exactly attributed. However, the observation that samples of other compositions did not exhibit such oscillatory behavior points toward this being instrumental noise rather than a real physical phenomenon. It is worthwhile to note that the radiation hardness of these materials is independent of sample purity, manufacturer or composition for these samples.

A change in the samples was, nonetheless, observed. Immediately following irradiation with high-energy photons, Cr:YAG samples changed their color from green to brown. Similar color changes were observed in the same samples when exposed to intense pulses of UV radiation during UNPP experiments (described in Chapter V). Since coloration in the UV experiments was connected to measurable absorption at 1064 nm, a more thorough statistical analysis was carried out on these HERMES data. This analysis is described in the *UV Irradiation* chapter of this report (Chapter V, Section 5.2.1.3).

Section 4.2.1.4 **$Cr^{3+}, Nd:YAG$**

Three material compositions were tested in this category. The first was from Airtron-Litton, with composition 0.13 at% Cr, 1.0 at% Nd. The second was from Scientific Materials, with composition 0.5 at% Cr, 1.0 at% Nd. The last was also from Scientific Materials; its composition was 1.0 at% Cr, 1.2 at% Nd. Their ionizing-radiation response curves are shown in Figure 4.9.



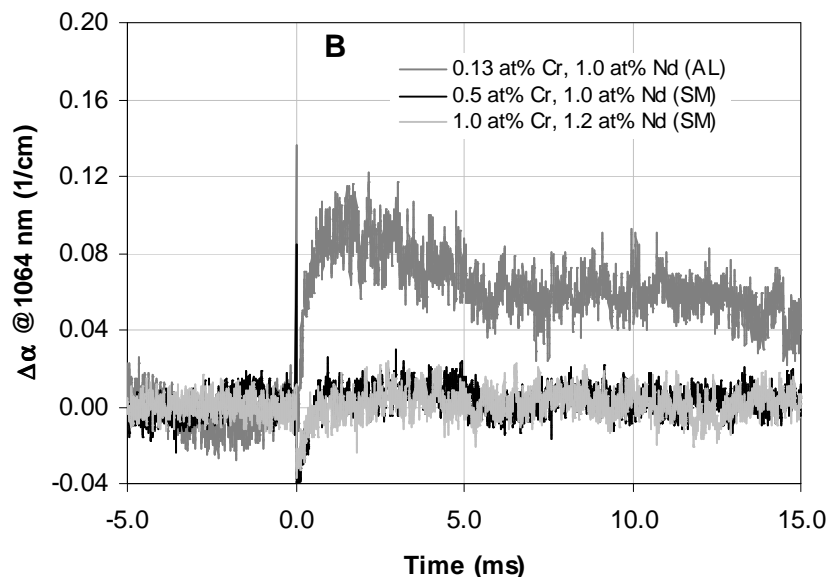


Figure 4.9. Time dependence of absorption at 1064 nm Cr^{3+} , Nd:YAG samples induced by a single fast pulse of 2 MeV photons. Reported negative absorption corresponds to induced gain at 1064 nm. A: Data on the seconds scale. B: Data on the milliseconds scale.

From the figure, it can clearly be seen that the behavior of the 0.13 at% Cr sample was dominated by a relatively slow absorption process that had a finite, measurable onset, functionally similar to that observed in the Airton-Litton undoped YAG sample shown in Figure 4.4B (though the amplitude of the absorption response was an order of magnitude lower for the above co-doped YAG sample). The onset of increased absorption was followed by its gradual decay. Similarly to the undoped YAG and Nd:YAG samples, this low-chromium sample has largely recovered its transmittance within 0.5 seconds.

In contrast, short-term gain is clearly observable in the Scientific Materials' samples immediately following exposure of the samples to the ionizing radiation pulse.

The gain curve (reported as negative induced absorption) is followed by a slight but measurable amount of longer-term absorption. The persistence and exact contribution of this absorption is difficult to ascertain, since its amplitude is very close to the noise amplitude.

A further comparison of the Cr,Nd:YAG samples to the Nd:YAG samples can be carried out via log-linear plots, shown below in Figure 4.10. This figure shows the same samples and data as Figure 4.9, except the time axis is plotted as a log scale.

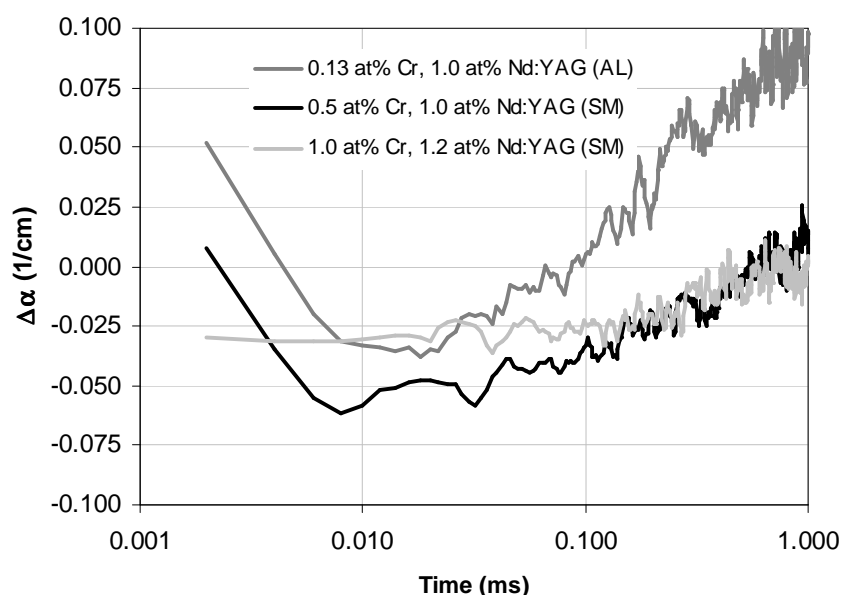


Figure 4.10. A log-linear plot of the data from Figure 4.9. Induced absorption response of Cr,Nd:YAG samples to a pulse of 2 MeV photons.

The first observable difference between the plots in Figure 4.10 and in Figure 4.7 is that response of the co-doped samples has a much more linear functionality. This means that the complex composition of the absorption response of the Nd:YAG samples is not seen in the co-doped samples. The response of the co-doped samples can more

readily be explained in terms of a minor slow absorption process and a gain process similar to that observed in some of the Nd:YAG samples. An in-depth analysis of the components comprising the transient response of the co-doped samples is provided later on in Sections 4.3.2.3 and 4.3.2.4.

An important observation to be made here is that, completely unlike the Nd:YAG samples, the high-chromium co-doped samples did not experience a measurable loss of transmittance, neither transient nor permanent. Therefore, we can note that under the conditions of this experiment, the high-chromium Cr,Nd:YAG samples proved to be radiation-hardened when compared to their Nd:YAG equivalents.

Section 4.2.2

Permanent Response to Gamma Irradiation

Section 4.2.2.1

Undoped YAG

As described in the Method section above (Section 4.1.2), absorption spectra were taken before and after the gamma irradiation treatments to determine the permanent effect of ionizing radiation on the materials. Figure 4.11 below shows differential absorption induced in two of the undoped YAG samples. The composition purity of these samples has been discussed earlier (Chapter III, Section 3.3.2). While a number of contaminants were identified, the Airtron-Litton (AL) sample was generally the most contaminated (e.g., 0.7 ppma of iron). The samples from Scientific Materials were generally more pure, with the average-purity samples (SM, avg) containing approximately 0.4 ppma of iron, and the purest sample (SM, high) containing approximately 0.3 ppma of iron.

Examination of Figure 4.11 shows that the differential absorption spectrum consists of a negative and a positive component. The negative contribution is seen to peak near 252 nm, a location that has been attributed to Fe^{3+} absorption, while the positive contribution peaks near 320 nm and then extends across the visible spectrum and into the NIR, reminiscent of the Fe^{2+} absorption spectrum. It can be further noted that the sample with the lower iron concentration reported by mass spectroscopy (Scientific Materials high purity) exhibits less induced absorption. Maxima, minima, and total doses received by the samples are listed below in Table 4.2

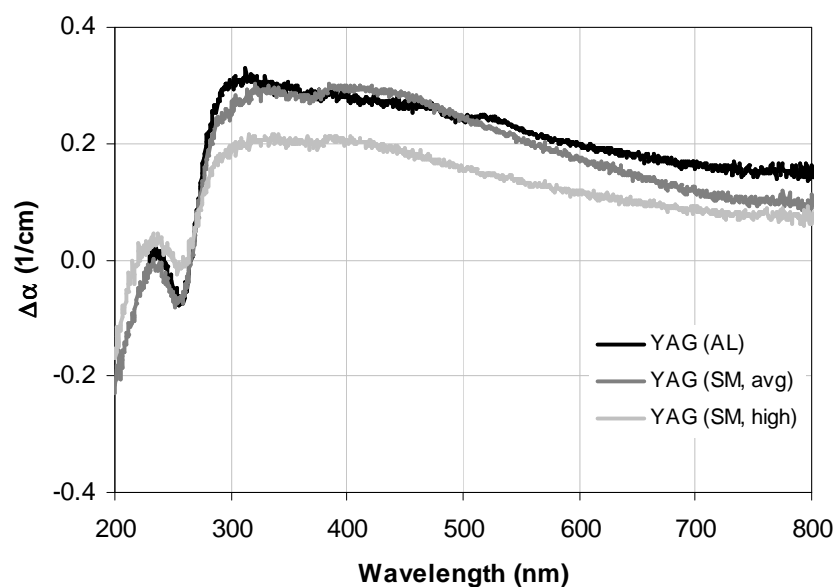


Figure 4.11. Differential absorption spectroscopy data showing permanent induced absorption in undoped YAG samples due to gamma irradiation at HERMES III.

Sample	Min $\Delta\alpha$ (cm^{-1})	Max $\Delta\alpha$ (cm^{-1})	Total dose (krad (Si))
YAG (AL)	-0.08	0.33	76.8
YAG (SM, avg)	-0.08	0.30	320.6
YAG (SM, high)	-0.03	0.22	123.5

Table 4.2. A summary of the extrema of induced absorption in undoped YAG samples, along with the total dose received by these samples. Minima are stated for the wavelengths above 230 nm.

It should be noted that the pre-irradiation spectrum for the Airtron-Litton sample was initially recorded with a faulty baseline, an error which was not discovered until after the gamma irradiation. Therefore, the data presented here uses a reference spectrum obtained from this sample after annealing it in air at 500 °C. This temperature setting was used in thermal treatment of other irradiated samples, and was chosen to relax the divalent iron color centers.

Section 4.2.2.2

Nd:YAG

A similar analysis has been performed for the available Nd:YAG samples. These data are presented in Figure 4.12 below.

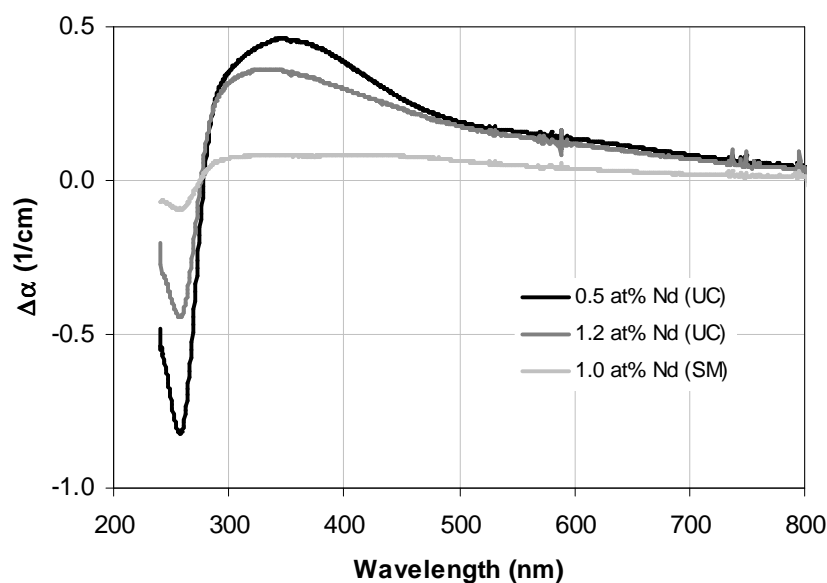


Figure 4.12. Differential absorption induced in Nd:YAG samples by gamma irradiation at HERMES III.

Similar to the results observed for samples of undoped YAG, the differential absorption of the Nd:YAG samples is composed of both a negative and a positive component. The negative peak reaches its minimum at approximately 250 nm, while the positive peak reaches its maximum near 320 nm, and then continues across visible part of the spectrum and into the NIR. Minima, maxima, and the total doses are listed below in Table 4.3.

Sample	Min $\Delta\alpha$ (cm^{-1})	Max $\Delta\alpha$ (cm^{-1})	Total dose (krad (Si))
0.5 at% Nd:YAG (UC)	-0.82	1.30	76.3
1.0 at% Nd:YAG (SM)	-0.51	0.08	142.7
1.2 at% Nd:YAG (UC)	-0.50	1.12	76.6

Table 4.3. A summary of the extrema of induced absorption in undoped YAG samples, along with the total dose received by these samples.

Again, the amplitude of induced absorption is positively correlated with concentration of the iron impurity in the samples. Samples with 0.5 at% Nd and 1.2 at% came from United Crystals (and can be assumed to have similar quality), while 1.0 at% Nd:YAG came from Scientific Materials. According to mass spectroscopy data (Section 3.3.2), the Scientific Materials' sample had 6.5 times less iron than the United Crystals sample. Areas under the positive parts of the curves in Figure 4.12 (calculated as a numerical integral between 279 nm and 800 nm) can be compared between the three samples. This comparison reveals that the 1.2 at% Nd:YAG sample had 3.5 times as much absorption, and 0.5 at% Nd:YAG sample had 4 times as much absorption as the Scientific Materials sample. While the agreement between optical spectroscopy and mass spectroscopy is not exact, the trend in impurity concentration between SIMS and absorption spectroscopy data shows a correspondence.

Section 4.2.2.3

Cr³⁺,Nd:YAG

As with the transient induced absorption results, the two types of samples available for study showed vastly different modes of behavior in the case of stable (steady-state) induced absorption. Data from the low-chromium Airtron-Litton sample (0.13 at% Cr³⁺, 1.0 at% Nd) and the high-chromium Scientific Materials sample (1.0 at% Cr³⁺, 1.2 at% Nd) are shown in Figure 4.13.

Examination of the data in the figure reveals that for the Airtron-Litton sample, the differential absorption spectrum consists of several broad peaks in the UV and visible, with changes terminating below 600 nm. Further, there is a significant increase in the UV absorption, with a peak at 275 nm. Another broad peak follows at 480 nm.

Differential absorption data on the Scientific Materials sample consists of a slope composed of very broad peaks. Its maximum contribution is in the UV, and it slowly decreases in amplitude across the visible and NIR, terminating near 1000 nm.

The unique behavior of the Scientific Materials sample prompted a further investigation. One of the slices was sectioned into smaller sub-samples (measuring 7 mm x 7 mm). The cutting pattern was hexagonal – one sub-sample was at the core of the original sample, with the other six were taken from the outside. It was found that differential absorption shown in Figure 4.13 decreased away from the core, as examined below in Figure 4.14.

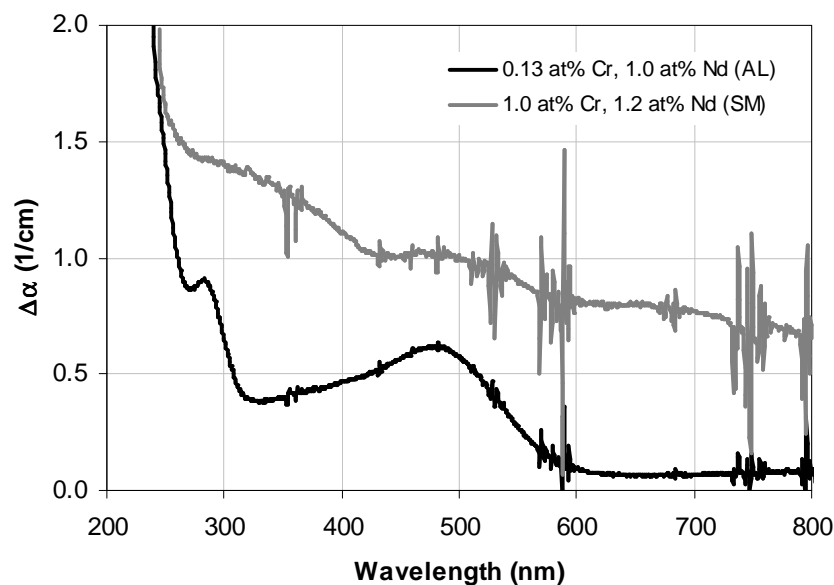


Figure 4.13. Differential absorption in Cr,Nd:YAG due to pulsed gamma irradiation at HERMES III.

Analyzing various spots within the sample, it was found that the induced loss is well-correlated with regions of striations and core in the sample. By comparison, regions free of such striations show a minimal increase in induced loss, as seen below in Figure 4.14. This figure shows that as examination of the material moves away from the core – which is the most heavily affected by striations, as seen in Figure 4.15 – the amount of induced absorption drops off dramatically. Whereas the sample from the core registered a maximum increase of almost 2 cm^{-1} (for $\lambda = 300 \text{ nm}$), the sample from near the edge registered an increase of only 0.6 cm^{-1} at the same wavelength.

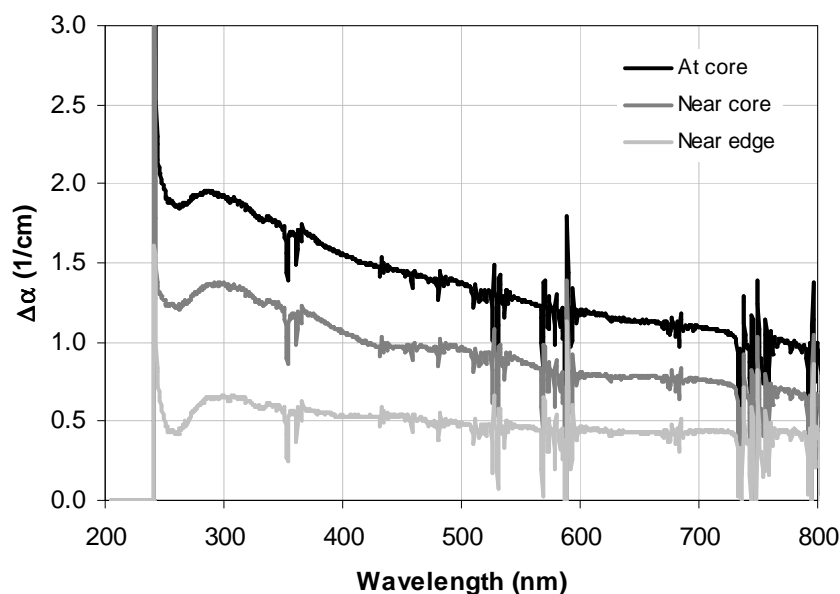


Figure 4.14. Sampling of differential absorption induced by gamma irradiation in a Scientific Materials Cr,Nd:YAG sample. The three regions tested had differing amount of striations detected, with the core region most heavily affected, and the outer region least affected.

Shadow imaging was used to further observe radial differences in the co-doped Scientific Materials sample. If significant variations in the index of refraction were present in the sample, they would appear as dark areas (shadows) in the resulting image. A false-color representation of such an image is shown below in Figure 4.15. Shadow imaging was performed by passing a diverging laser beam (from a HeNe laser operating at 632.8 nm) through a sample, and then projecting it on a white paper screen. A digital camera (Canon Digital Rebel XT EOS) was used to capture these images. A background image without a sample in the beam path was first captured. This background image was then subtracted from images of the sample and the false-color image calculated from the subtraction residual using a Python script (employing the Python Imaging Library).

It is apparent from Figure 4.15 that the sample is not homogeneous, and in fact includes a distinct core (a high-refractive-index core is a known YAG growth defect, Willis and Dixon 1968) as well as radial striations. Since the anomalous differential absorption appears to correspond to the core and its accompanying striations, it is likely that these variations in stress and density that are responsible, and not some other process attributable to the material composition.

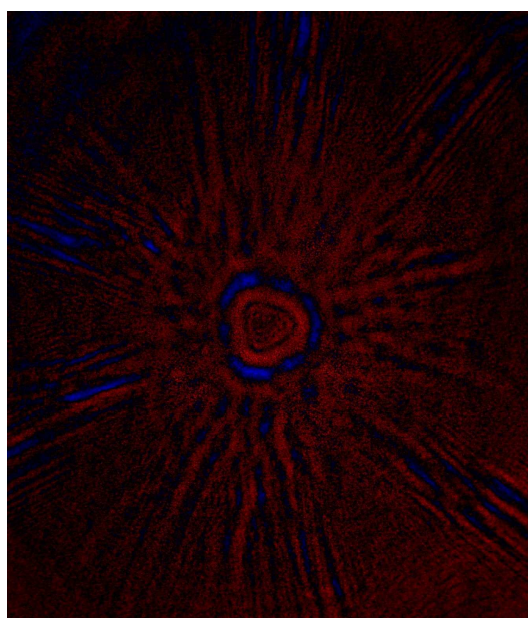


Figure 4.15. False-color representation of a shadow image of a Scientific Materials co-doped Cr,Nd:YAG sample. Blue represents dark regions, red represents the bright, and black represents no change in brightness. Central core and radial striations are clearly visible indicating radial variation in the index of refraction of the sample.

Shadow imaging of the co-doped samples from Airtron-Litton (the low-chromium composition) revealed no such striations. Therefore, losses observed in the co-doped Airtron-Litton samples cannot be attributed to the same causes as the losses observed in some of the co-doped Scientific Materials samples.

Section 4.3

Data Analysis

Several types of numerical analysis have been carried out on the data described above in Section 4.2. A correlation between dose and induced transient absorption at 1064 nm is described below in Section 4.3.1. Modeling of the transient response is further discussed below in Section 4.3.2, whereby the transient response curves are broken into a sequence of decaying exponentials. This latter type of analysis was carried out in order to more consistently compare the various behaviors observed in the different samples.

Section 4.3.1

Correlation of Dose and Induced Absorption

During experiments at HERMES III, the radiation dose varied from shot to shot (from as little as 8 krad (Si), and up to as much as 70 krad (Si) per shot). The dose also varied spatially due to a uniform drop-off in the beam intensity away from the center. As a result, each sample was exposed to a range of doses per shot. This made it possible to perform a correlation analysis to determine whether the transient induced absorption (or gain) bore significant statistical dependence on the dose. For the purposes of this analysis, p-correlation was used as a measure of dependence, as defined below in Equation 4.7:

$$\rho_{xy} = \frac{\text{cov}(x, y)}{\sigma_x \sigma_y} \quad (4.7)$$

In Equation 4.7, cov() represents covariance, and σ represents standard deviation. Covariance is further defined below in Equation 4.8:

$$\text{cov}(x, y) = \frac{1}{N} \sum_{i=1}^N [(x_i - \bar{x})(y_i - \bar{y})] \quad (4.8)$$

In Equation 8, \bar{x} (\bar{y}) denotes the mean of the set $\{x\}$ ($\{y\}$). N is the total number of points in the data set.

The p-correlation describes how close the relationship between the two variable sets is to a linear one. It can assume values from -1 to 1. A value of 1 indicates that there is an exact linear relationship between the two sets. Value of -1 indicates that the two sets

lie on lines with opposite slopes. A p-value of 0 indicates that there is no statistically meaningful relationship between the two sets.

P-correlation was calculated for several cases where doses were compared against various measures of induced absorption.

Section 4.3.1.1

Undoped YAG

Several shots were available for each tested undoped YAG sample, yielding sufficient data to perform a correlation of radiation dose versus several measures of induced absorption. These measures include evaluating the maximum value of the induced absorption at 1064 nm (denoted $Max \Delta\alpha$), the total sum of the data points in the curve (denoted $Sum \Delta\alpha$, trace being used was T2, time interval from 0 ms up to 24 ms), the sum of the fast signal (denoted $Sum \Delta\alpha$, in which data points were summed from 0 ms to 0.2 ms), or data points sum of the early portion of the slow signal (denoted $Sum \Delta\alpha$ (0.2ms – 1 ms)). Calculated p-correlation values are shown below in Table 4.4. The *combined* column lists the p-correlation for the set that included data from all the samples.

Table 4.4

	AL*	SM (avg)	SM (high)	<i>combined</i>
$Max \Delta\alpha$	-1.000	0.739	0.473	0.574
$Sum \Delta\alpha$	1.000	0.160	0.725	0.387
$Sum \Delta\alpha$ (0.2 ms)	1.000	0.542	0.932	0.537
$Sum \Delta\alpha$ (0.2ms – 1 ms)	1.000	0.413	0.210	0.448

*Only two shots were available for this sample. Therefore, p-correlation could only yield values of ± 1 .

Table 4.4. P-correlation values for undoped YAG, describing dependence of induced absorption on shot dose.

In most cases, the data appear to be weakly positively correlated with shot dose. The trend appears to be generally positive – an increase in total dose received is generally accompanied by an increase in the observed induced absorption.

One representation of the efficiency of inducing absorption with gamma irradiation is represented below in Figure 4.16. This figure shows a plot of $Sum \Delta\alpha$ (0.2

ms) vs. shot dose. Each sample is represented using a different symbol. Each individual shot is represented with a single data point.

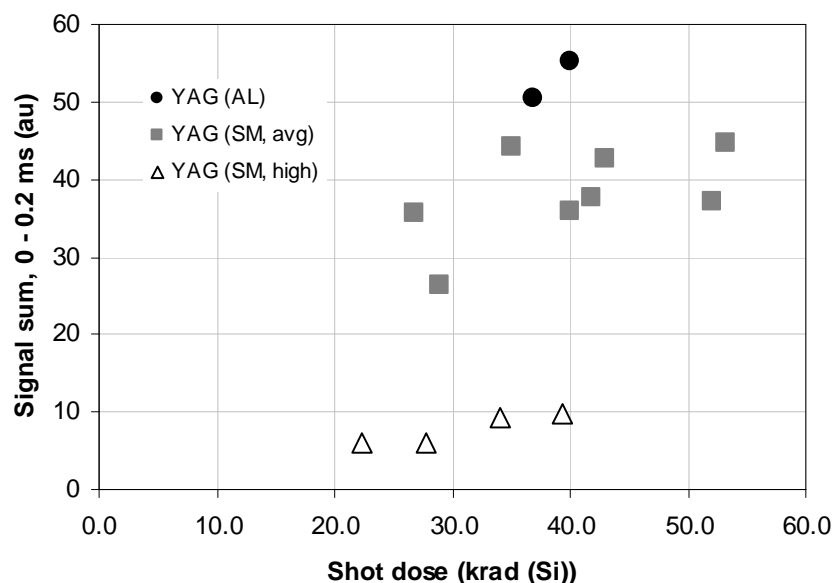


Figure 4.16. A plot of $\Delta\alpha$ (summed over the first 0.2 ms) vs. shot dose. Data points correspond to the three samples tested – Airtron-Litton (AL), Scientific Materials average purity (SM avg), Scientific Materials high purity (SM high). A general positive correlation between induced absorption and dose are noted.

The plot in Figure 4.16 illustrates the observation made in Table 4.4, that induced absorption is generally positively correlated with the irradiation dose. However, it should also be noted that there is significant variation in response from sample to sample. The three sets of points, when combined, only form an uncertain correlation.

It is also clear from the plot, that for a given dose, an increase in contamination (the Airtron-Litton sample being the most heavily contaminated of the three) corresponds to an increase in induced absorption. This is most clearly seen for the three points

corresponding to approximately 400 Gy (Si) dose. This agrees with the observation made in the earlier discussion of data (Section 4.2.1.1).

Section 4.3.1.2

Nd:YAG

The three compositions tested were analyzed separately. Correlation analysis was carried out using sums of data points from two time intervals. The first interval was designed to include only the “fast” component of the induced absorption. This interval was set from 0.0 ms to 0.03 ms. Its boundary was picked as approximately the point where the gradient of the curve changed significantly from the fast decay process to a slower one.

The second interval was set from 1.0 ms to 5.0 ms. The first boundary was chosen to minimize contributions from the gain component (described above, in Section 4.2.1.2). This component varied strongly from sample to sample, and so it was desired to exclude it from this analysis. The second boundary was chosen to minimize contributions from fluctuations in laser power and other signal noise. Results of correlation analysis over these intervals are presented below in Table 4.5.

Samples		Sum (0 – 0.03 ms)	Sum (1 – 5 ms)
0.5 at% Nd	S01	0.4	0.8
	S04*	1.0	1.0
	S14*	1.0	1.0
	All	0.0	0.8
1.0 at% Nd [†]		0.6	0.7
1.2 at% Nd	S01	0.6	0.0
	S02*	-1.0	-1.0
	S03*	1.0	-1.0
	S18*	1.0	1.0
	All	0.3	0.6

*Only two exposures were available for these samples.

[†]Only one sample of this composition was available.

Table 4.5. Correlation values between indicated sums over data points for given samples and corresponding shot doses.

Although none of the correlation scores are high some general conclusions can still be drawn from the trends seen in Table 4.5. That some samples have scores of unity (positive or negative) is not indicative of the strength of correlation, but rather due to the fact that only two shots were recorded for each of those samples. Given two points, the correlation equation can only produce values of unity (since any two non-coincidence points always form a line). Nonetheless, data from these samples are included here for completeness. Furthermore, data from these samples were still used when groups of samples were being analyzed (shown in Table 4.5, on lines marked “All”).

In all cases, correlation score for the interval corresponding to the “slow” process is higher than the score corresponding to the “fast” process. In fact, when all 0.5 at% Nd:YAG samples are considered as a single data set, overall p-correlation for the fast process between induced absorption and dose is zero, suggesting there is no meaningful relationship between dose and absorption over the range of experimental parameters.

While correlation values are consistently higher for the second interval, it can also be observed that correlation is reduced with increased concentration of neodymium.

Overall, there is generally a positive correlation between shot dose and observed amount of induced absorption. However, the present set of data is insufficient to suggest a particular functional dependence of induced absorption on shot dose.

Section 4.3.2

Modeling of Transient Response

In order to better interpret the transient response data and correlate it with results published by previous researchers, a mathematical model representation of the data was sought. Based on visual analysis of the different modes of behavior, it was possible to break down the ionizing-radiation response of the YAG-based samples into three general categories, mentioned previously in Section 4.2.1 of this Chapter. These categories include the fast absorption process (lifetime on the order of 10 μ s), the slow absorption process (lifetime on the order of 10 ms), and the gain process (lifetime on the order of 0.5 ms).

Further analysis of the data showed that even in the samples that experienced significant induced absorption, the fast process was not always present. Contributions to the data from the gain process also varied, becoming negligible in some samples. This allowed for isolation of the three processes, simplifying the overall data analysis.

Section 4.3.2.1

Undoped YAG

As described in the data section of this chapter, the transient response of undoped YAG samples generally followed two modes of behavior. One mode consisted of a slow absorption process with a delayed onset, and the other mode consisted of a fast and a slow absorption processes. The following analysis assumed that the two processes are physically distinct and independent. As such, a sample whose response consisted of only the slow process, had a response designated as $\Delta\alpha_{slow}$, and a sample with both the fast and slow response components had the following form:

$$\Delta\alpha = \Delta\alpha_{fast} + c \cdot \Delta\alpha_{slow} \quad (4.9)$$

In Equation 4.9, c is a proportionality constant. Since the Airtron-Litton undoped YAG sample was the only one to exhibit the exclusively slow-process mode of behavior, it was chosen as the reference slow process data set.

For the purposes of this modeling, c was defined in the following way:

$$c = \frac{\sum \Delta\alpha}{\sum \Delta\alpha_{slow}} \quad (4.10)$$

Summation was carried out over the time interval from 1 ms to 5 ms. After the slow process was thus accounted for in a given data set, the residual signal was fitted using a single exponential. Overall, the model for the undoped YAG samples took the following form:

$$\Delta\alpha(t) = a_{fast} \exp\left(-\frac{t}{\tau_{fast}}\right) + c \cdot \Delta\alpha_{slow}(t) \quad (4.11)$$

Fitting of the exponential term to the residual was accomplished using the *genfit* function in MathCAD, over a time interval up to 0.15 ms. The fits were stable and convergent, although they generally underestimated the values of induced absorption near $t = 0$, though usually by less than 5%. Variation in the amount of the underestimation caused some spread in the data. The results of the fits are presented below in Table 4.4. Results from multiple shots were averaged together.

Since the Airtron-Litton sample was used as the reference slow process data set, the fast process was not fitted to its data, and the value of c was, thus, unity by construction.

The fitted model and the original experimental data for the Scientific Materials average purity sample are shown below in Figure 4.17.

As can be seen in the two parts of Figure 4.17, the fit complies rather closely to the actual experimental data. Aside from the rapid oscillations of the curves (periodicity of approximately 0.2 ms), the model curve appears to follow closely the data curve. The model did not attempt to simulate these oscillations as they were attributed to instrumental noise. Therefore, the model is to be taken to accurately represent the data.

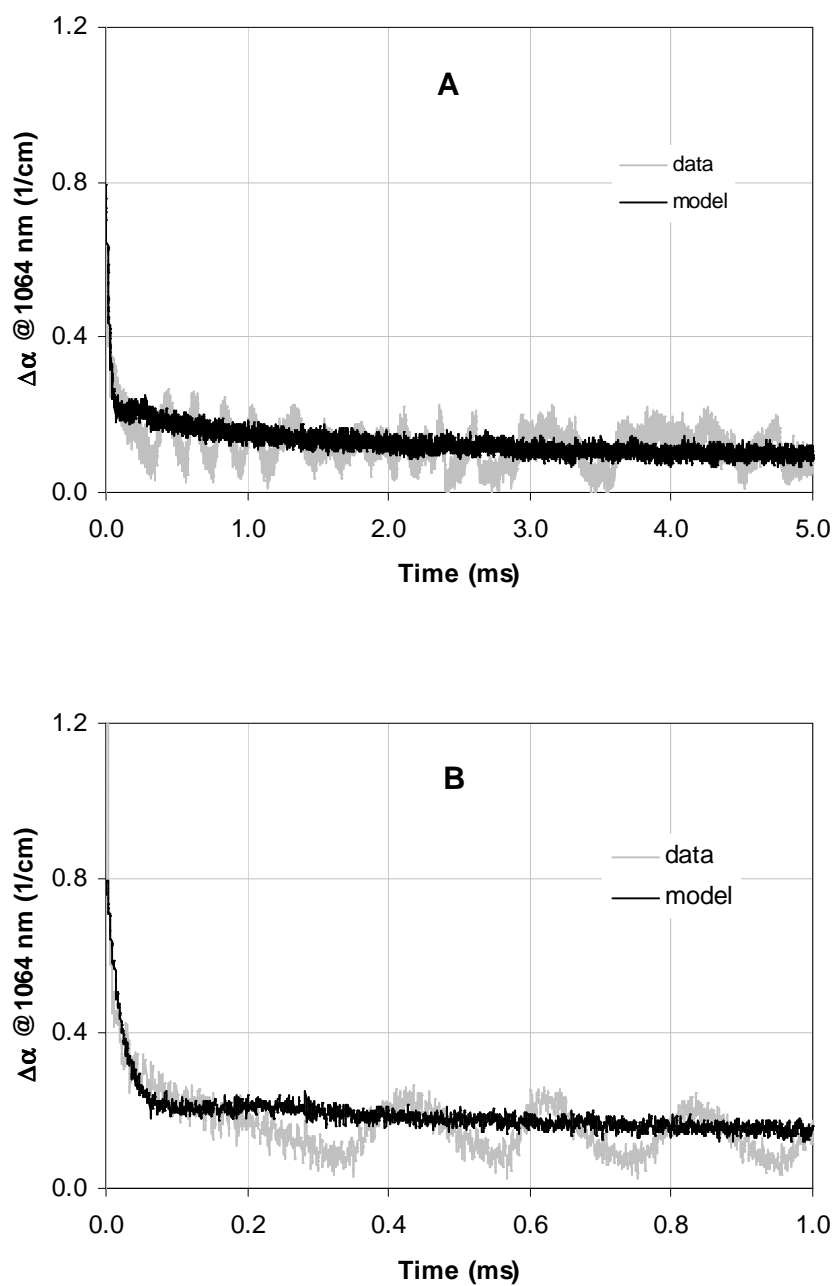


Figure 4.17. Experimental data from undoped YAG (SM, avg) and its model are compared on two different time scales. A: compliance with the slow process. B: compliance with the fast process.

Results of all the fits for the undoped YAG samples are represented below in Table 4.6. As can be seen in the obtained values of the fit parameters, amplitude of the slow process (represented by c) is much more dependent on the sample purity than the fast process parameters (most significantly the amplitude, a_{fast}).

Material	a_{fast} (cm^{-1})	τ_{fast} (ms)	c
YAG (AL)			1.000
YAG (SM, avg)	0.863	0.025	0.573
YAG (SM, high)	1.209	0.005	0.124

Table 4.6. Averaged results of modeling transient response of undoped YAG samples to pulses of gamma radiation. Material labels correspond to those used previously, as in Figure 4.3. Variable labels correspond to those used in Equation 4.11.

Overall, trends seen in Table 4.6 are generally aligned with the qualitative observations made previous in Section 4.2.1.1 of this Chapter.

Section 4.3.2.2

Nd:YAG

As outlined above, data analysis proceeded by attempting to isolate the processes in order to understand their general behavior. One 0.5 at% Nd:YAG and one 1.2 at% Nd:YAG sample exhibited response consisting of the slow component only. As the data from the 1.2 at% Nd:YAG sample appeared to be of higher quality (lower noise level), it was used as the reference set of data.

While the fast process was present in all of the other Nd:YAG samples analyzed, the gain contribution varied, becoming apparently negligible in some of the 1.2 at% Nd:YAG samples. These samples were used to isolate characteristics of the fast absorption process.

The apparent gain contribution was seen to be the strongest in 0.5 at% Nd:YAG samples. Figure 4.18 below represents the three types of signals identified. These representative data curves are the actual experimental data.

It is further clear from Figure 4.18 that the slow process contribution (when considered approximately past 1.0 ms) is similar in all three cases, differing only by some scaling factors. From here, the analysis proceeded in the following sequence.

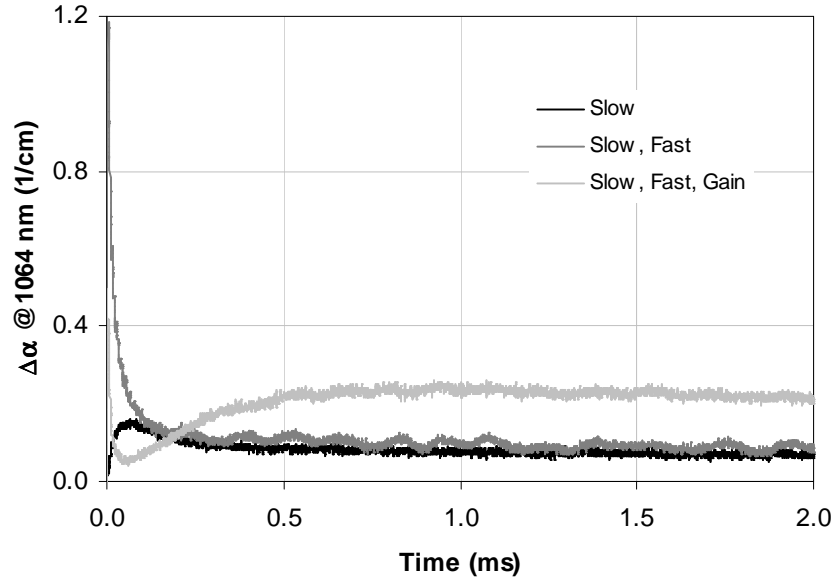


Figure 4.18. Examples of the three modes of behavior used in modeling of the transient response data. The black curve represents the slow absorption process. The dark gray curve exhibits both the slow and the fast processes. The light gray curve includes all three components – fast and slow absorption processes, as well as the gain process. These traces are actual experimental data. “Slow” and “Slow, Fast”: 1.2 at% Nd:YAG (UC) (two different samples). “Slow, Fast, Gain”: 0.5 at% Nd:YAG (UC).

Data from the 1.2 at% Nd:YAG sample that consisted solely of the slow component included data from two shots. These data were averaged together, producing one set of data describing the slow process. This set was labeled the reference slow process data set ($\Delta\alpha_{slow}$).

Then, two 1.2 at% Nd:YAG samples that appeared to not included a gain component were analyzed. For each set of data ($\Delta\alpha$), the reference slow process data was subtracted, after being adjusted by the scaling c :

$$c = \frac{\sum \Delta\alpha}{\sum \Delta\alpha_{slow}} \quad (4.12)$$

The summation in Equation 4.12 was carried out over the interval from 1 ms to 5 ms. The model (identical to that expressed in Equation 4.11) and the data are compared in Figure 4.19 below, in which close agreement is seen between the two.

The residual data (remained after the scaled slow component was subtracted from the experimental data) was sufficiently well described by a single exponential. The fit was achieved using MathCAD's *genfit* function using analytically derived partial derivatives. Exponent's amplitude (a_{fast}) and lifetime (τ_{fast}) were used as adjustable parameters. This concluded analysis of the data composed of slow and fast process contributions. The resulting model was identical that used for undoped YAG, shown in Equation 4.11.

A representative result of the fitting procedure is shown below in Figure 4.19. As with the modeling of undoped YAG data discussed in the previous chapter, a close agreement is seen between the model and the actual data. Both the fast and the slow parts of the absorption response are replicated in the model.

No predictable relationship could be established between the amplitude of the slow absorption process and fitting parameters of the fast absorption process. Additionally, it was seen that the fast process and the gain process overlapped significantly making the isolation of these effects impossible in relevant samples.

Modeling of the samples that included a significant gain contribution started in the same way as that described above, by subtracting the reference slow process data set, again adjusted by c , following Equation 4.12.

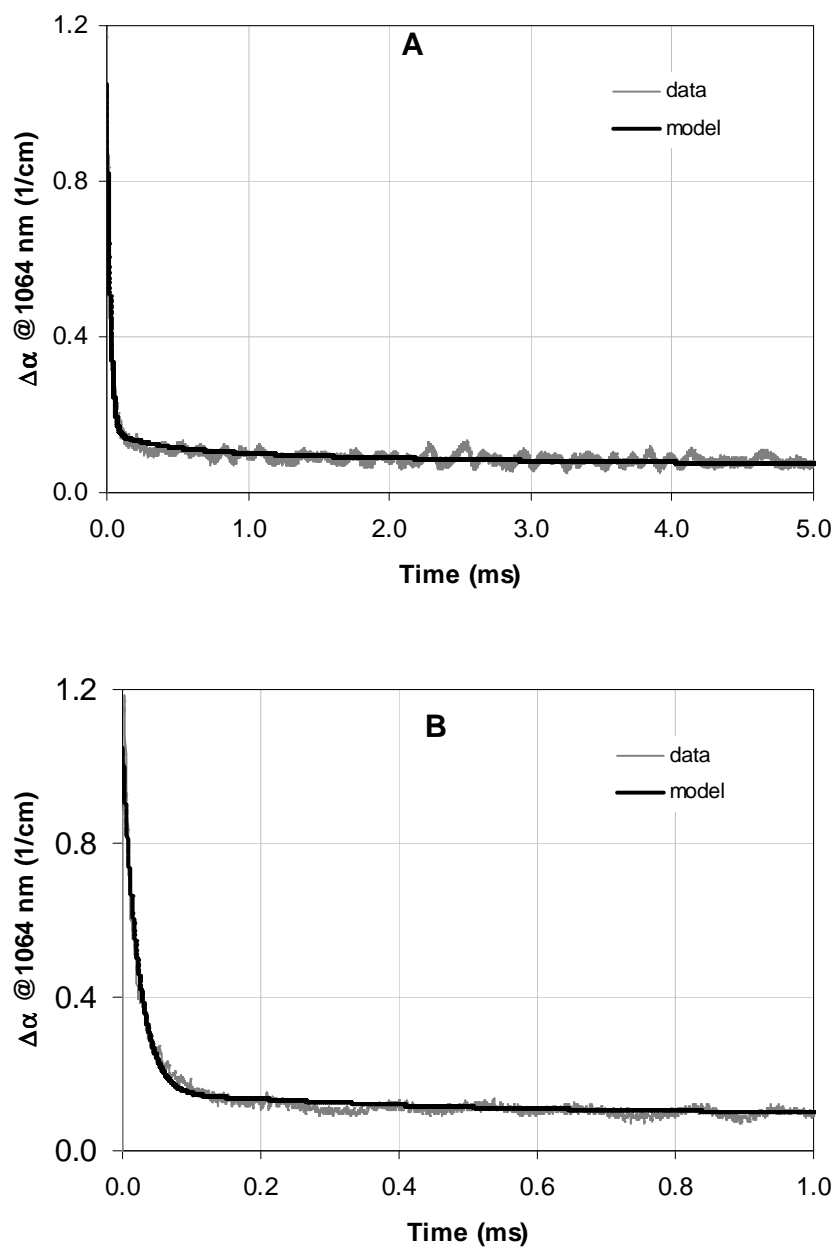


Figure 4.19. Experimental data and its model are compared on two different time scales. A: compliance with the slow process. B: compliance with the fast process. Fits are based on a 1.2 at% Nd:YAG (UC) sample.

The residual data were fitted using a sum of two exponentials, one with a negative amplitude representing the gain process. This produced stable, convergent fits that accurately represented all remaining Nd:YAG samples. This model is described below in Equation 4.13:

$$\Delta\alpha(t) = a_{fast} \exp\left(-\frac{t}{\tau_{fast}}\right) - a_{gain} \exp\left(-\frac{t}{\tau_{gain}}\right) + c \cdot \Delta\alpha_{slow}(t) \quad (4.13)$$

An example of the resulting fit is shown below in Figure 4.20, where again good agreement is seen between the experimental data and the mathematical fit.

Close compliance of the model to the experimental data provides some validity to the underlying assumption about the processes contributing to the overall dynamics of the induced absorption response of Nd:YAG to pulsed gamma radiation.

All of the Nd:YAG samples for which data were available were processed using the method outlined above. The results of these fits are summarized below in Table 4.5. Data from multiple shots were averaged where available.

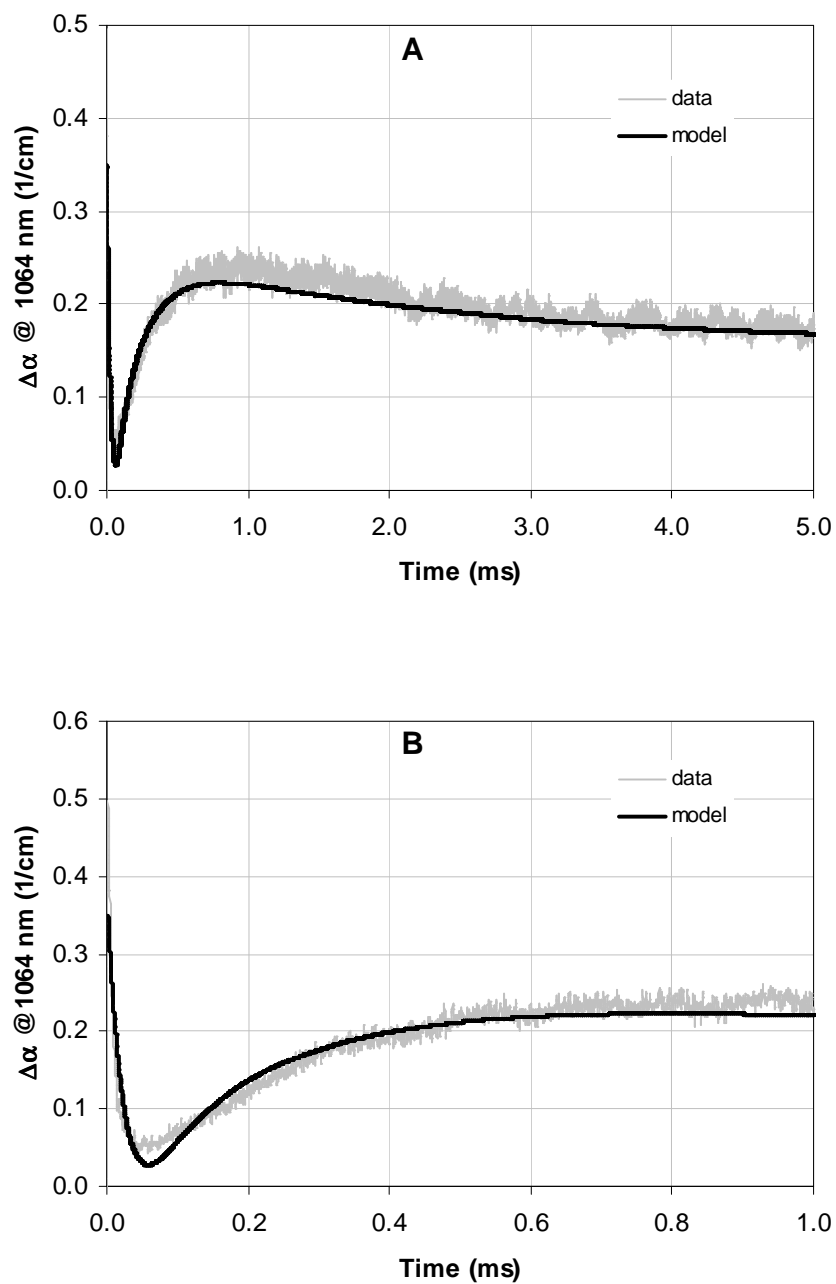


Figure 4.20. Experimental data and the model are compared on two different time scales. A: compliance with the slow process. B: compliance with the fast and the gain process. Fits are based on a 0.5 at% Nd:YAG (UC) sample.

Table 4.7

Sample		a_{fast} (cm^{-1})	τ_{fast} (ms)	a_{gain} (cm^{-1})	τ_{gain} (ms)	c
0.5 at% Nd (UC)	S01	0.801	0.024	0.423	0.218	2.494
	S04	0.882	0.028	0.227	0.163	2.507
	S14	0.906	0.022	0.087	0.272	2.361
1.0 at% Nd (SM)	S02	1.014	0.013	0.101	0.330	0.408
1.2 at% Nd (UC)	S01	0.759	0.030	 	 	1.001
	S02	 	 	 	 	1.000
	S04	0.763	0.024	0.119	0.308	1.122
	S18	1.163	0.023	 	 	1.108

Table 4.7. Average values of model fitting parameters describing transient response of Nd:YAG samples to pulsed gamma radiation. 1.2 at% Nd:YAG samples S01 and S18 had a negligible gain contribution, 1.2 at% Nd:YAG sample S02 was used as the slow process reference; none of the other components were fitted to its data.

Values in Table 4.7 reinforce visual observations made earlier in Section 4.2.1.2. The fast absorption process appears common to all samples, and seems fairly independent of neodymium concentration and sample purity (1.0 at% Nd:YAG (SM) samples had significantly lower levels of contamination than 0.5 at% Nd:YAG (UC) and 1.2 at% Nd:YAG (UC) samples. This independence suggests that the fast absorption process is linked more closely to the host crystal composition than to the Nd dopant or to the existence of impurities in the samples. Furthermore, the three processes identified – slow absorption, fast absorption, and gain – appear common and relatively constant amongst all samples, suggesting that, indeed, similar physical processes are taking place in all of the samples, albeit at differing amplitudes. It should be further noted, that the lifetime of the fast absorption process appears very similar between the Nd:YAG samples and the undoped YAG samples.

Section 4.3.2.3

High-Chromium Content Cr³⁺,Nd:YAG

Analysis of the transient response of the high-chromium co-doped samples proceeded in generally the same way as for the doped YAG samples described above – by identifying the longest-lifetime component first, subtracting, and then fitting the residual to an exponential process. Since all samples exhibited the same behavior (a combination of an apparent gain process and a small, nearly constant, absorbing contribution), it was not possible to immediately isolate one process from the others.

The first step in performing fits of the co-doped YAG data was to identify the value of the constant absorbing contribution over the time interval being analyzed (0 ms – 5 ms). This was achieved by simply averaging all data past 1 ms (to avoid contributions from the gain process). This value is represented by the variable b , defined below:

$$b = \overline{\Delta\alpha(t \in [1,5])} \quad (4.14)$$

The overall model then can be expressed in Equation 4.15 below:

$$\Delta\alpha(t) = a_{gain} \exp\left(-\frac{t}{\tau_{gain}}\right) + b \quad (4.15)$$

The residual signal was fitted using a single exponential representing the gain process, in a manner identical to its previous use in this Section. Use of a dual exponential was also attempted (in order to account for some initial absorption). However, dual exponentials produced unstable fits that either did not converge, or produced trivial results that did not improve upon the single exponential method.

Results, averaged for each sample, are presented in Table 4.8 below.

Table 4.8

Sample		a_{gain} (cm ⁻¹)	τ_{gain} (ms)	b (cm ⁻¹)
0.5 at% Cr, 1.0 at% Nd	S02	0.031	0.336	0.0019
	S06	0.154	0.258	0.0053
1.0 at% Cr, 1.2 at% Nd	S07	0.062	0.323	0.0098
	S08	0.089	0.315	0.0042

Table 4.8. Average values of model fitting parameters describing transient response of high-chromium Cr, Nd:YAG samples to pulsed gamma radiation.

Examination of the data reveal that the parameters of the gain component of the signal data from the co-doped Cr³⁺:Nd:YAG appear comparable to those of singly-doped Nd:YAG samples with higher neodymium concentrations, suggesting that the same gain process is active in both types of compositions.

Section 4.3.2.4

Low Chromium Content Cr³⁺,Nd:YAG

Analysis of the data from the low chromium content samples proceeded in a way similar to the data from the high chromium content samples, outlined above in Section 4.3.2.3. Since it was not possible to use an actual data set to isolate any of the contributing processes, isolation was carried out numerically, by fitting separately processes taking place on longer and shorter time scales.

The first part to be isolated was the longer processes, considered on the time interval from 0.1 ms to 5 ms. Given the shape of the curve – a delayed onset with gradual decline – the data were modeled using two exponentials, one with a positive amplitude and one with a negative amplitude. This follows the set of processes identified in Nd:YAG samples – a slow absorption process and a gain process. The resulting model for this time window took the following form:

$$\Delta\alpha(t > 0.1\text{ms}) = a_{\text{slow}} \exp\left(-\frac{t}{\tau_{\text{slow}}}\right) - a_{\text{gain}} \exp\left(-\frac{t}{\tau_{\text{gain}}}\right) \quad (4.16)$$

A data set simulated using Equation 4.16 was then generated for the entire time interval (0 ms to 5 ms), projecting the influence of these slower processes toward $t = 0$. This simulated data set was subtracted from the original data, and the resulting residual was further analyzed.

The residual was considered on a small time interval, from 0 ms to 0.15 ms. Data in this interval consisted of a rapidly decaying contribution with, in some cases, a

constant offset, perhaps resulting from an imperfect fit of the model in Equation 4.16.

The residual was modeled using the Equation 4.17 below.

$$\Delta\alpha(t < 0.15 \text{ ms}) = a_{fast} \exp\left(-\frac{t}{\tau_{fast}}\right) + d \quad (4.17)$$

In Equation 4.17, the constant d accounts for the offset described above.

Table 4.9, shown below, provides averaged results of these fits. The parameter d is omitted from the table, since it was used as a correction factor over a specific interval, and likely does not correspond to actual physical processes.

Table 4.9

	a_{fast} (cm ⁻¹)	τ_{fast} (ms)	a_{slow} (cm ⁻¹)	τ_{slow} (ms)	a_{gain} (cm ⁻¹)	τ_{gain} (ms)
S02	1.057	0.0028	0.189	10.47	0.246	0.211
S03	0.688	0.0028	0.146	11.24	0.208	0.224

Table 4.9. Average values of model fitting parameters describing transient response of low-chromium Cr, Nd:YAG (AL) samples to pulsed gamma radiation.

As seen in Table 4.9, lifetimes and amplitudes of all three processes are fairly similar, pointing at consistency in the material's behavior and the test's results. Lifetimes of the gain process are again similar to those observed in the other materials where the gain process was present, though the gain parameter values are seen to be somewhat closer to those of materials with 0.5 at% Nd rather than materials with 1.0 or 1.2 at% Nd, as might have been expected.

Section 4.3.3

Summary of Numerical Data Analysis

Numerical analysis has been carried out on the transient absorption data from HERMES III on all the samples in the experimental sample suite. Analysis was confined to the first 5 ms of the signal, due to oscillations in laser power limiting the certainty of data at longer time scales.

The first part of analysis consisted of testing p-correlation between various portions of the data and incident radiation dose. While correlation scores were generally positive, they were not high enough to suggest a linear relationship between induced absorption and incident dose with confidence. It can only be generally claimed that an increase in dose tended to increase induced absorption. Exact functional relationship between the two quantities could not be established.

The second part of analysis consisted of identifying common processes composing the transient response across the sample suite. Generally, there were three processes that could be isolated. The first was a fast absorption process. It was fitted using a single exponential, with lifetimes generally on the order of 25 μ s.

The second process was a gain process, observed in samples containing neodymium. It was also modeled using a single exponential. Its lifetime varied from about 200 μ s to 300 μ s, with samples containing a higher concentration of neodymium reporting longer lifetimes.

The third process was a slow absorption process. In low-chromium co-doped samples it was modeled using a single exponential, with fits returning a lifetime near 10

ms. For undoped YAG and Nd:YAG samples, the slow absorption process was not directly modeled, but rather a reference data set from one of the samples was used. It was found that the reference sample's response was sufficiently well replicated in all other samples in this group.

A summary of the fitting results is included below in Table 4.10. Constant offsets (such as b used for the high-chromium co-doped samples in Equation 4.15 and d for the low-chromium samples in Equation 4.17) are omitted in Table 4.10.

Composition		a_{fast} (cm^{-1})	τ_{fast} (ms)	a_{gain} (cm^{-1})	τ_{gain} (ms)	c	
YAG (AL)						1.000	
YAG (SM, avg)		0.863	0.025			0.573	
YAG (SM, high)		1.209	0.005			0.124	
0.5 at% Nd:YAG (UC)	S01	0.801	0.024	0.423	0.218	2.494	
	S04	0.882	0.028	0.227	0.163	2.507	
	S14	0.906	0.022	0.087	0.272	2.361	
1.0 at% Nd:YAG (SM)		S02	1.014	0.013	0.101	0.330	0.408
1.2 at% Nd:YAG (UC)	S01	0.759	0.030			1.001	
	S04	0.763	0.024	0.119	0.308	1.122	
	S18	1.163	0.023			1.108	
0.13 at% Cr, 1.0 at% Nd:YAG (AL)	S02	1.057	0.0028	0.246	0.211		
	S03	0.688	0.0028	0.208	0.224		
0.5 at% Cr, 1.0 at% Nd:YAG (SM)		S02			0.031	0.336	
1.0 at% Cr, 1.2 at% Nd:YAG (SM)	S06			0.154	0.258		
	S07			0.062	0.323		
	S08			0.089	0.315		

Table 4.10. Summary of fitting results from modeling of the transient response of materials tested at HERMES III. Crossed-out cells corresponded to values not used to fit the particular composition. The sample used as a reference data set in the modeling of the Nd:YAG data was omitted from this table.

The data presented in Table 4.10 allows further analysis of the absorption processes in context of the contamination levels (refer to Table 3.5 for a summary of identified contaminants and their concentrations).

First, let us consider the slow absorption process represented by the fitting parameter c . In all cases, the value of c increases with increased contaminant levels. Since all contaminants generally increase in concentration together, it is difficult to identify which one is responsible for the growth of the slow absorption process' amplitude but the trend is clearly established.

In contrast, the amplitude of the fast absorption process (a_{fast} in Table 4.10) does not appear well-correlated with purity. In all cases, the amplitude of the fast absorption process is either approximately the same (Nd:YAG (SM) vs. Nd:YAG (UC)) or higher (YAG (SM, avg) vs. YAG (SM, high)) for the samples of greater purity.

This suggests that the fast absorption process is due to defects that are intrinsic to the YAG lattice itself. However, the slow absorption process is due to defects formed by impurities. Furthermore, it appears that the defects responsible for the slow absorption process are capable of quenching the defects responsible for the fast absorption process – in all cases, the samples that exclusively display the slow absorption process are among the most contaminated for that group.

Section 4.4

Discussion

Section 4.4.1

Identification of the Radiation-Hardened Composition

Out of the sample suite, those containing at least 0.5 at% Cr were seen to be almost entirely resistant to pulsed gamma irradiation. Modes of failure observed in all other samples either did not appear in these samples at all, or became greatly reduced.

In the domain of the immediate transient response, material behavior essentially consisted of three general processes. Two absorption processes (a “fast” and a “slow” process) and one gain process. While parameters of the gain process were found to be similar between all compositions containing neodymium, the co-doped high-chromium samples exhibited a nearly complete lack of the fast absorption process, and the slow process was similarly reduced. Therefore, the presence of chromium, in sufficient concentration, was effectively seen to block processes responsible for transient absorption that was unstable at room temperature.

In the domain of the permanent ionizing-radiation response, undoped YAG and Nd:YAG samples generally developed reduced UV absorption (a peak centered near 255 nm) and increased absorption across the visible and NIR parts of the optical spectrum. The decay and growth of permanent absorption bands in the samples can be correlated with the presence of Fe^{3+} (~250 nm) and Fe^{2+} (broad absorption ~350 nm to near IR) bands identified in the literature. This process will be discussed fully in section 4.4.2.2 below. In the high-chromium samples, neither of these changes were present after

irradiation regardless of gamma radiation dose. While the low-chromium co-doped sample did exhibit some induced permanent absorption, its profile differed from the non-chromium samples, indicating a different physical process in this sample set.

Based on these observations, it is clear that addition of at least 0.5 at% Cr to YAG material system vastly improves the laser material's resistance to gamma radiation. Experimental results show that the co-doped Cr,Nd:YAG materials can, indeed, function as radiation-hardened substitute of Nd:YAG.

Section 4.4.2

Physical Interpretation of Observations

This section aims to establish a connection between the observations described in above section and known processes taking place in YAG and Nd:YAG materials. Such identification relies on connecting results presented in this report to the established body of knowledge on the subject. Knowing the exact physical processes that are at play in these materials also helps in identifying the possible mechanisms by which the presence of chromium improves the co-doped materials' performance in an ionizing radiation environment.

Section 4.4.2.1

Identification of F-type Centers

Although no previous work in the known literature has performed identical experiments, it is nonetheless possible to draw parallels between observations made in this report and those made in previously published research. Previous work by other researchers does not report on kinetic changes in absorption at room temperature, as described in this report, however a number of researchers have reported on thermoluminescence studies of samples exposed to ionizing radiation (x-rays and UV) at cryogenic temperatures (Bernhardt 1976, Vedda et al. 2004).

Clearly, any color centers that are stable at cryogenic temperatures but have annealing temperatures below the room temperature become unstable at room temperatures. Such centers, if they manifested at room temperature at all will have relatively short lifetimes. While the connection between the kinetic data presented here and the thermoluminescence data published elsewhere is tenuous, an examination of this connection is nonetheless warranted.

Figures 4.21 and 4.22 below represent some of the data obtained by the previous researchers (Bernhardt 1976, Vedda et al. 2004). In the temperature range above 100 K, the two sets of data display two modes of behavior. The first, represented by the solid curve in Figure 4.21, consists of a peak near 140 K, and a pair of peaks near 186 K and 220 K. The second mode of behavior, represented by the dashed curve in Figure 4.21 and undoped YAG data in Figure 4.22, replicates the higher-temperature peaks while the peak near 140 K is absent.

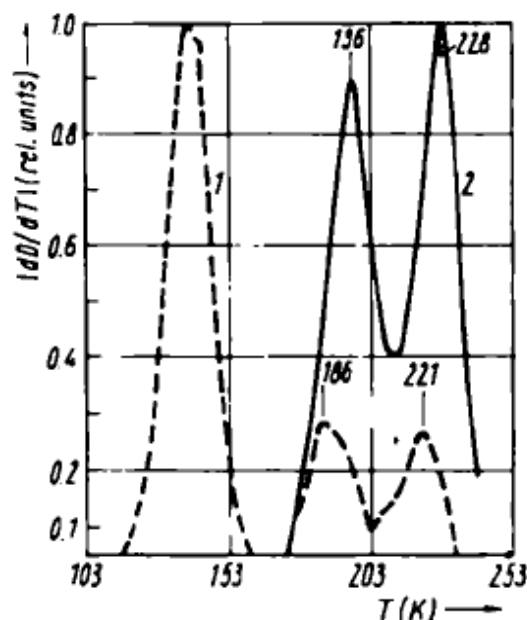


Figure 4.21. Thermoluminescence of nominally pure undoped YAG exposed to x-rays at liquid nitrogen temperature. Dashed and solid lines represent results of different experiments. Observation carried out at two wavelengths (644 nm and 775 nm). (Reproduced from Bernhardt 1976)

Indications of these observations are two-fold. The first is that unstable traps of varying depths are present in YAG. In particular, there are two groups of such traps that we can consider – one with an annealing temperature near 140 K (the shallower traps), and one with annealing temperature in the range from 180 K to 220 K (the deeper traps). The second indication is that one of these groups of traps may be inactive, leaving solely the deeper unstable trap. Though the thermoluminescence data does not suggest a reason for why one of the traps may or may not be active in a given sample, presently it suffices to note that the shallower of the two traps may be found to be inactive in some samples.

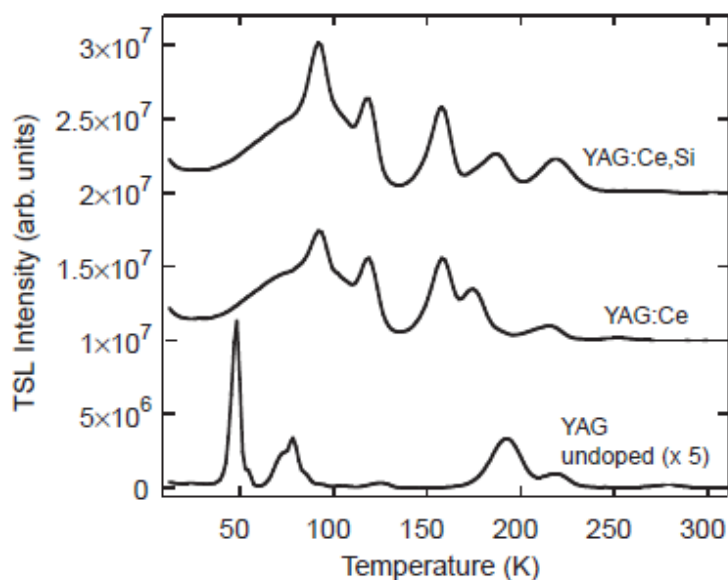


Figure 4.22. Thermoluminescence of several materials exposed to x-rays at 10 K. Curves are artificially vertically offset. Curves obtained by integrating wavelength-resolved measurements from 280 nm to 715 nm. (Reproduced from Vedda et al. 2004)

These two points bear some similarity to observations made in this chapter – that the dynamic response of undoped YAG to pulsed gamma radiation consists of two groups of processes, of apparently two different potential depths, and that the shallower one (corresponding to the faster decay lifetime) may be inactive. While the correspondence of these trends is notable, it is not a rigorous cause for physical equivalence of the processes observed.

Unstable traps in YAG are generally attributed to electrons stripped from oxygen ions and trapped on oxygen vacancies or self-trapped interstitially (Bernhardt 1976, Mori 1977, Karaseva et al. 1985, Akhmadulin et al. 1992, Matkovski et al. 2000). The trend similarity outlined above suggests that observations made in this report are likely consistent with observations made by other researchers. Therefore, though with a

reservation, we may use other researchers' physical interpretations – specifically, that unstable color centers are effectively the result of F center activity – to provide a hypothetical description of the materials used in this report.

Section 4.4.2.2

Identification of Fe^{3+} / Fe^{2+} Conversion

As described in Sections 4.2.2.1 and 4.2.2.2 of this Chapter, undoped YAG and Nd:YAG samples exhibited a nearly identical pattern of permanent optical absorption behavior. The change in the absorption profile consisted of a negative peak located near 250 nm, indicating a decrease in optical absorption with ionizing radiation exposure of the materials, and a positive peak located near 310 nm, indicating a radiation-induced increase in optical loss in the samples, that extended across the visible and into the NIR parts of the optical spectrum.

This pattern of behavior has been previously observed by other researchers, such as K. Mori (1977) and Akhmadulin et al. (1992). Differential absorption data observed by these authors are shown below in Figures 4.23 and 4.24.

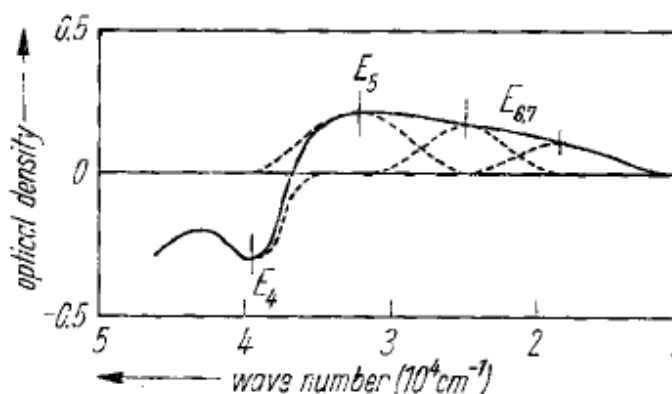


Figure 4.23. Differential absorption for an undoped YAG sample irradiated with an unfiltered xenon flash lamp. Solid line indicates the spectrum. Dashed lines represent modeled components. (Reproduced from K. Mori 1977).

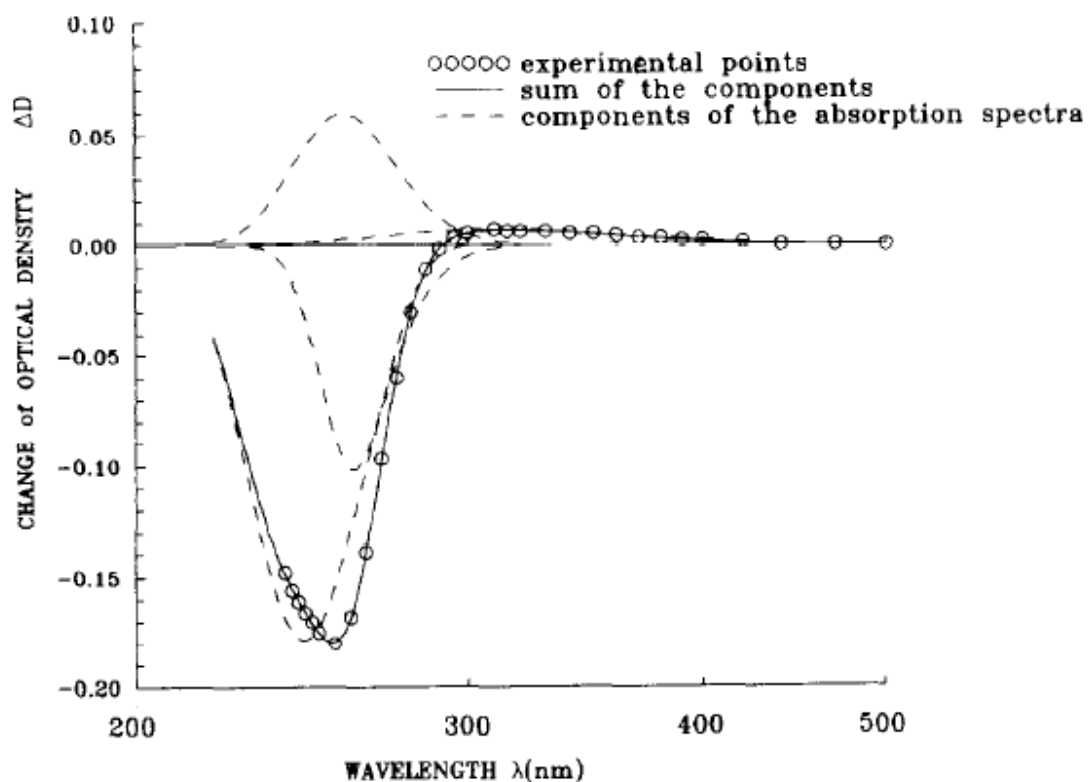
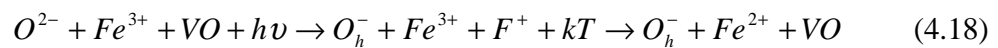


Figure 4.24. Differential absorption for an undoped YAG sample. Changes induced by a reducing anneal. (Reproduced from Akhmadulin et al. 1992).

Both authors attribute the changes to a change in the valence state of the iron impurity. The peak near 250 nm is attributed to the trivalent iron impurity (Fe^{3+}), while the broad peak near 310 nm is attributed to iron in the divalent state (Fe^{2+}). Their differential absorption observations closely agree with observations presented in this report (up to a negligible scaling factor). Therefore, we will cautiously make the assignment that the absorption spectrum changes observed in the present report are attributable to similar sources. The present data, thus, support a model in which in undoped YAG and Nd:YAG samples, pulsed gamma radiation induces a reduction of the trivalent iron impurity to its divalent state.

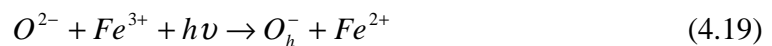
While the two authors cited above agreed on the attribution of the changes in the optical absorption, they disagree on the physical pathway that lead to the creation of the iron color center.

Mori (1977) stressed the role of oxygen vacancies as intermediate electron traps. In the model he presented, anions (oxygen ions for the case of YAG) become photoionized (creating O_h^- hole centers). These electrons first become trapped at oxygen vacancies (yielding F and F^+ electron color centers) as well as at impurities (such as the Fe^{2+} electron color center). As the F and F^+ center begin to relax (since they are unstable at room temperature), electrons may recombine with the hole centers, or become trapped on the impurity centers (increasing the concentration of the Fe^{2+} color centers). This process can be summarized in Equation 4.18 below.



In the equation above, VO represents an oxygen vacancy, $h\nu$ represents a photon, and kT represents the thermal energy that destabilizes the F^+ color center.

Akhmadulin et al. (1992), however, posited that production of the Fe^{2+} color centers was purely through a ligand transfer from a coordinating oxygen ion. Their model is represented in the following photochemical equation shown below.



The important difference between the two models is the inclusion of the bridging role of the oxygen vacancy which does or does not act as the intermediary between the oxygen ion and the iron electron trap.

In a later paper, Akhmadulin et al. (1993) further explored the Fe^{2+} color center, in particular studying the EPR spectra of the divalent ion in order to determine its position in the crystal lattice. By comparing their observations to predictions of the ion's behavior in the two possible sites (octahedral and tetrahedral), they claimed that the divalent iron impurity occupies the octahedral site.

The importance of the last observation is that if the iron impurity were to be induced to occupy only the tetrahedral sites – whether by means of material composition, treatment, or growth conditions – its ability to form color centers would be significantly reduced.

Section 4.5

Conclusions

In the preceding chapter, it has been observed that the response of undoped YAG and Nd:YAG samples to gamma radiation follows a similar process. The immediate transient response at 1064 nm has been seen to consist of a slow and a fast absorption process, the former with lifetimes generally close to 20 μ s, and the latter with lifetimes generally on the order of 10 ms. Nd:YAG samples also sometimes were observed to exhibit a pumped gain response, with the lifetimes ranging from 200 μ s to 350 μ s. Absorption processes that may be attributable to F and F^+ color-center activity (both of which are unstable at room temperature) have been tentatively identified. The gain process was clearly seen to be due to the presence of neodymium ions in the YAG lattice.

The permanent, steady-state, response of these materials to ionizing-radiation exposure consisted of a reduced absorption near 250 nm, while absorption above 300 nm and toward the NIR increased. These changes are consistent with a recharging of the iron impurity, changing its state from trivalent to divalent.

Experiments performed with samples of Cr^{3+} :YAG did not experience any observable radiation-induced changes in optical transmittance. Cr,Nd:YAG samples, on the other hand, were split into two groups based on their behavior. Those containing 0.13 at% Cr exhibited a small amount of slowly decaying transient absorption at 1064 nm as well permanent absorption. Permanent, radiation-induced changes in the optical absorption spectrum consisted of an increase in the UV absorption and the induction of a

broad peak centered near 480 nm. These changes have not been attributed to any specific processes at this point of the report.

Cr,Nd:YAG samples containing at least 0.5 at% Cr produced a clear gain response (with lifetimes comparable to those observed in some Nd:YAG samples). Although a small amount of transient absorption was detected, no meaningful permanent changes in the optical absorption spectrum were noted.

Based on these findings, the original hypothesis of the report – that a co-doped Cr,Nd:YAG material can serve as a radiation-hardened material – is supported, though with a qualification, which is that the concentration of chromium in the sample must exceed a certain minimal threshold. Although this threshold is not currently precisely established, it should be noted that samples with at least 0.5 at% Cr did not experience significant degradation of optical transmission due to pulsed gamma irradiation.

Chapter 5 – Results of UV Irradiation Tests

Chapter Summary

Samples representing the experimental sample suite were exposed to pulsed UV laser radiation. Tests consisted of an experimental setup similar to that used at HERMES III – measuring in-situ transmission at 1064 nm in response to individual pulses of UV radiation. Differential optical absorption spectroscopy observations were also carried out to identify steady-state changes in the materials. Overall, the experimental strategy was to closely follow tests performed using gamma radiation to obtain a close comparison of the two ionizing radiation environments.

Part of the motivation for performing the UV experiments was to identify a material testing technique that would closely resemble the results obtained in tests at HERMES III. Access to such a technique would have multiple advantages. Testing materials using pulsed UV radiation – as opposed to pulsed gamma radiation – carries lower cost and fewer hazards. Such a technique would also be more easily accessible and controlled, since it would be implemented in our own laboratory using our own equipment. Tests involving UV radiation instead of gamma radiation would also carry a considerably lower cost, reducing the overall resource commitment necessary to develop radiation-hard materials.

Interpretation of data obtained through the UV experiments was carried out mostly by comparing it to data obtained through the HERMES III experiments. These comparisons are covered in Section 5.4.2 and 5.4.3.

Observations of Cr^{3+} :YAG revealed processes not mirrored by the data available from the HERMES III experiments. Analysis of these new processes is covered in Section 5.4.1.1. These new data also provided an insight into a further analysis of the Cr^{3+} :YAG data from HERMES III, which is covered in Section 5.3.2.

Section 5.1

Method

Section 5.1.1

Experimental Setup of the UV/NIR Pump/Probe Test

These tests measured the time-resolved evolution of sample transmission at 1064 nm in response to fast pulses of UV laser radiation. The source of irradiation was a KrF excimer laser (operating wavelength 248 nm), which produced 10 ns pulses with energies ranging from 5 mJ to 15 mJ per pulse (the setup is described in detail below in Section 5.1.1.1). The UV/NIR Pump/Probe (UNPP) tests facilitated the examination of color-center formation in the materials included in the experimental sample suite (described previously in Chapter III) under the influence of UV irradiation.

The UNPP setup was designed and custom-built in our own laboratory at the University of Arizona, affording a greater degree of control over the experimental conditions. This Section will discuss the physical layout of the setup, how the data was acquired and processed, and the degree of the experiment's reliability and accuracy. In the following sections, results of the measurements regarding effects of UV irradiation on doped and undoped YAG will be presented. This will be followed by a discussion comparing effects of UV irradiation to the effects of gamma irradiation.

Section 5.1.1.1

Physical Setup

This experiment consisted of in-situ measurements of samples' transmission at 1064 nm as they were exposed to individual pulses of UV laser radiation. UV pulses were provided by a KrF excimer laser operating at 248 nm. The experiment used a single-pass, dual-detector setup, employing referencing and rest-signal nulling. The exact experimental configuration is shown in Figure 5.1 below.

The UV pump beam was steered using two narrowband dielectric reflectors (marked 2 in Figure 5.1), with reflectivity maxima at 248 nm. The UV laser delivered short pulses (nominal duration 10 ns) with energies in the range from 5 mJ to 15 mJ. The UV beam was projected at a small angle onto the sample using a 150 mm focal length UV-grade fused silica plano-convex lens. The exposure spot on the sample was approximately 6 mm x 6 mm. After passing through the sample, the UV beam terminated in a beam block. Scattered UV light was registered by the Pulse detector (ThorLabs FDS-010 photodiode, nominal bandwidth 1 GHz, biasing voltage +24 V, loading resistor 50 Ω).

The system delivered at-sample single shot pulses with energy densities in the range from 13.8 mJ / cm² to 41.6 mJ / cm². Taking into account the nominal pulse duration, this translates into at-sample single shot power densities ranging from 1.4 MW / cm² to 4.2 MW / cm².

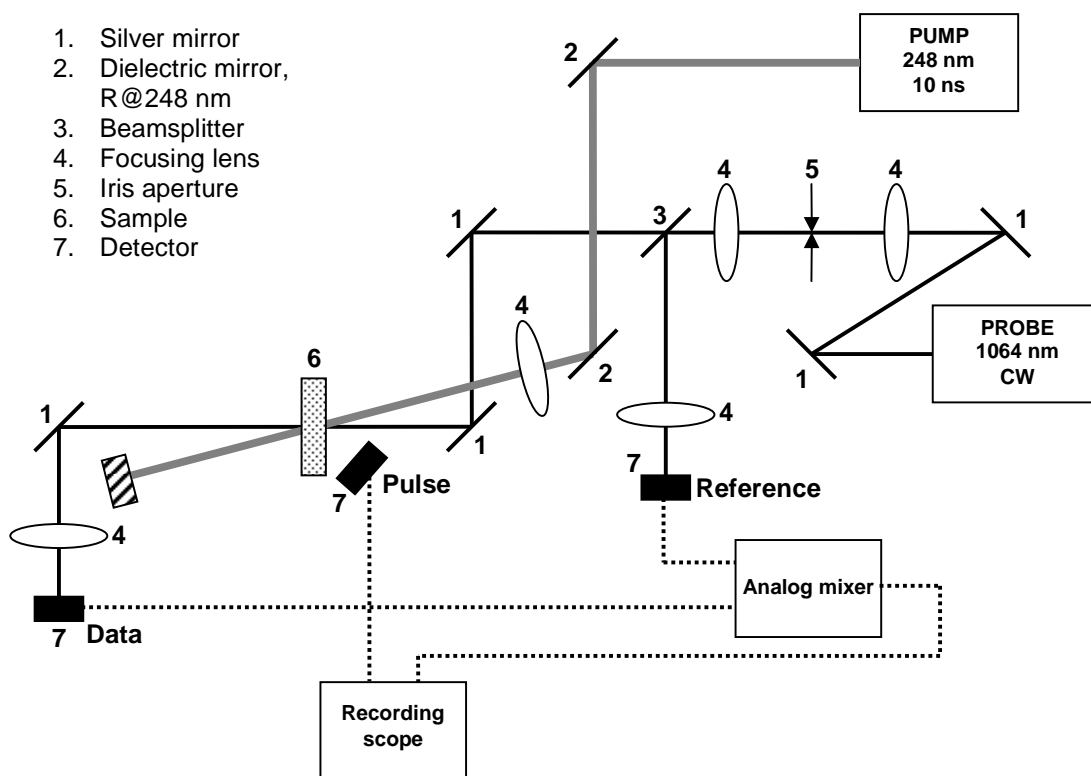


Figure 5.1. Physical layout of the UV/NIR Pump/Probe experiment.

The Near-Infrared (NIR) probe beam (normally operated at its minimum power of approximately 65 mW, operating wavelength of 1064 nm) was steered using silver mirrors (labeled 1 in Figure 5.1). The first pair of mirrors brought the beam to the same height as the excimer beam, so that the rest of path manipulation could be performed in a single horizontal plane. The probe beam's profile quality was improved using a 1:1 afocal telescope comprised of two lenses (labeled 4 in Figure 5.1, uncoated BK7 plano-convex lenses with nominal focal lengths of +100 mm) and an iris aperture (labeled 5) placed in the intermediate focal plane. This significantly improved spot quality (the laser produced a double-spot, a defect that was eliminated by this setup).

The probe beam was then sampled using a nominally 50 / 50 beam splitter, dividing the probe beam into a reference beam and a data beam. The former was directed toward the reference detector, while the latter was steered toward the sample using another pair of silver mirrors. The probe beam impinged on the sample at normal incidence. After passing through the sample, the probe beam was steered toward the Data detector using another silver mirror.

Both the data and the reference beams were focused into the detectors (with uncoated BK7 plano-convex lenses, nominal focal length of +100 mm), underfilling the detector surfaces.

Data and Reference detectors (ThorLabs FDS-100 photodiodes, nominal bandwidth 100 MHz, biasing voltage +24 V, loading resistor 1 k Ω) were further outfitted with shrouds protecting them from stray light. These shrouds were made of heavy weight black paper, measuring 2" in length with a 0.5" x 0.5" square cross-section (allowing for a f/4 collection of light, matched to the focusing lenses).

The outputs of the Data and Reference detectors were then fed to an analog mixer, which subtracted the two signals from one other (its operation is described below in Figures 5.2 and 5.3). The mixer's output was then sent to the recording oscilloscope (Fluke model 400C, nominal bandwidth 400 MHz), where it was stored.

The output of the Pulse detector was sent directly to the recording oscilloscope. It was used to provide timing information, serving as the trigger for the oscilloscope. The Pulse detector's output was not stored.

The analog mixer was a custom-built circuit. Its function is illustrated by Equation 5.1 below. Its output (V_{out}) was the difference of the signal from the Data detector (V_{data}) and the signal from the Reference detector (V_{ref}). The Reference detector's signal was adjustable by variable gain a .

$$V_{out} = V_{data} - a \cdot V_{ref} \quad (5.1)$$

Therefore, the Data signal was passed through with unity gain. Variable negative gain was applied to the Reference signal. The circuit's layout is shown below in Figures 5.2 and 5.3

Raw signals from the detectors were delivered to this mixer circuit via BNC cables, connected at the ports indicated on the left-hand side of the diagram in Figure 5.2. Each signal was first put through an isolating buffer (implement using an op-amp follower), using op-amps labeled U1A and U3A. The isolating buffers were built using LF 412 dual op-amps (manufactured by National Semiconductor Co., nominal bandwidth 3 MHz, supply voltage ± 15 V).

The reference signal was then processed by an inverting amplifier (U3B in Figure 5.2) with variable gain. The exact gain was set by two variable resistors R6 (coarse adjustment) and R7 (fine adjustment). After inversion, the signal was once again buffered by another follower (labeled U4, National Semiconductor LM 741 single op-amp, nominal bandwidth 250 kHz, supply voltage ± 15 V).

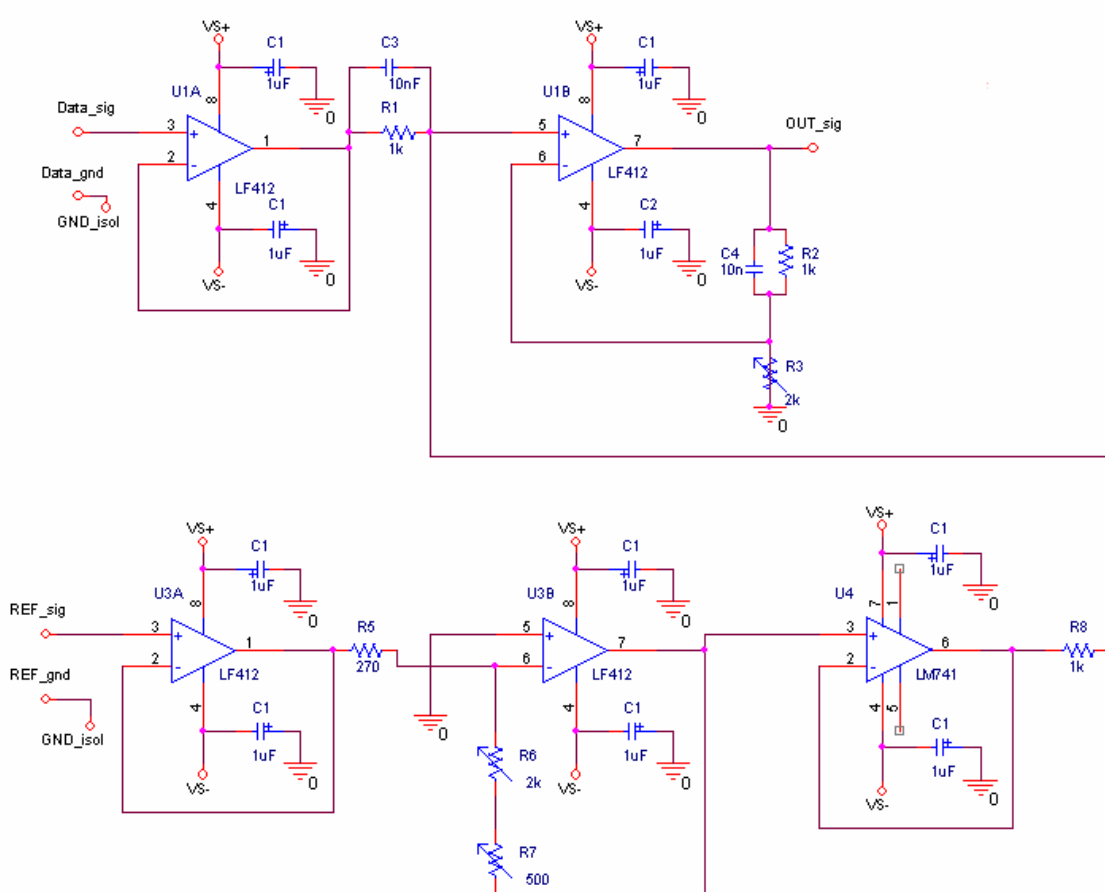


Figure 5.2. Main circuit diagram of the analog mixer used in the UNPP experiment. GND_isol connects to an isolated ground reference, shown in Figure 5.3.

At this point, the data signal and reference signal (amplified and inverted) were passed to the adder circuit element (labeled U1B in Figure 5.2, again built using an LF 412 op-amp). This element simply added signals arriving at its positive terminal, providing overall unity gain (ensured by the variable resistor R3). The output of the adder element was connected to another BNC cable that delivered it to the recording oscilloscope.

Power supplies at each individual op-amp were equipped with bypass 1 μF capacitors to ensure their operating stability. Forward bypass ceramic capacitors C3 and C4 were used to improve the circuit's high-frequency response.

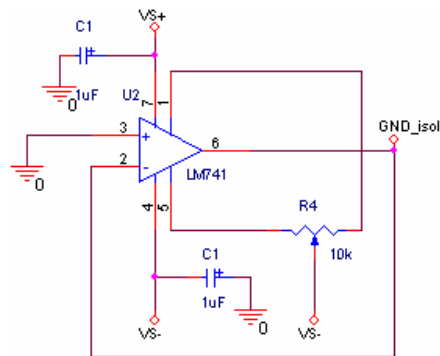


Figure 5.3. The isolated ground sub-circuit of the analog mixer device.

The isolated ground sub-circuit is presented in Figure 5.3. Its function was to provide a precise, isolated ground reference for the rest of the circuit. This was accomplished by using a follower circuit (with its positive terminal connected to the ground) that employed external nulling for the op-amp (accomplished via potentiometer R4 in Figure 5.3).

The LF 412 operational amplifier was chosen for the signal-processing portions of the circuit for its high bandwidth and stability (quoted equivalent input noise voltage of $25 \text{ nV} / \sqrt{\text{Hz}}$). The LM 741 operation amplifier was chosen for the reference buffer and the isolated ground circuit because it had the external null-setting option, which could be used to precisely set its voltage offset to zero.

The signal reported by the Data detector could be represented as a combination of DC signal plus three modulating components, as in Equation 5.2 below. The DC

component is due to ideal laser power. The actual laser's output also included its own modulation (S_{laser}), due to such factors as variations in the laser's temperature and oscillations in its imperfect power supply. The modulation due to changes in the sample's transmittance is designated S_{sample} . Finally, there is detector's own noise, $S_{noise-D}$.

$$S_{data} = DC + S_{laser} + S_{sample} + S_{noise-D} \quad (5.2)$$

Out of all these contributions, only DC and S_{sample} were desired. The oscillations due to the laser itself and the detector were extraneous. The modulation S_{sample} only had physical meaning in proportion to DC .

For these measurements, it is clear that S_{laser} would be expected to be the same at the two detectors (Data and Reference) up to some multiplication constant. However, the detector noise would be expected to be different; S_{sample} would be absent from the signal collected by the Reference detector. Therefore, the difference between the outputs of the two detectors should remove S_{laser} , as in Equation 5.3. The noise contributions are omitted in Equation 5.3.

$$S_{data} - a \cdot S_{ref} = S_{sample} \quad (5.3)$$

The scaling factor was obtained in absence of the signal modulation due to changes within the sample, such as prior to exposure, and corresponds directly to the scaling factor a in Equation 5.1 above. In absence of sample signal modulation, the analog mixer was adjusted to produce zero signal – hence the “rest signal nulling” description of the setup.

The *DC* component was obtained by blocking the reference beam and reading the mixer's output with a digital multimeter. Per Equation 5.1, as V_{ref} goes to zero, the system output becomes V_{data} .

The noise contributions were reduced by averaging data from multiple exposures, as described below in Section 5.1.1.3.

The rest-signal nulling approach was chosen over AC coupling because it was found that the laser's output carried oscillations with a frequency near 60 Hz whose amplitude exceeded the useful data signal. The frequency composition of this contribution was not distinct, which made frequency-filtering of data impossible. Simply filtering out all frequencies below some threshold (such as 100 Hz) was assumed to distort the sought signal, and thus was undesirable. Subtraction of the reference signal, as described above, was found to completely remove laser's own oscillations from the data.

In general, the observed modulation was quite small compared to the DC component. While the modulation's maximum amplitude was on the order of 5 mV, the DC component was about 2 V. Measuring such a small modulation reliably required at least rudimentary suppression of mechanical vibrations present on the table due to equipment mounted directly on the table (most notably the pulsed UV laser, which had a large power supply with a cooling fan). This was done by firmly attaching sheets of cork to the posts holding the optics and the detectors, and also bolting small pieces of cork sheets directly to the table. This was found to approximately half the random signal oscillations due to vibration.

Section 5.1.1.2

Data Collection

For each pulse of the UV laser, a single trace (output of the analog mixer) was recorded. Generally, several such traces were collected in sequence for each measurement, and then averaged using a procedure described below. The delay between successive exposures was approximately two minutes.

Raw data consisted of a voltage modulation provided by the analog mixer and the DC component which was captured by blocking the reference beam and measuring analog mixer's output with a digital multimeter. Since only relative changes in the signal were considered useful, the voltages were not re-calculated into real beam power values by accounting for the detectors' spectral responsivity.

Section 5.1.1.3

Data Processing

The recorded data traces $T_n(t)$ were converted into induced absorption coefficient through the procedure described below. Since data were affected by random, low-frequency oscillations, the individual trace had significant DC offsets with respect to each other. This was corrected by forcing the average of each trace for $t < 0$ to equal zero, providing adjusted signals $S_n(t)$ as shown in Equation 5.4:

$$S_n(t) = T_n(t) - \overline{T_n(t < 0)} \quad (5.4)$$

After individual traces were baseline-corrected in this way, they were averaged together:

$$S(t) = \frac{1}{N} \sum_n S_n(t) \quad (5.5)$$

Finally, using the sample's thickness z and the recorded *DC* component, the induced absorption was calculated:

$$\Delta\alpha(t) = -\frac{1}{z} \ln\left(\frac{DC + S(t)}{DC}\right) \quad (5.6)$$

These calculations – from raw data to induced absorption values – were carried out by a Python script, which allowed for an automated analysis of the data. Normally, each measurement consisted of twenty individual traces.

Section 5.1.1.4

Data Accuracy

The accuracy of these data can be evaluated in several ways. The first is to compare calculated uncertainty for each value of t to the total amplitude of the signal, providing an estimate of the signal-to-noise ratio (SNR):

$$SNR = \frac{A}{\left(\frac{\sigma(t)}{N}\right)} \quad (5.7)$$

The maximum observed amplitude was about 5 mV, and the average uncertainty was about 50 μ V, providing a maximum SNR value of 100.

Another measure of accuracy would be to calculate the standard deviation of $\Delta\alpha(t < 0)$ and compare it to the maximum amplitude of induced absorption. Standard deviations for several samples averaged to $3 \times 10^{-4} \text{ cm}^{-1}$, while the maximum absorption was observed at about 0.017 cm^{-1} . This gives an SNR value of 57.

Section 5.2

Data and Results

A representative subset of the experimental sample suite was subjected to the tests described in the previous section. As the UV tests were designed to mirror the HERMES III tests, discussion of the gathered data is likewise similarly organized. The transient and the permanent response data are discussed separately, further broken out by composition.

The subset of samples tested included all the composition and manufacturer groups. This included all three types of undoped YAG – one sample from Airtron-Litton designated as “AL”, and two samples from the Scientific Materials Corp., designated as “SM avg” and “SM high,” referring to their purity (refer to Section 3.3.2).

Only two concentrations of Nd:YAG were tested, those available from the United Crystals Co. No Nd:YAG sample from the Scientific Materials Corp. was available in the appropriate size. For the labeling to be consistent with Chapter IV, the Nd:YAG samples in this chapter as still labeled as “UC.” Similarly, the Cr³⁺:YAG sample from the Scientific Materials Corp. was also not tested.

Two co-doped Cr,Nd:YAG samples were tested. One from Airtron-Litton, labeled “AL,” and one from the Scientific Materials Corp., labeled “SM.” Only one composition provided by the Scientific Materials Corp. was tested (1.0 at% Cr³⁺, 1.2 at% Nd:YAG). No sample with the other composition (0.5 at% Cr³⁺, 1.0 at% Nd:YAG) was available in the appropriate size.

Section 5.2.1

Transient Response to UV Irradiation

Section 5.2.1.1

Undoped YAG

Samples of undoped YAG were UV-irradiated in the UV-NIR pump-probe experiment (UNPP). The data for the undoped YAG samples are shown in Figure 5.4. As can be seen in the figure, all of the undoped YAG samples showed induced absorption at 1064 nm that began to anneal at room temperature. The data are shown in Figure 5.4. The absorption response is characterized by a relatively quick onset. Relaxation appears to take place in two stages. During the first stage, depending on the sample, between 30% and 100% anneals within approximately 250 μ s, with the purest sample exhibiting the greatest degree of anneal. The second stage follows a much slower rate of decay.

Overall, while the maximum initial absorption is similar between the three samples (approximately 0.006 cm^{-1}), amplitude of the slower component appears correlated with the samples' purity levels. The Airtron-Litton sample (labeled "AL") shows the most overall absorption. Meanwhile, the purest Scientific Materials sample (labeled "SM, high") anneals completely in less than 0.5 ms.

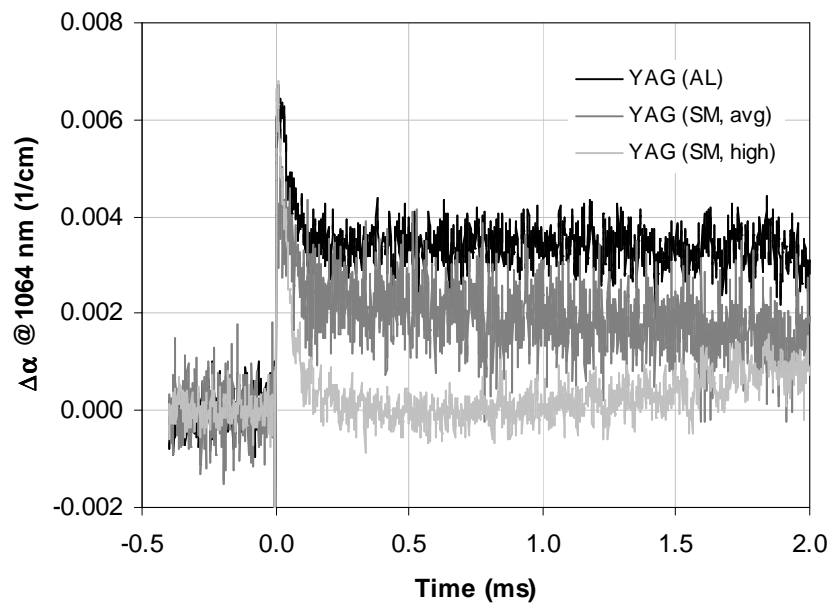


Figure 5.4. Induced absorption at 1064 nm due to a pulse of UV in undoped YAG samples.

The samples can further be compared using a log-linear plot, as presented in Figure 5.5 below.

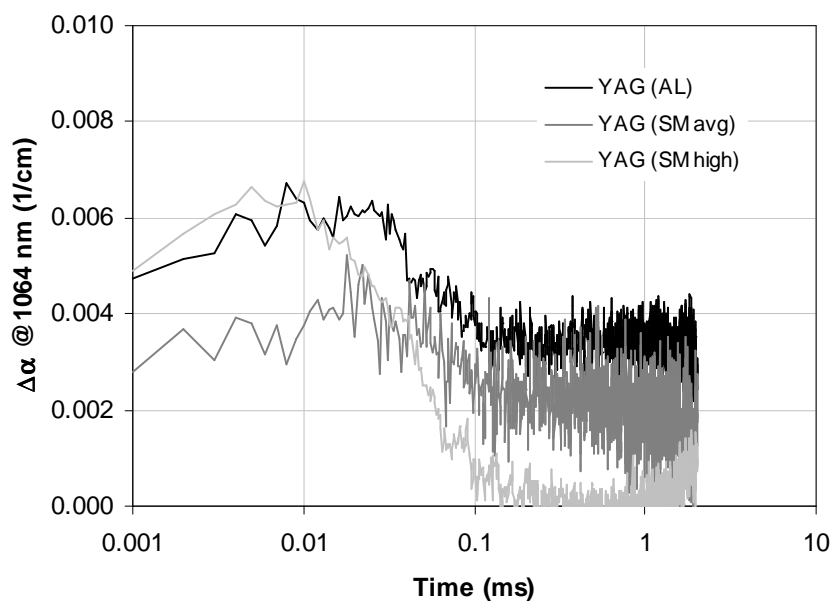


Figure 5.5. A log-linear plot of data from Figure 5.4.

In Figure 5.5 above, roughly three regions of behavior can be identified. Up to 0.001 ms, a slight increase in absorption is observed in all three samples. Past this point, relaxation of induced absorption begins across all the samples. The rate of decay (as indicated by the slope of the curve in the log-linear plots) stays nearly constant from 0.01 ms to 0.1 ms. Past 0.1 ms, a slower decay rate is observed.

Section 5.2.1.2

Nd:YAG

Samples of two concentration levels (0.5 at% Nd and 1.2 at% Nd) from United Crystals were tested using UV irradiation. Samples from Scientific Materials (1.0 at% Nd) were not available in an appropriate size, and so were not tested in this experiment.

Transient absorption was induced in all the Nd:YAG samples tested, as seen in Figure 5.6. Parallels similar to the case of undoped YAG can be drawn using the Nd:YAG data. The fast absorption process, with an approximate lifetime of 10 μ s, that is present in the H3 data, is seen to be absent from the UV data. Conversely, the slow component, with lifetimes on the order of 1 ms, is present in both sets of data.

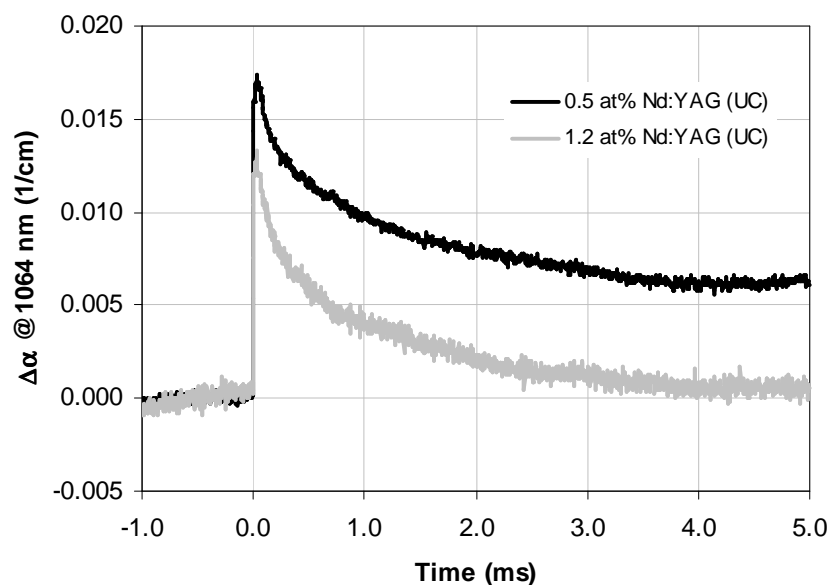


Figure 5.6. Induced absorption at 1064 nm due to a pulse of UV in Nd:YAG.

A further examination of the UV data is presented below in Figure 5.6 on the log-linear scale, facilitating identification of exponential components of the relaxation process.

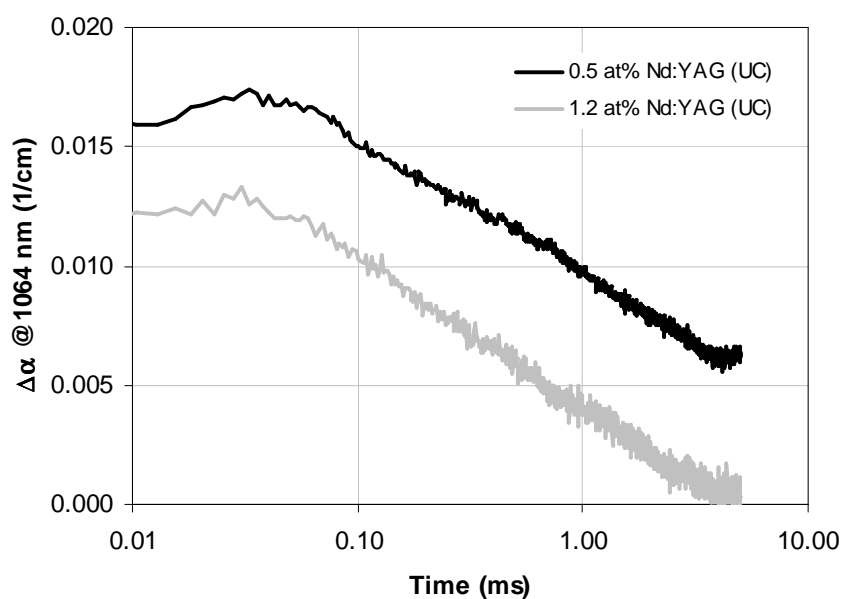


Figure 5.7. A log-linear plot of the data from Figure 5.5.

As can be seen in Figure 5.7, the curves indeed consist of roughly linear segments. The response is nearly flat up to approximately 0.04 ms, after which a nearly exponential relaxation process begins. The rate of this relaxation process is similar between the two samples, as indicated by the nearly equal slope of the two lines past 0.1 ms.

Section 5.2.1.3

Cr^{3+} :YAG

Samples of two concentration levels (0.5 at% Cr and 2.0 at% Cr) from United Crystals were tested in this experiment.

In contrast to H3 data, the detectable levels of absorption were readily observed in Cr^{3+} :YAG when exposed to the pulsed UV radiation. At 1064 nm, a small amount of induced absorption appeared, as seen in Figure 5.8. Samples with higher concentrations of chromium appear to have developed less absorption in response to the UV irradiation of the same pulse energy.

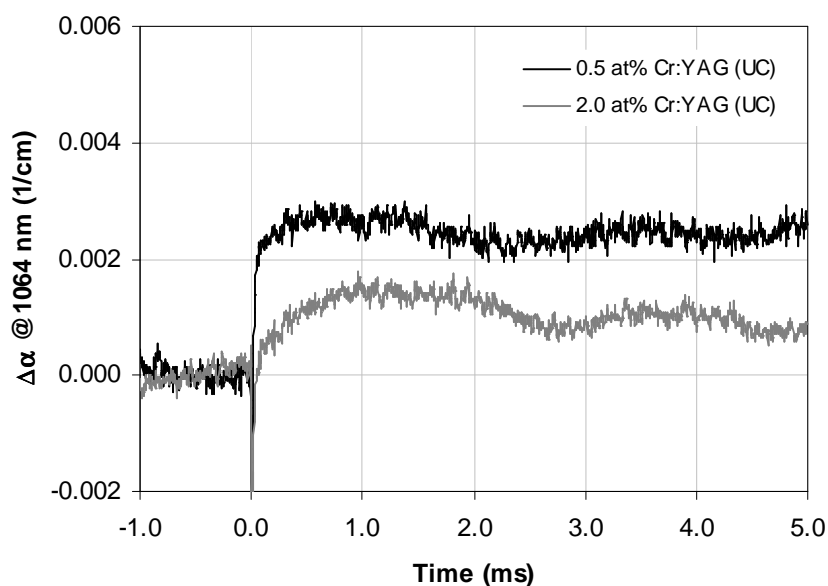


Figure 5.8. Induced absorption at 1064 nm due to a pulse of UV in Cr:YAG.

Upon a visual inspection of the Cr^{3+} :YAG samples following a UV irradiation, it was also noted that their color had changed from green to brown. This coloration

persisted for several hours, and so it was possible to measure the absorption spectrum associated with the color change.

Observed induced absorption (measured approximately five minutes past the UV irradiation) is shown below in Figure 5.9. The additional absorption observed in a 0.5 at% Cr³⁺:YAG sample (supplied by United Crystals) consisted of several wavelength regions of positive absorption contribution. These regions included an increase in absorption below 310 nm, a group of broad positive peaks between 310 nm and 650 nm (peaking at 480 nm), and a small broad contribution between 700 nm and 800 nm.

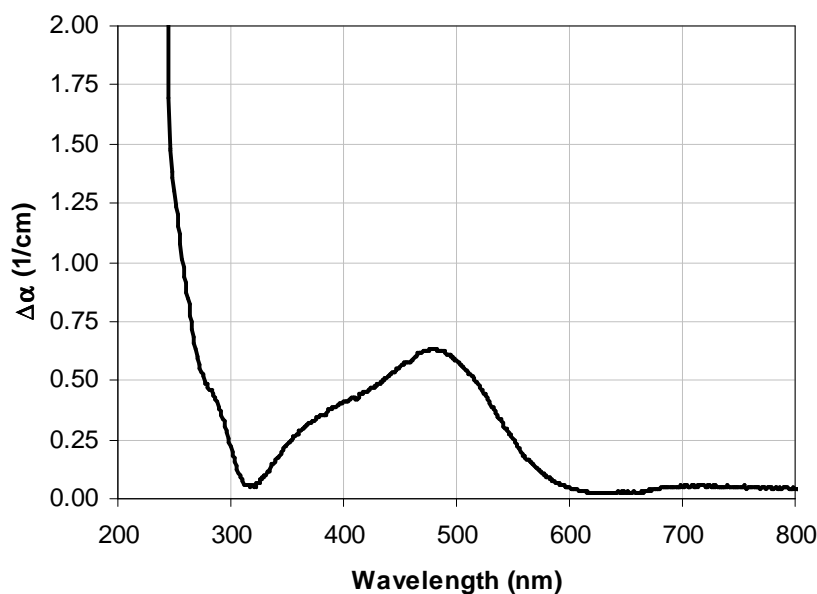


Figure 5.9. Differential absorption induced in 0.5 at% Cr³⁺:YAG (UC) by irradiating with 248 nm UV light. Spectrum taken approximately five minutes after exposure.

Since this absorption relaxed in the matter of hours, it was possible to accurately record its kinetics using fixed-wavelength, time-resolved measurements (a measurement option available on the Perkin-Elmer Lambda 950 UV-Vis spectrometer used in this

study). The spectrometer was set to 480 nm and recorded absorption over the course of two hours. The resulting data are shown in Figure 5.10.

From the time-resolved observation of absorption in Cr:YAG both on the short time scale (from the UNPP experiment in Figure 5.8), and from long-term spectrometer observations (Figures 5.10), it can be seen that the amplitude of the induced absorption decreased with increasing chromium concentration. It is also evident from Figure 5.10 that the rate of relaxation grew with increasing chromium content.

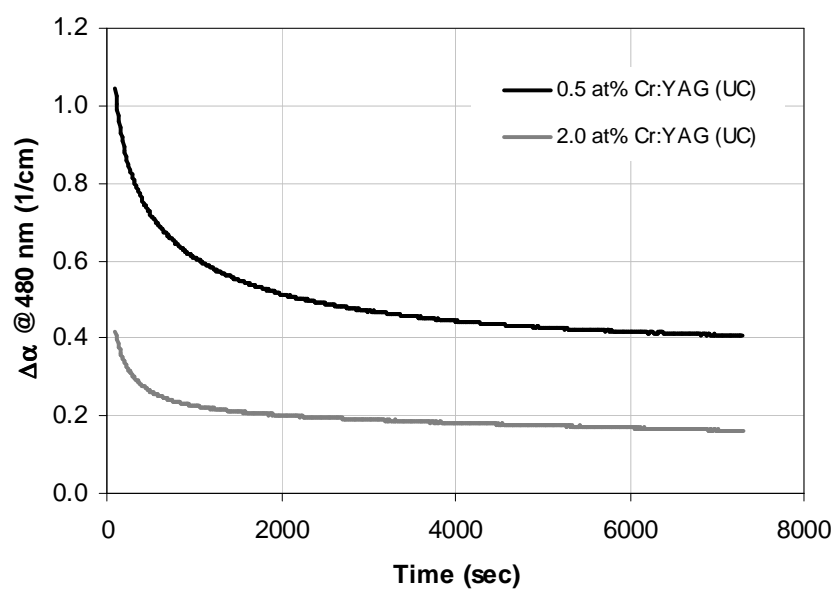


Figure 5.10. Induced absorption at 480 nm due to UV irradiation in Cr:YAG. Origin of the time axis corresponds to the end of UV irradiation.

Section 5.2.1.4

$Cr^{3+}, Nd:YAG$

Figure 5.11 shows the absorption behavior at 1064 nm of the two co-doped materials when exposed to the pulsed UV irradiation in this experiment. The Airtron-Litton sample, with the low chromium content, shows a small amount of induced absorption which tends to anneal at room temperature. By contrast, the Scientific Materials sample, with the high chromium content, shows a peak of signal gain, followed by a small amount of absorption that also tends to anneal at room temperature.

Unfortunately, the 0.5 at% Cr, 1.0 at% Nd:YAG samples from the Scientific Materials Corp. were not tested because no samples of this composition were available in an appropriate size.

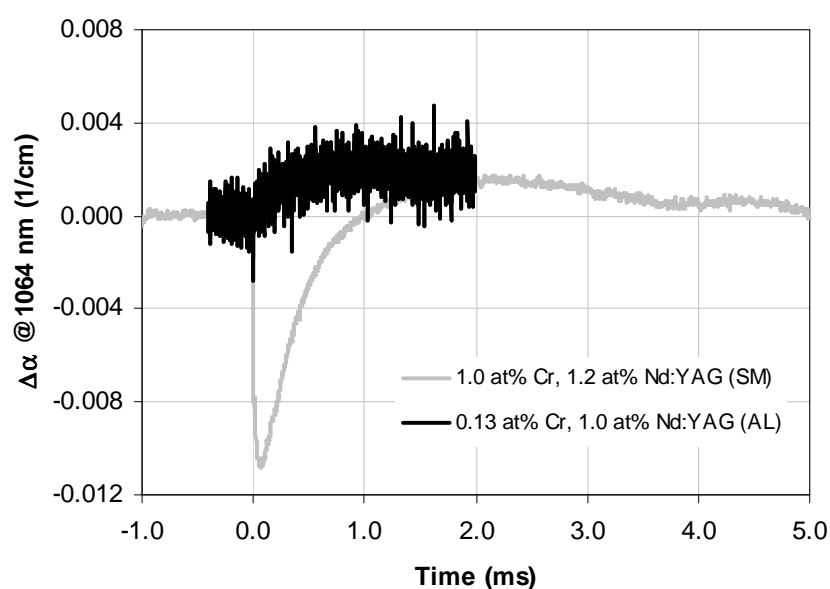


Figure 5.11. Induced absorption at 1064 nm due to a pulse of UV in Cr,Nd:YAG. Negative induced absorption indicates gain.

It is noteworthy that the co-doped samples exposed to UV irradiation exhibited a change in color (from green to brown) similar to the color change seen in the singly-doped Cr^{3+} :YAG samples (described in the previous section). As with the singly-doped samples, coloration persisted for some time in the co-doped samples, which made detailed absorption spectroscopy observations possible. These results are presented below in Figure 5.12.

The differential absorption consisted of several broad positive contributions. Notably, there was an increase in UV absorption below 315 nm, a broad peak centered near 480 nm, and further minimal absorption contribution past 700 nm. Generally, these features matched those observed in the Cr^{3+} :YAG samples (see Figure 5.9 above).

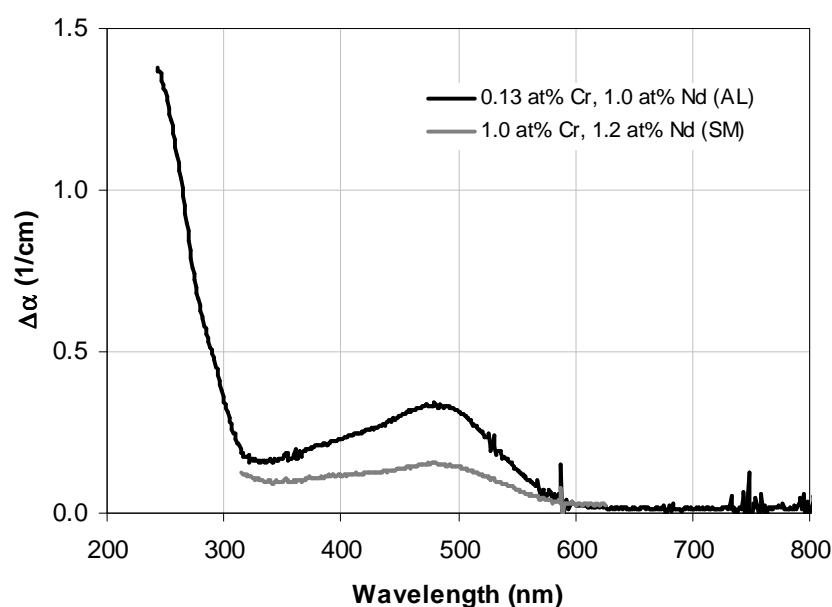


Figure 5.12. Transient differential absorption in Cr,Nd:YAG samples due to pulsed UV irradiation at 248 nm.

Section 5.2.2

Permanent Response to UV Irradiation

Section 5.2.2.1

Undoped YAG

The UV-induced steady-state differential absorption profiles of the undoped YAG samples are shown in the Figure 5.13 below. These spectra were collected within two hours of UV exposures. The samples were kept at room temperature and ambient humidity conditions. The trends depicted were similar to those observed under the gamma irradiation. Differential absorption features included a negative peak centered near 255 nm, and a positive peak (with maximum between 310 and 400 nm) that extended across the visible and into the near infrared part of the spectrum. These data were collected several hours after the UV irradiation.

Data presented in this section were based on irradiation of samples of approximately 2 mm in thickness with 5000 pulses of UV irradiation (average pulse energy of about 5 mJ, for a total dose of approximately 100 J/cm²). The data taken after 2500 pulses did not significantly differ from these data, suggesting that the differential absorption measured had reached its point of saturation for the data reported here.

The amount of the induced absorption is positively correlated with the level of contamination as reported by SIMS results (see Chapter III, Section 3.3.2 for purity data, and Chapter IV, Section 4.2.2.1 for similar data from the HERMES III experiments).

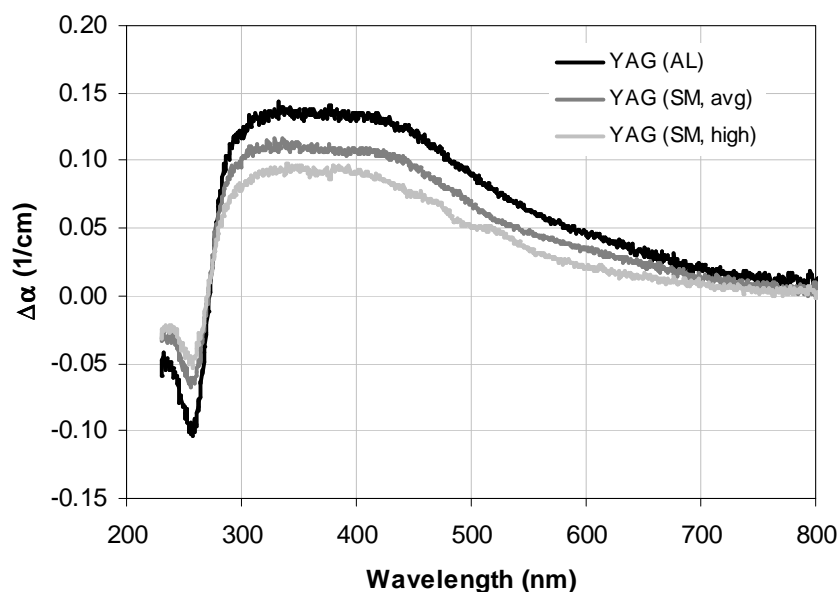


Figure 5.13. Differential absorption in undoped YAG due to pulsed UV irradiation at 248 nm. Data shown are from an Airtron-Litton sample (black curve), average purity Scientific Materials sample (dark gray curve), and the high-purity Scientific Materials sample (light gray curve). Data for the YAG (SM high) sample was vertically shifted to compensate for an erroneous offset in the raw data.

The maximum values of the induced absorption (taken between 300 nm and 400 nm in Figure 5.13 above) did not reach the levels induced by gamma irradiation (refer to Figure 4.9). The post-irradiation differential absorption for the case of UV was only about 50% of the values achieved in the case of the gamma irradiation.

In the original data, permanent absorption in the high-purity Scientific Materials sample appeared to reach greater amplitude than other (in the reference region between 300 nm and 400 nm), less pure samples. This contradicted behavior trends observed in permanent induced absorption observed under gamma irradiation (refer to Figure 4.9 and its associated discussion). This was attributed to an erroneous offset in the data from the

YAG (SM high) sample. The offset was corrected by vertically shifting the data to force it to tend toward zero near 800 nm. The shift was the only correction applied – no scaling was used.

Section 5.2.2.2

Nd:YAG

Similarly to the undoped YAG, the UV irradiation resulted in steady-state differential absorption in the Nd:YAG samples as well. These changes are shown below in Figure 5.14. Differential absorption spectra consisted of a negative peak near 255 nm and a positive peak near 320 nm that extended across the visible and into the UV. Nd:YAG samples from Scientific Materials were not tested as they were not available in an appropriate size.

The data presented in this section were based on irradiation of samples of approximately 2 mm in thickness with 5000 pulses of UV irradiation (average pulse energy of about 5 mJ, for a total dose of approximately 100 J/cm²). Data taken after 2500 pulses did not significantly differ from these data, suggesting that additional absorption had reached the point of saturation.

While identical compositions tested at HERMES III reached nearly 0.5 cm⁻¹ of differential absorption at their peak, samples under the UV irradiation reached maximal values of approximately 0.25 cm⁻¹. This agrees with the trend observed in the data from the undoped YAG samples, in which gamma radiation induced a greater change in the differential coefficient of absorption.

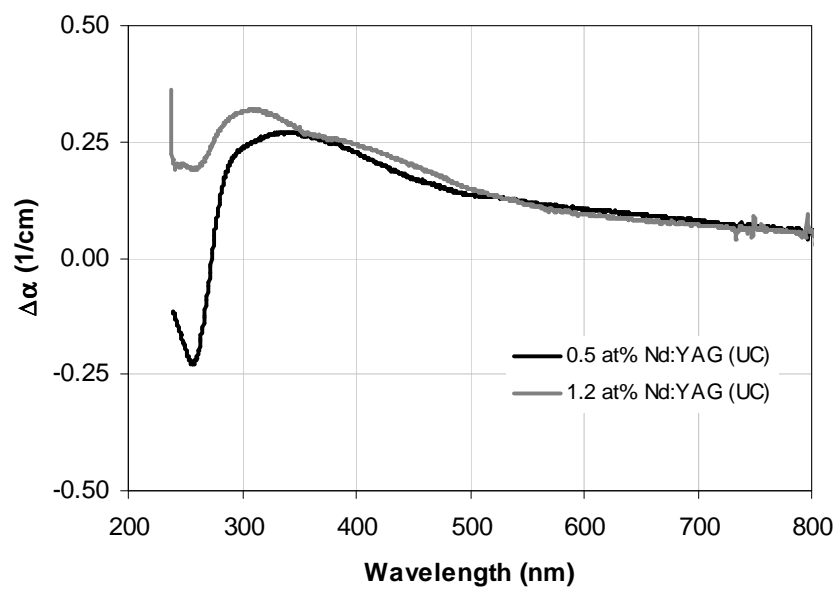


Figure 5.14. Additional absorption in Nd:YAG due to pulsed UV irradiation at 248 nm.

Section 5.2.2.3

Permanent Response of Cr^{3+} :YAG and Cr^{3+} ,Nd:YAG

No permanent differential absorption was observed in the samples containing chromium. Though they did exhibit some form of differential absorption, it was unstable at room temperature, with the samples returning to their pre-irradiation state within a matter of hours. These changes were discussed in Section 5.2.1.3 and 5.2.1.4, respectively.

Section 5.3

Numerical Data Analysis

Several means of numerical analysis have been applied to the data in the UNPP tests to quantify the data. These included the same types of analysis as followed in Chapter IV for the gamma irradiation data, namely the effect of dose on induced transient absorption and a simple numerical modeling of the processes making up the observed behavior.

As has been reported in Section 5.2.1.3 of this Chapter, chromium-bearing samples have been observed to develop temporary differential absorption in response to the UV radiation. In order to quantify this finding, a deeper analysis was performed – and described in this Section – in an attempt to determine whether similar minute changes in absorption were induced in the Cr³⁺:YAG samples during the gamma irradiation tests. Since this differential absorption was completely gone within approximately 24 hour of exposure, and samples irradiated at HERMES III were not available for further testing for approximately a year after the exposures, no further comparison of spectroscopy data from the H3 experiments could be made available for this analysis.

Section 5.3.1

Correlation of Fluence and Induced Absorption

The greater control over the experimental variables in the UNPP test, as compared to the HERMES III test, allowed for a finer examination of the relationship between the incident irradiation dose and the induced transient absorption. An experiment was constructed, in which UNPP data were collected for the same sample over a range of pulse energies. Since magnification was not changed between the tests, the pulse energy was directly proportional to the energy flux at the sample surface. The pulse duration was reasonably assumed not to have changed appreciably between tests, and so this experiment tested the dependence of the induced transient absorption on the incident UV power flux.

One representative sample was thus tested, 0.5 at% Nd:YAG. The data for this sample are presented below in Figure 5.15.

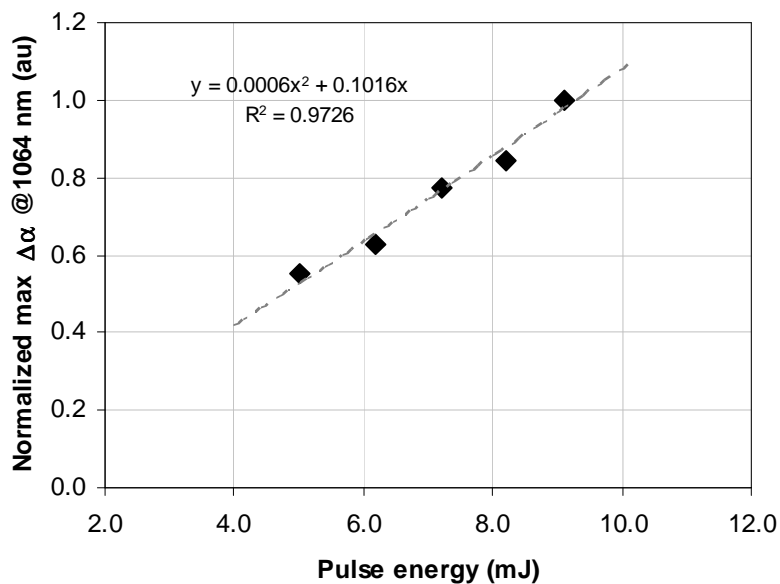


Figure 5.15. Dependence of maximum UV-induced absorption in 0.5 at% Nd:YAG (UC) on pulse energy of the UV laser.

A linear fit (with the y-intercept fixed at zero) satisfied this set of points with a correlation of 0.97. Several polynomial fits of higher degree were also attempted, using a quadratic and a cubic function. In all cases, the y-intercept was again forced to be zero. Quadratic and cubic terms in these fits were several orders of magnitude lower than the linear term. These fits did not provide a significant increase in the fit's correlation score.

This strongly indicated that at least for the Nd:YAG samples, there was a linear dependence of UV-induced transient absorption on the incident power flux.

Section 5.3.2

Re-Examination of HERMES III Data from Cr³⁺:YAG Data

The UV/NIR Pump-Probe experiment revealed a small amount of induced absorption in Cr:YAG samples (refer to Figure 5.8). In the original examination of Cr:YAG data from the gamma irradiation experiments (refer to Chapter IV, Section 4.2.1.3), no such corresponding phenomenon was observed. Since many other behaviors appeared to be replicated between the two means of irradiation, a closer statistical analysis was performed to determine if H3 data indeed contained an increase in absorption in Cr:YAG samples.

The analysis relied on what is termed “Method of Quasi-Derivates,” which essentially calculated numerical derivatives using large, averaged subsets of the data. This method, and the results of its applications to the HERMES III data, are described in the two subsequent sections.

Section 5.3.2.1

Method of Quasi-Derivatives

Let us assume that gamma irradiation induced a physical process in Cr:YAG samples that was similar to that induced in the same samples by the UV irradiation. That is, it induced a relatively small amount of absorption with a lifetime on the order of at least several minutes. Although this absorption decays away, its lifetime is much longer than the time scale on which much of the data was gathered. A process with a lifetime that is at least four orders of magnitude greater than the time scale on which the data are being studied can be considered to be a constant.

Then, similar to observations in the UNPP experiments, if analyzed on the timescale of several milliseconds, the induced absorption in the gamma-irradiated Cr:YAG samples should approximate a step function.

The absorption signal is obscured by a broad spectrum of noise arising from both rapid oscillations (largely due to instrument noise) and slow changes in offset (largely due to drifts in the laser's power output). Examination of the gamma data in Figure 4.7 reveal that the rapid oscillations exceed the amplitude of the sought absorption signal, obscuring its observation in visual inspection. The slow oscillations may also compete with the absorption signal, and give false positives.

The first challenge (rapid oscillations) can be overcome by increasing the time averaging windows (since contribution from additive noise goes down as a square root of integration time, Frieden 2001). The second challenge can be overcome by observing whether the increase in absorption coincides with the gamma pulse (which would suggest

that it represents real data), and if such increases repeat from sample to sample (eliminating the concern that the signal results from random noise oscillations).

The method of quasi-derivatives involves calculating a value similar to a numerical derivative. Given a set of points P_n that correspond to times t_n (time recorded at intervals Δt), numerical derivative at t_n can be defined in the following way:

$$m(t_n) = \frac{P_{n+1} - P_{n-1}}{2\Delta t} \quad (5.8)$$

In order to minimize contributions from rapid oscillations due to noise, we can take averages over preceding and following regions (each region containing N points):

$$M(t_n) = \frac{1}{TN} \left(\sum_{j=n+1}^{n+N} P_j - \sum_{j=n-1}^{n-N} P_j \right) \quad (5.9)$$

In Equation 5.7, T represents the length of time corresponding to N points. Since every point in set $M(t_n)$ would be divided by the same factor TN , we can omit it and not define T exactly:

$$M(t_n) = \sum_{j=n+1}^{n+N} P_j - \sum_{j=n-1}^{n-N} P_j \quad (5.10)$$

We can further normalize each set:

$$M_{norm}(t_n) = \frac{1}{\max\{M\}} M(t_n) \quad (5.11)$$

Since this method tracks value of quasi-derivative over time, it is possible to account for coincidence of peaks by adding all the sets of data together. Then, only the features that are coincident in time and common to all sets of data should maximally contribute.

Section 5.3.2.2

Results of Analysis

The first composition we examine is 0.5 at% Cr:YAG. Five sets of HERMES III data (from three samples) were available for this test. Results of the above analysis are shown in Figure 5.16. Both graphs, M and M_{norm} , show a positive spike at $t = 0$, which is consistent with the hypothesis expressed above – there is a step-wise increase in absorption in Cr:YAG.

Additionally, there are other spikes, positive and negative, most prominently observed in non-normalized data for between 10 and 20 ms. Here, positive peaks are usually followed by negative peaks of similar area and duration. By construction of M , this indicates oscillatory behavior in absorption signal. Since such oscillatory behavior has been observed in all traces, regardless of sample composition and even in the case of no-sample reference shots, it can be attributed to equipment noise. Therefore, these oscillations are a measurement artifact.

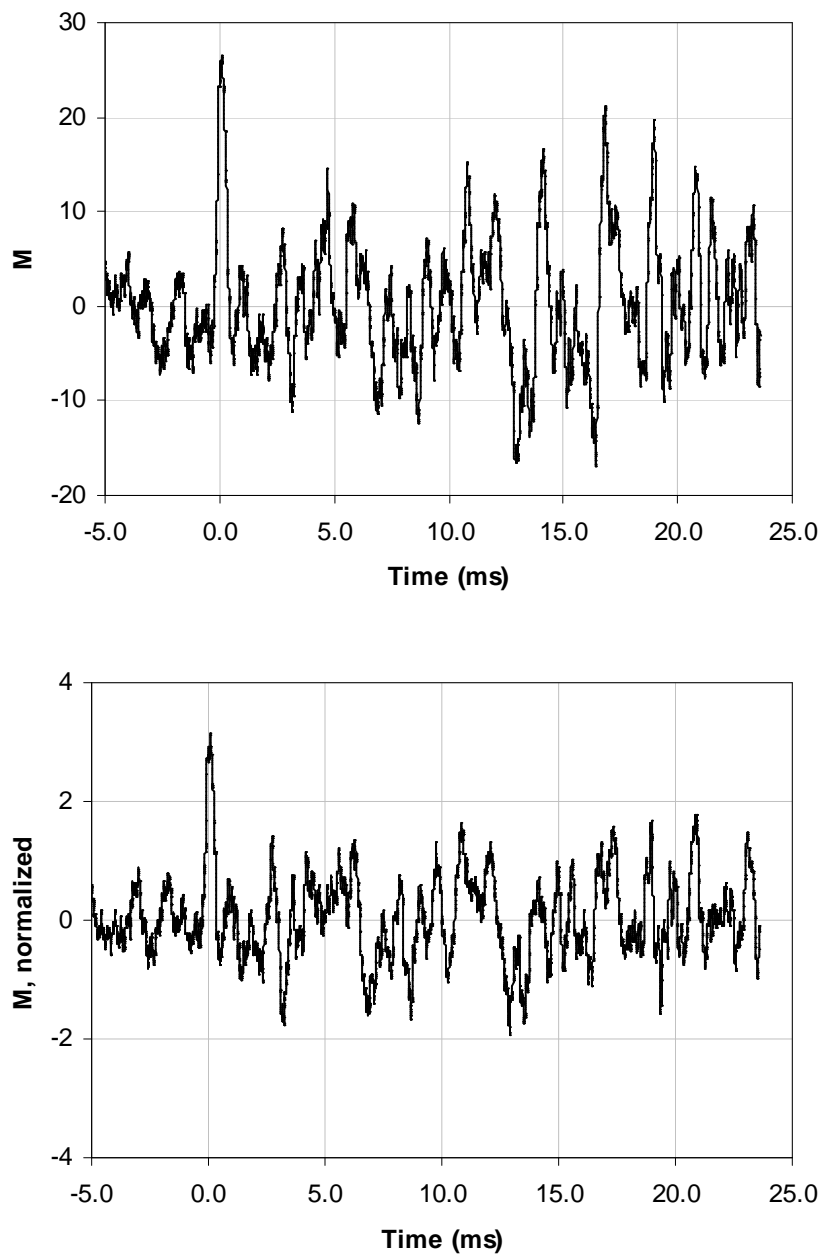


Figure 5.16. Quasi-derivatives calculated for 0.5 at% Cr:YAG (UC). Averaging included 200 data points (approximately 0.4 ms).

Figures 5.17 and 5.18 show sums of normalized quasi-derivatives (M_{norm}) for 1.5 at% Cr:YAG and 2.0 at% Cr:YAG, respectively. In this graph, no discernible spike

appears at $t = 0$. All other peaks and valleys appear to correspond to oscillatory changes in absorption described above. Therefore, no step-wise increase in absorption can be ascertained in the samples of higher chromium content.

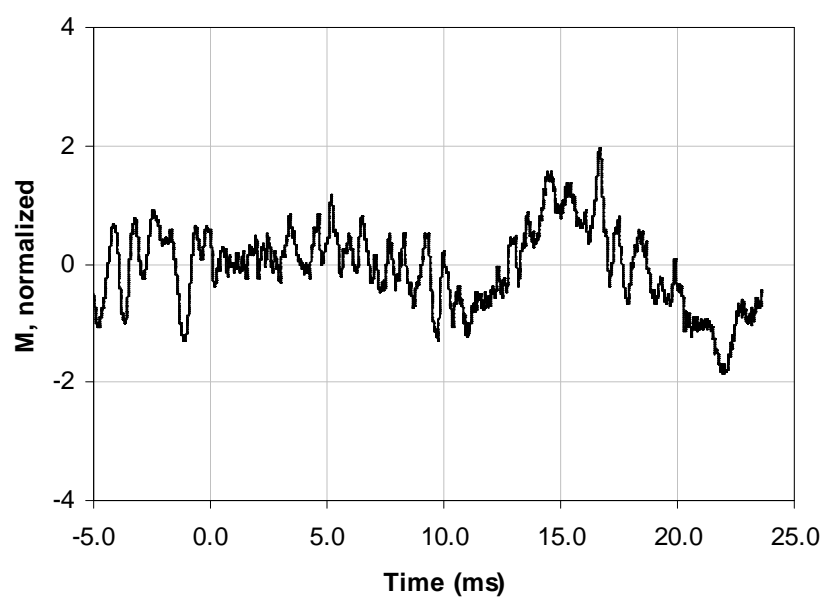


Figure 5.17. Normalized quasi-derivative for 1.5 at% Cr:YAG (SM).

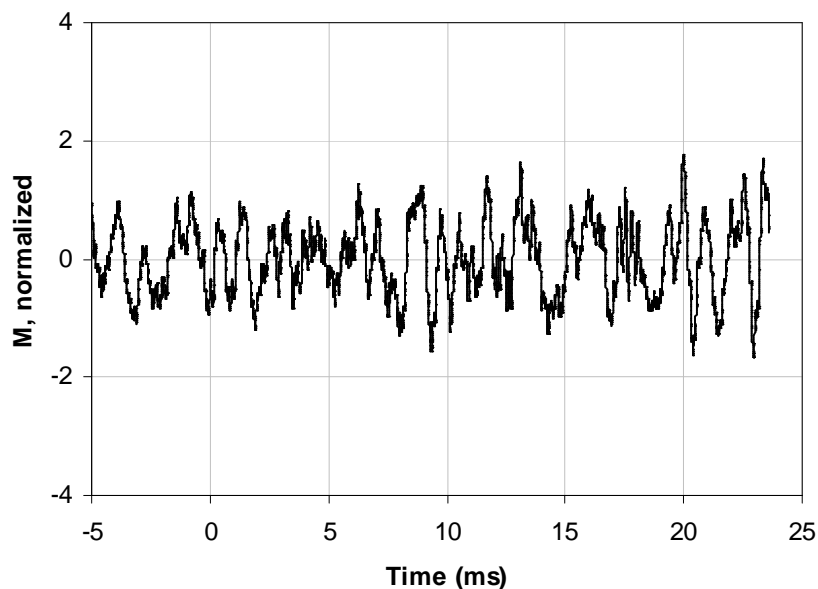


Figure 5.18. Normalized quasi-derivative for 2.0 at% Cr:YAG (UC).

Due to this difference, increases in absorption in higher-content Cr:YAG samples should be masked by slow oscillations due to the instrumentation. As seen in Figure 5.16, such oscillatory behavior is on the order of magnitude of the induced absorption. Therefore, if, relative to the 0.5 at% Cr:YAG material, the amplitude of the induced absorption were reduced, and its onset were no longer step-wise, it would be obscured by the oscillating artifacts in the measurements.

As a result, we can only suggest that some similarity in the induced absorption behavior at 1064 nm due to ionizing radiation (UV and gamma) exists in lower-content Cr:YAG materials. Analysis of data from higher-content Cr:YAG is inconclusive.

However, the following should be further noted. If the behavior of gamma-induced absorption in Cr:YAG is indeed identical to UV-induced absorption in Cr:YAG,

then higher-content chromium-doped YAG would not have responded in a step-wise fashion. In UNPP experiments, UV-induced photodarkening in high-chromium Cr:YAG samples had a smoother onset with a finite rise time (see Figure 5.8). In that figure, while onset of absorption in the 0.5 at% Cr³⁺:YAG sample is essentially instantaneous, absorption takes approximately 1 ms to reach its maximum in the 2.0 at% Cr³⁺:YAG sample. Given that the window of averaging in the above analysis was approximately 0.4 ms, such a slow onset of absorption would appear gradual, and not step-wise.

Section 5.4

Interpretation and Discussion of Results

The data and analysis presented in the above sections lends itself to a discussion in terms of conclusions drawn in the previous chapter, as well as previous work published by other researchers. In particular, a number of similarities can be identified between the effects of pulsed UV radiation described in this chapter and the effects of pulsed gamma radiation described in the previous chapter. Furthermore, an analysis of the UV data can shed further light onto some observations outlined in the chapter covering results of the gamma irradiation, as exemplified by statistical analysis probing the presence of gamma-radiation induced absorption in the Cr:YAG samples (presented in Section 5.3.2).

In this section, an argument is made that both UV irradiation and gamma radiation induce generally the same types of processes in single crystal YAG materials studied within this report. An optically-induced Cr^{4+} color center is also discussed based on the UV data.

Section 5.4.1

Physical Interpretation of Data

Section 5.4.1.1

Identification of Cr^{4+} Centers

As reported in Chapter IV, differential absorption was induced in chromium-bearing samples via ionizing radiation. In most cases, this differential absorption was unstable at room temperature, with a characteristic lifetime on the order of tens of minutes. While this made investigation of differential absorption impossible in most cases (with the exception of the low-chromium samples) for the case of the gamma ray exposure, it was possible to record these spectra in the case of the UV irradiation due to the samples handling and access issues previously discussed. Examples of these changes are reproduced below, in Figure 5.19.

An interpretation of the induced bands is based on the work of Feldman et al. (2003). In their work, Feldman et al. analyzed Ca,Cr:YAG samples that had undergone a variety of annealing treatments (in various controlled atmospheres). They were further able to break down the observed band structure and isolate the three possible states of chromium, assigning specific electronic transitions to specific absorption bands for the materials. In particular, they assigned three bands between 360 nm and 480 nm to Cr_{octo}^{4+} . Using these assignments, it was possible to perform a fit using data from Figure 5.18 above. In these fits, UV bands were ignored, because varying contribution of the UV absorption edge made these points unreliable. Observed absorption contributions past 650

nm were also ignored, as they were too small in amplitude and too broad in width to yield meaningful fits.

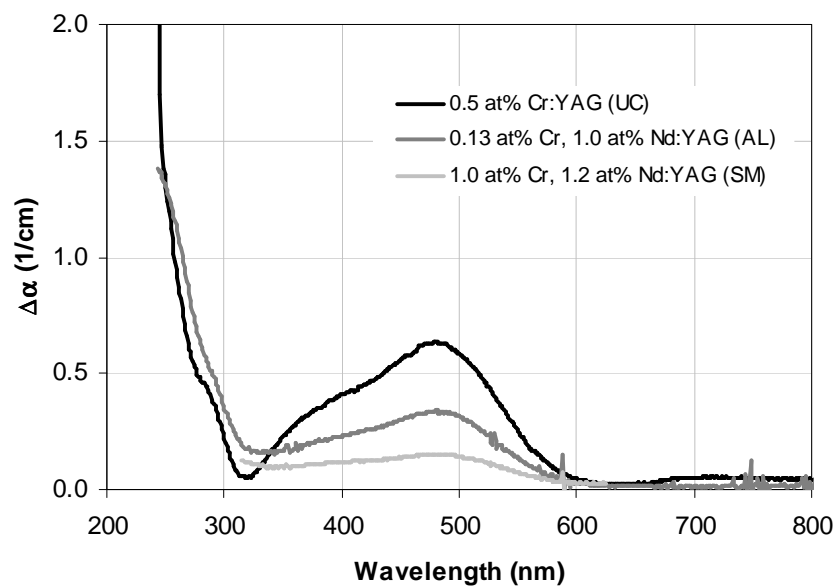


Figure 5.19. UV-induced differential absorption in chromium-bearing YAG samples. “AL” stands for Airtron-Litton, “SM” for Scientific Materials, and “UC” for United Crystals, referring to the sample manufacturer.

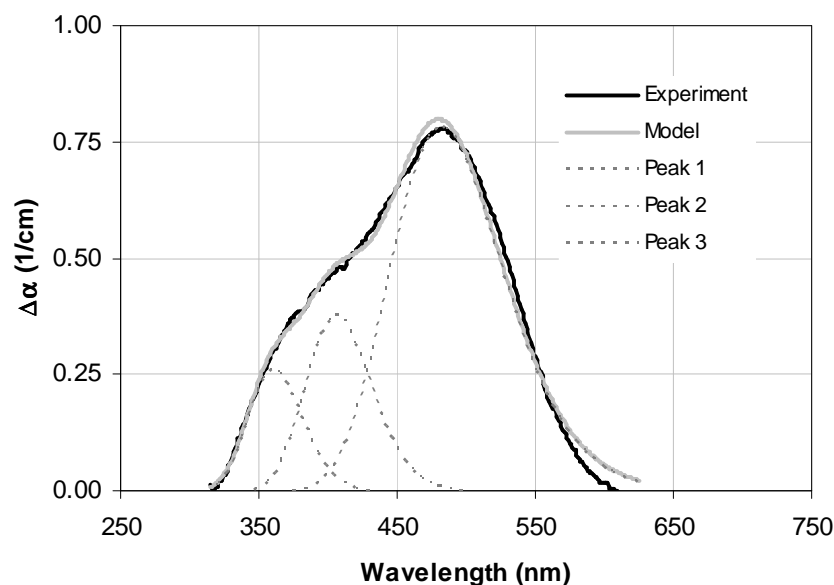


Figure 5.20. Experimental data and the model for absorption in 0.5 at% Cr:YAG. Peak positions from Feldman et al. (2003). Fit peak positions: 482 nm, 406 nm, 361 nm. Peaks were modeled as Gaussians. Positions were fixed, while widths and amplitudes were left adjustable.

The fit shown in Figure 5.20 above shows strong agreement between the model (peaks attributed to Cr_{octo}^{4+}) and the real differential absorption data (taken from 0.5 at% Cr:YAG). Therefore, it is reasonable to attribute the peaks to Cr_{octo}^{4+} . The results obtained in this fit are compared to those published by Feldman et al. in Table 5.1 below.

Table 5.1

Band		$\Delta\nu_{FWHM}$ (cm ⁻¹)	
λ (nm)	ν (cm ⁻¹)	This report	Feldman et al. (2003)
482	20740	4175	4410
406	24625	3502	6930
361	27710	3592	6350

Table 5.1. Comparison of fitting results from the fit presented in Figure 5.19 and those published by Feldman et al. In the fitting procedure used here, band positions were fixed, while peak amplitude and widths were varied.

Another notable feature of the differential absorption depicted in Figure 5.19 is the absence of bands associated with recharging of the iron impurity (refer to Figures 4.20 and 4.21). Positive absorption contributions from the Fe^{2+} defect are known to have a maximum near 320 nm, and to contribute strongly to absorption near 600 nm. However, in Figure 5.19, differential absorption tends toward zero at these positions, indicating that the presence of iron in the lattice had little or no effect on the induced absorption in the Cr-containing samples. This is despite the fact that these samples contained approximately the same amounts of iron as other samples (see Chapter III, Section 3.3.2).

Therefore, it is possible to claim that in chromium-bearing samples tested in this report, the differential absorption is dominated by the Cr_{octo}^{4+} color center, and evidence for recharging of the iron impurity is essentially absent.

A further comparison between the data discussed above (in Figure 5.19) and the data presented for the low-chromium co-doped sample from HERMES III experiments (see Figure 4.11, Chapter IV, Section 4.2.2.4) shows that the induced bands of absorption bear strong similarity. This suggests that both the UV and the gamma irradiation can create Cr_{octo}^{4+} color centers in the chromium-bearing YAG materials.

Section 5.4.2

Comparison with HERMES III Transient Data

As has been pointed out by previous researchers, different types of ionizing radiation affect optical properties of YAG in similar ways. Therefore, a comparison is warranted between the two data sets described above, in this and the previous chapters.

By design, UV experiments measured quantities directly comparable to those measured in the gamma irradiation experiments. Therefore, the comparison can be carried out directly, side-by-side. This analysis revealed that transient gamma-induced effects were largely replicated by the UV experiments, in particular for the case of the co-doped materials. The permanent effects in YAG and Nd:YAG were also strongly similar between the two modes of irradiation.

Section 5.4.2.1

Undoped YAG

Results of the transient UV (as described above in Section 5.2.1.1 of this Chapter) and transient gamma (Chapter IV, Section 4.2.1.1) experiments are shown side-by-side below in Figures 5.21 and 5.22. Since absolute values in the two cases were different, data from the gamma experiments were scaled down for the purpose of this comparison as the focus here is on the functional form of the response, not the absolute value of the induced loss.

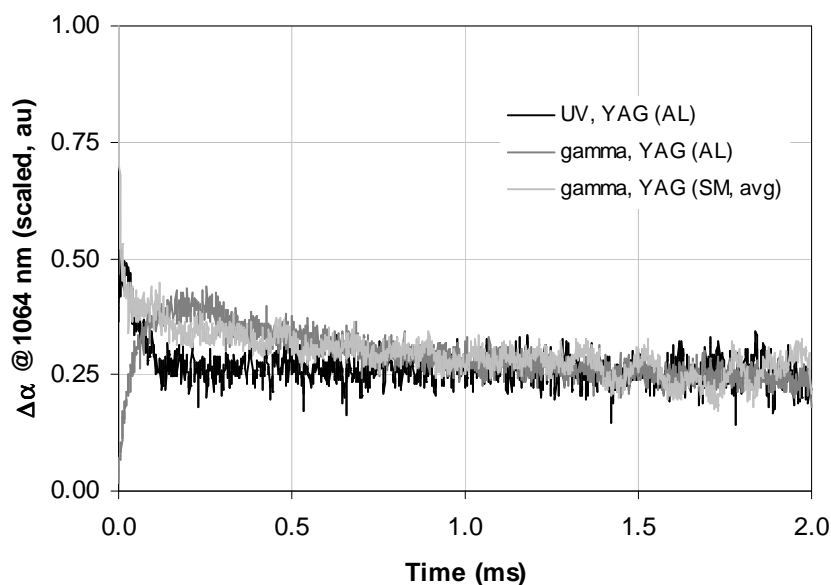


Figure 5.21. Relative comparison of UV and gamma transient induced absorption data. UV data, shown in black, is from the same sample Airtron-Litton sample as the gamma data shown in dark gray. Scientific Materials sample of average purity is shown in light gray.

As can be seen in Figure 5.4 of this chapter, the response of all tested UV-irradiated YAG samples was essentially the same in form, differing only in scale.

Therefore, only one of those samples is represented in Figure 5.20 above. The figure shows that past the first 0.5 ms after the irradiation, samples behaved in a very similar manner, irrespective of the source of ionizing radiation. Figure 5.22 below explores the differences on a shorter time scale.

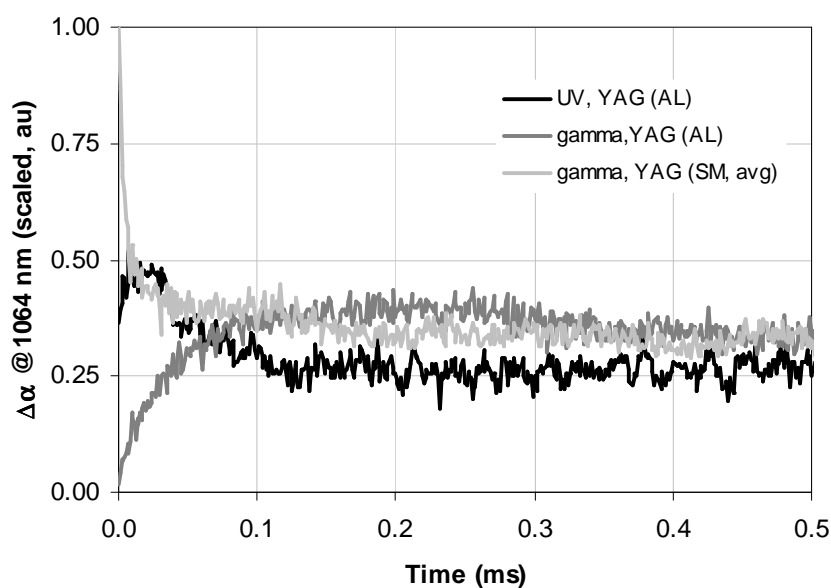


Figure 5.22. Samples and data set are the same as in Figure 5.21, but presented on a shorter time scale.

Differences in the absorption response to the two modes of irradiation are highlighted in Figure 5.22 above. The same Aitron-Litton (AL) sample was used to obtain the YAG (AL) in Figures 5.21 and 5.22, yet it is clear from these figures the transient induced-absorption behavior depends on the source of irradiation. It can be seen in the figure that the onset of the induced absorption was faster for the case of the UV irradiation of the Aitron-Litton samples. However, the onset of induced absorption in the Scientific Materials YAG samples in response to gamma radiation was significantly

faster still (shown as the light gray curve in Figures 5.21 and 5.22), suggesting that the state responsible for the fast absorption process (described in Chapter IV, Section 4.3.2) was not accessed by the UV irradiation in these samples.

Section 5.4.2.2

Nd:YAG

A similar comparison is here carried out for Nd:YAG samples. Figure 5.23 and 5.24 below compare data from the UV tests and gamma tests side-by-side. As no UV tests were performed on the Scientific Materials Nd:YAG samples, only samples from United Crystals (UC) are discussed in this Section. As discussed previously (Chapter IV, Section 4.3.2.2), response of Nd:YAG to pulsed gamma radiation could generally be broken down into three components: a fast absorption process (lifetime on the order of 10 μ s), a slow absorption process (lifetime on the order of 10 ms), and a gain process.

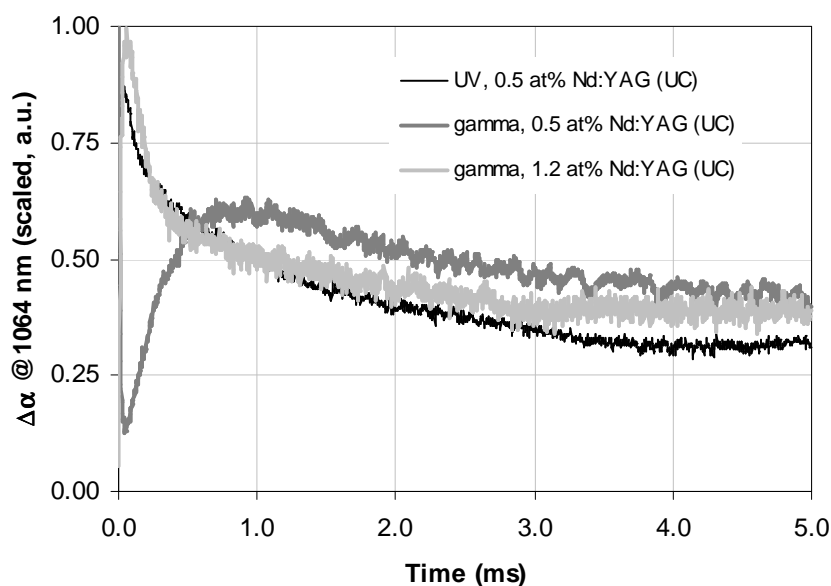


Figure 5.23. A side-by-side comparison of UV and gamma irradiation tests. Data were scaled and then normalized to appear on the same scale.

For the purpose of comparing the UV data to the gamma irradiation data, two gamma irradiation curves were chosen. The first, represented in Figure 5.23 by a light

gray curve, consisted of slow response only. The second, represented in Figure 5.23 by a dark gray curve, consisted of all three major components – fast absorption, slow absorption, and gain.

The first observation that is clear from Figure 5.23 is that a significant contribution of the gain process seen in the data from the gamma tests (represented by the dark gray 0.5 at% Nd:YAG (UC) curve in Figure 5.23) is absent from the UV test data. The UV-irradiated sample did not display a dip in induced absorption associated with a significant contribution of the ionizing-radiation-induced gain process.

Now compare the gamma test data from 1.2 at% Nd:YAG (the light gray in Figure 5.23) to the UV test data for 0.5 at% Nd:YAG (the black curve). A significant similarity between these curves can be clearly seen. In fact, the curves essentially overlap past approximately 0.25 ms for the two means of irradiation.

The two sets of data (UV and gamma irradiation) are further compared on a shorter time scale in Figure 5.24 below. The curve from the gamma test containing a gain contribution (the dark gray curve for 0.5 at% Nd:YAG) has been omitted, as its mode of behavior was absent from the UV data.

Figure 5.24 highlights the behavior of the different Nd:YAG samples near the event of irradiation. Examination of Figure 5.24 shows that all of the curves bear a generally similar character. They all display a delayed onset of induced absorption (reaching maximum absorption within 30-60 μ s), followed by a decay. The rates of decay also appear similar.

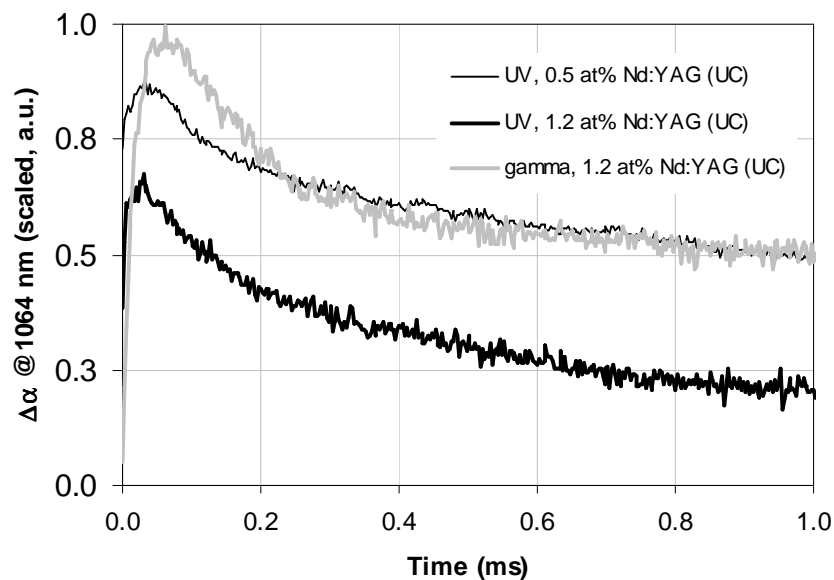


Figure 5.24. Same data as in Figure 5.23. A shorter time scale is used to highlight behavior near the irradiation event. Data for gamma irradiation of 0.5 at% Nd:YAG has been omitted from this figure.

As both UV irradiation response curves (black curves in Figures 5.23 and 5.24) have onset on the order of tens of microseconds, it is seen that the fast absorption process observed in the gamma radiation response data is largely absent from the UV test data.

Section 5.4.2.3*Cr³⁺:YAG*

No direct comparison could be made between UV and gamma irradiation data of Cr:YAG samples. However, an in-depth statistical analysis comparing the two data sets was carried, and is described in Section 5.3.2 of this Chapter.

Section 5.4.2.4

$Cr^{3+}, Nd:YAG$

Figure 5.25 below shows a side-by-side comparison of the transient response data for the co-doped samples from the UV and gamma irradiation experiments.

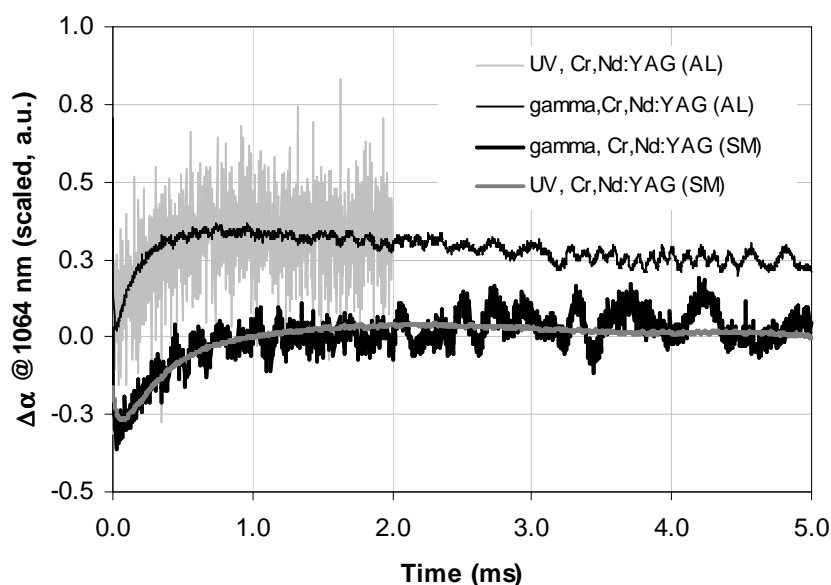


Figure 5.25. Comparison of transient response data for the co-doped samples, from two types of irradiation. The Airtron-Litton (AL) sample's composition was 0.13 at% Cr, 1.0 at% Nd:YAG. The Scientific Materials (SM) sample's composition was 1.0 at% Cr, 1.2 at% Nd:YAG.

Figure 5.25 clearly shows that the samples followed nearly identical patterns of behavior in both types of ionizing radiation. Co-doped samples containing a low concentration of chromium displayed a delayed onset of induced absorption. Co-doped samples with a high concentration of chromium exhibited signal gain, as well as perhaps a small amount of induced absorption.

Therefore, we can conclude that both types of ionizing radiation – gamma and UV – induced similar physical processes in the studied compositions.

Section 5.4.3

Comparison with HERMES III Permanent Data

Section 5.4.3.1

Undoped YAG and Nd:YAG

As differential absorption was calculated for both types of irradiation (Chapter IV, Sections 4.2.2 for gamma and Chapter V, Section 5.2.2 for UV), it is possible to compare these results side by side. A comparison of data for undoped YAG and for Nd:YAG is shown below in Figures 5.26 and 5.28.

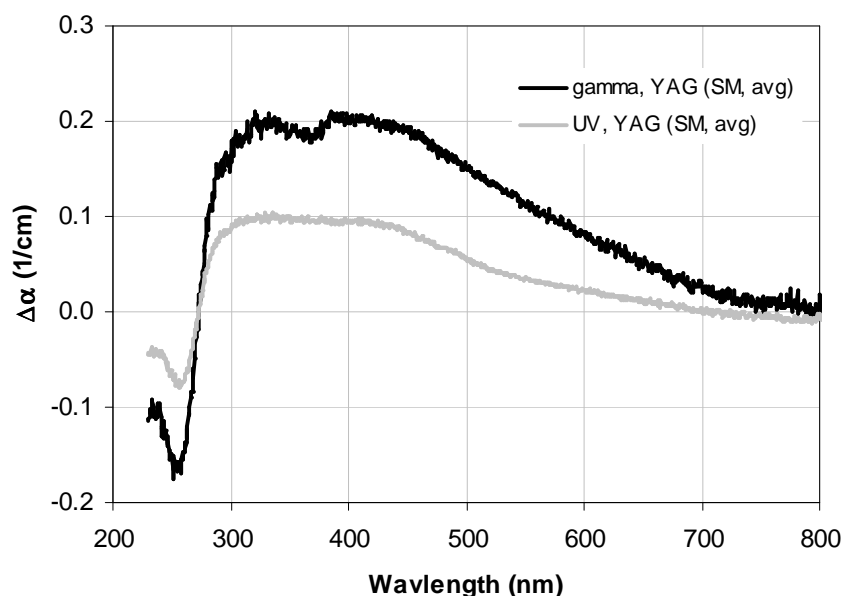


Figure 5.26. Comparison of room-temperature-stable differential absorption in undoped YAG due to gamma irradiation (the black curve) and UV (the light gray curve). Data used are from the Scientific Materials sample of average purity.

For this comparison, data from the gamma-irradiated YAG sample was shifted in the manner consistent with that described in Section 5.2.2.1 of this Chapter. Its curve was shifted so that it tends to zero near 800 nm. The two curves bear similar features (a

negative peak near 255 nm and a positive peak between 300 nm and 400 nm), suggesting that similar processes are induced in the materials by the two types of irradiation (UV and gamma).

It is further instructive to compare the amplitude of induced changes in the materials, and to compare these changes between the two modes of irradiation. This comparison was achieved by comparing the difference between the maximum of differential absorption and its minimum ($\Delta\alpha_{\max} - \Delta\alpha_{\min}$, effectively the peak-to-valley measure of differential absorption). This effectively combines the drop in concentration of Fe^{3+} with the increase in concentration of Fe^{2+} , and removes any ambiguity due to the changing vertical offsets. Furthermore, these results can be analyzed in the context of sample purity by graphing these values against the measured iron concentration. This analysis is presented below, in Figure 5.27.

A definite positive trend is observed in Figure 5.26, where induced changes are scaling with the iron concentration. This trend can be further analyzed by calculating the p-correlation between the concentration values and the peak-to-valley values of differential absorption (using Equation 4.7). For the case of gamma irradiation, this yields the correlation value of 0.771. For the case of UV irradiation, the correlation value is 0.995. While for the case of gamma irradiation the correlation is strongly positive, for the case of UV irradiation the relationship is almost exactly linear.

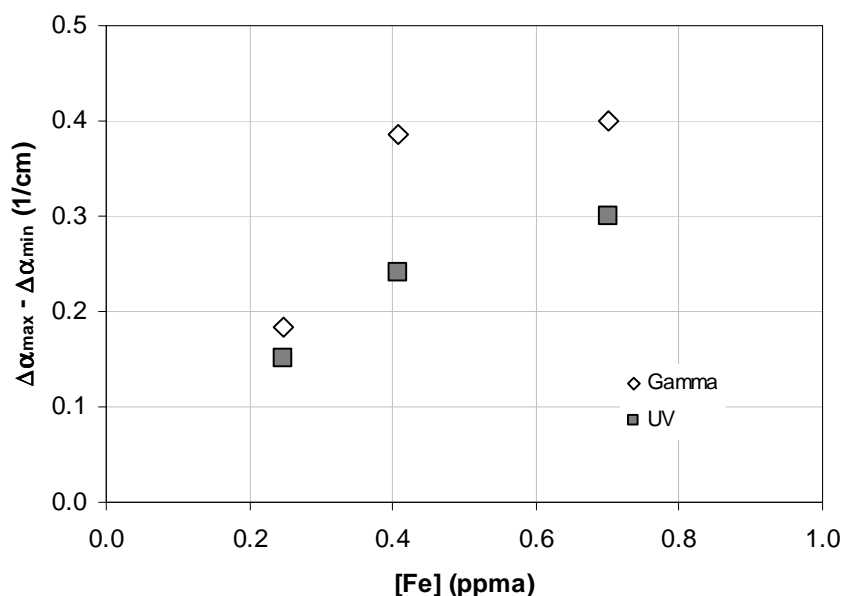


Figure 5.27. Comparison of the amplitude of induced permanent changes in undoped YAG samples, plotted against concentration of the iron impurity.

Figure 5.28 shows a side-by-side comparison of differential absorption in an undoped YAG sample from Scientific Materials. The same sample was used in both tests (with an anneal at 500 °C in between, relaxing the coloration induced by the gamma irradiation). As is clearly seen in Figure 5.28, both types of irradiation induce essentially the same type of band structure, different in amplitude but not in shape. Gamma radiation causes a greater extent of coloration when compared to UV irradiation. In both cases, there is a negative peak near 250 nm, and a broad positive peak with maximum amplitude between 300 nm and 400 nm, with its shoulder extending across the visible spectrum into the NIR.

In a manner mirroring the changes observed in undoped YAG, Nd:YAG samples follow a similar trend in both types of irradiation, gamma and UV. Again, differential

absorption consists of a negative peak near 250 nm, and a broad positive peak reaching its maximum value near 320 nm, and its shoulder extending toward the longer wavelengths across the visible and into the NIR. Again, for the same material, gamma irradiation has caused a greater extent of coloration than UV.

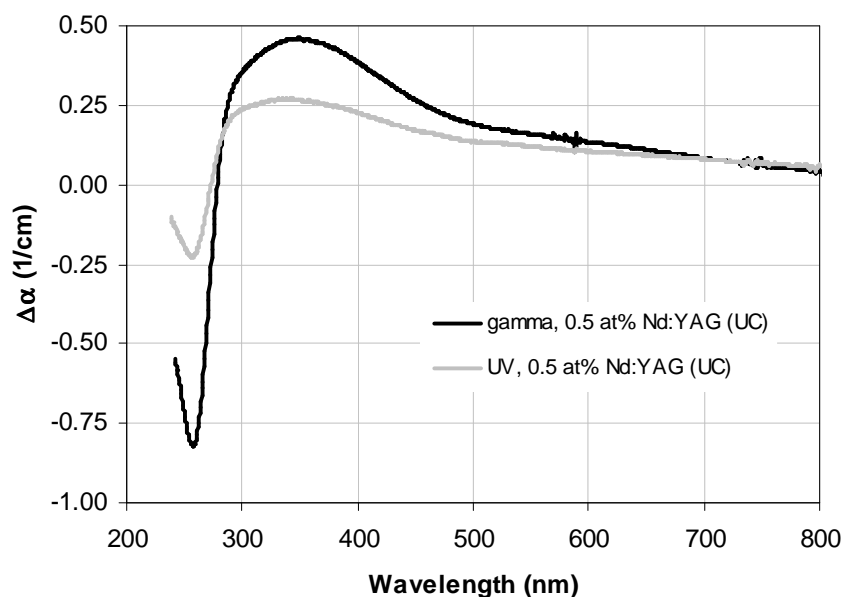


Figure 5.28. Comparison of room-temperature-stable differential absorption in Nd:YAG due to gamma irradiation (the black curve) and UV (the light gray curve). Data used are from the United Crystals samples doped with 0.5 at% Nd.

As the behavior of undoped YAG and Nd:YAG samples appears to follow the same trends under both UV and gamma, then attribution of the peaks shown earlier in Chapter IV, Section 4.4.2.2 can be applied to the UV data. Therefore, based on the available differential absorption data, the UV-induced coloration can be attributed to creation of the divalent iron color centers.

Section 5.4.3.2

Cr³⁺:YAG and Cr³⁺,Nd:YAG

No permanent changes in the optical absorption spectrum were observed in Cr:YAG and Cr,Nd:YAG samples. Based on regular differential absorption measurements carried out over a course of two days, Cr:YAG samples appeared to recover completely to their pre-irradiation state within 24-48 hours.

Anomalous absorption observed in some Cr,Nd:YAG samples that was ascribed to internal sample stresses (see Chapter IV, Section 4.2.2.4) could not be replicated under UV irradiation. Changes seen in the low-chromium co-doped samples appeared to be similar under both types of irradiation, again pointing to the fact that both types of ionizing radiation induced similar color center processes.

Section 5.5

Conclusions

The experimental sample suite was subjected to a series of tests exposing these materials to UV irradiation in the form of pulsed radiation at 248 nm. These tests consisted of measuring transient absorption at 1064 nm (in a manner similar to the tests conducted at HERMES III), as well as observing differential absorption induced in these materials by the UV radiation.

Observations of the transient absorption revealed a behavior that bore significant similarities to that observed in the same materials in response to pulsed gamma irradiation at HERMES III. The responses of undoped YAG and Nd:YAG to pulsed UV generally exhibited that slow absorption process that was similarly identified in the same materials under gamma irradiation. This process had a finite onset of absorption, with relaxation times on the order of 10 ms, annealing nearly completely at room temperature. Neither the fast absorption process (lifetime on the order of 10 μ s) nor the gain process were seen in the Nd:YAG samples under UV irradiation.

The transient absorption measurements on Cr,Nd:YAG also yielded results similar to the HERMES III tests. High-chromium co-doped samples showed gain along with a small amount of absorption. The low-chromium samples displayed a small amount of induced absorption.

Observations of differential absorption showed trends also very similar to those observed in the gamma-irradiation data. Under both types of irradiation, undoped YAG

and Nd:YAG samples displayed changes in absorption consistent with a valence change of the iron impurity, creating the divalent iron color centers.

In all of the above cases, the amplitude of changes induced in these materials was lower for the case of the UV irradiation when compared to the results of the gamma tests.

In a series of differential absorption measurements performed on the chromium-bearing samples, photoionization of the octahedral Cr^{3+} ions was identified. With the exception of the low-chromium co-doped sample from Airtron-Litton, the Cr^{4+} state is unstable at room temperature.

Two conclusions can be drawn from these observations. The first is that the samples bearing at least 0.5 at% of Cr^{3+} have resisted the formation of color centers under the influence of pulsed UV radiation. Their radiation hardness with respect to UV radiation is improved compared to the samples in the experimental suite that did not contain at least 0.5 at% of Cr^{3+} .

The second conclusion is that to some extent there is a similarity between the two sets of data – gamma data from HERMES III and the UV test data. Both transient and permanent data suggest that the two types of irradiation access some similar groups of defect states and color centers, across several compositions, purity levels, and material manufacturers. In particular, steady-state and slowly-decaying color center formation appears to be strongly correlated across irradiation methods. Fast-decaying processes, attributed to gamma-excited defects in the host crystal (and not arising from impurities) in Chapter 4, do not appear to be active under UV illumination. This strongly suggests that pulsed UV tests can be used to simulate some of the effects of gamma radiation on

this family of materials. While the experimental results have not been perfectly replicated between the two sets of experiments, a strong qualitative correlation is nonetheless observed.

Therefore, it may be possible to use the types of UV exposures described in this chapter to pre-qualify particular materials for radiation exposures as described in Chapter IV. The advantage of this approach is that UV testing – which is safer, less expensive, and more accessible than gamma radiation testing – can be used to reduce the number of materials that needs to be subjected to the actual gamma radiation tests.

Chapter 6 - Conclusions

Chapter Summary

The previous chapters have provided an overview of the experimental data collected over the course of this study, along with a physical interpretation of these observations. Set in context of the existing prior research, this report's observations have pointed to activity of specific ions and defects within the YAG material system.

Furthermore, through a side-by-side comparison of several compositions, a radiation-hard material was identified. In this composition, the effects of both UV and gamma radiation were greatly reduced when compared to the more standard compositions being used today.

Based on these identifications, this chapter aims to offer a hypothesis explaining the improved radiation hardness phenomenon observed in some compositions.

Section 6.1

Summary and Review of Results

The action of the ionizing radiation on the undoped YAG and Nd:YAG materials appears adequately described by previous research (Mori 1977, Akhmadulin 1992) in the following way. The electrons excited by the ionizing radiation are transferred to a fixed variety of trap states, which generally fall into two groups – those stable and unstable at room temperature.

The unstable trap states appear to consist of oxygen vacancies capturing excited electrons, resulting in F and F^+ color centers. Their annealing thresholds are reported to be between 140 K and 210 K, well below room temperature. Therefore, their lifetime at room temperature must be limited.

The stable group is dominated by the iron impurity, which can capture excited electrons. These traps have a much higher annealing temperature (at least 200 degrees above room temperature). Due to their high annealing temperature, the divalent iron color centers persist at room temperature.

It is possible that the unstable traps act as an intermediate feeder state for the stable traps. As suggested by data presented by Bernhardt 1976, and claimed by Mori 1977, the majority of trapped electrons are first captured by the unstable F centers, and as these centers relax, some of the electrons are intercepted by deeper traps (such as the trivalent iron impurity).

In contrast to the undoped YAG and Nd:YAG materials, neither group of these color centers appears to be active in the materials containing significant amounts of

chromium. In the materials studied – which contained at least 0.13 at% Cr – the dominant color center process was further ionization of chromium. Even though iron was present in approximately the same quantities as in non-chromium-bearing samples (see data in Chapter III, Section 3.3.2), no changes in its valence state were detected and a concurrent gamma-radiation hardened optical response was observed.

Section 6.2

Proposed Mechanism of Radiation Hardness

The presence of chromium appears to prevent the formation of both the oxygen vacancy traps and the divalent iron color centers. It is clear from the mass spectroscopy data that chromium does not prevent the incorporation of iron into the YAG lattice, as iron was found present in roughly the same quantities in all materials tested regardless of chromium co-doping. The concentration of oxygen vacancies could not be readily verified using the available techniques and equipment.

Since oxygen vacancies likely play the initiating role in the formation of color centers in YAG, it is reasonable to examine their impact on the ultimate radiation sensitivity of the samples. Specifically, anion vacancies are formed during the crystal growth. While their concentration is increased if the crystal is grown under reducing conditions (such as vacuum or nitrogen), which is a common condition in industrial growth techniques of YAG crystals, a small concentration will remain even if grown under ideal stoichiometric conditions.

A further way in which the oxygen vacancy concentration can be increased is through the incorporation of di- and monovalent impurities during crystal growth. Since every cation site in YAG requires a trivalent species, some form of charge compensation is needed for the cases when the substitutional cation impurity itself cannot provide the three electrons. This is the case with alkali group elements, most notably calcium, magnesium, potassium, and sodium. All of these have been identified in nearly all the

samples studied using mass spectroscopy, in concentrations near or exceeding that of iron (see Chapter III, Section 3.3.2).

In the absence of a tetravalent impurity that can act as a charge compensator (in garnets, this role is commonly filled by silicon), an oxygen vacancy attaches to the hypovalent impurity. Thus it follows that the presence of hypovalent impurities, such as elements from the alkali group, would likely increase the concentration of oxygen vacancies.

It is known that chromium can act as a charge compensator, and in fact has been observed to function in this role in the presence of calcium and magnesium by assuming a permanent tetravalent state. It is, therefore, reasonable that the addition of chromium to the base crystalline material can, in effect, passivate some of the hypovalent impurities by providing the extra charge, and removing the need for an oxygen vacancy. In this way, the presence of chromium can combat the formation of oxygen vacancies in the YAG lattice.

It should be noted that even though chromium can act as a charge compensator for some hypovalent species, it does not act in this capacity for iron. Peaks attributed to trivalent iron are still present in chromium-bearing samples. Therefore, iron remains in the trivalent state even in the presence of chromium.

In addition to blocking the F centers, this blocks a possible pathway to creating the Fe^{2+} centers (under Mori's description). However, if the pathway utilizing the F centers is not a unique way of creating the Fe^{2+} centers (as suggested by Akhmadulin, for example), then another mechanism needs to be identified.

An alternative model to the intermediate-step description of formation of the Fe^{2+} centers, just described, is the direct ligand transfer model. In this case, the electron being captured by the iron impurity comes from one of its coordinating oxygen ions. The presence or absence of oxygen vacancies elsewhere in the lattice should not significantly affect this alternate process.

As described previously, trivalent chromium exclusively occupies octahedral sites, whereas trivalent iron can occupy both octahedral and tetrahedral sites (Table 2.1 in Chapter II, Section 2.1). As claimed by Akhmadulin, the divalent iron color center can only exist in the octahedral sites. It is possible that chromium forces iron into tetrahedral sites. In this site, iron cannot form the permanent divalent iron color center. This site exclusion mechanism would prevent formation of the divalent iron color center regardless of how an electron would ordinarily be transferred to the iron impurity.

To summarize, there are two possible mechanisms in which presence of chromium improves YAG's radiation resistance – charge compensation of hypovalent impurities and site exclusion of iron. In the first mechanism, chromium acts as a charge compensator for hypovalent impurities (such as Ca^{2+} and Mg^{2+}), preventing the formation of oxygen vacancies near those sites. This prevents the formation of F -type centers, and also blocks a possible pathway for activation of the divalent iron color centers. In the second mechanism, chromium forces the iron ions to occupy mostly the tetrahedral sites, which cannot accommodate the divalent iron ions.

Overall radiation hardness provided by co-doping YAG with chromium likely relies on both of these mechanisms. If only the first mechanism applied, then the divalent

iron color centers could still form through ligand transfer. However, formation of the divalent iron color centers was not observed in any of the samples doped with chromium. If only the second mechanism applied, then *F*-type centers could still form, yielding some transient loss of transmission. While some loss of transient absorption is observed in chromium-bearing samples, it is attributed to the photoionization of the Cr^{3+} ions. Lifetimes of these color centers are orders of magnitude longer than those observed for non-chromium-bearing samples, suggesting a process physically distinct from the *F*-type color center activity.

While it has been observed that the extent of radiation hardness depends on the concentration of the chromium dopant, currently available data do not allow a precise analysis of this relationship. Samples containing 0.5 at% of Cr^{3+} or more are essentially radiation-hardened. The sole sample containing 0.13 at% Cr^{3+} has improved performance, but still shows significant degradation. The available points form a relationship that is binary, and therefore a trend cannot be extracted from it. While it is likely the functional radiation hardness threshold lies somewhere between 0.13 at% and 0.5 at%, it is presently not possible to ascertain precisely what it may be.

Section 6.3

Future Work

While the progress in this report has been sufficient to provide significant insights into the issue of radiation hardness in YAG-based materials, several questions remain to be addressed. Answers to these questions may refine the picture of color center formation and prevention. Some of possible extensions of the current work are described below.

Some of the measurements, specifically mass-spectroscopy-based composition analysis (as described in Chapter III) and UV-based testing (as described in Chapter V) should be extended to cover more samples in the experimental suite. As it currently stands, only a single sample from some compositions has been tested. Further tests could provide information on the distribution of compositional impurities and UV response behavior modes.

The connection to *F*-type color centers is presently based on correlations, not direct experimental evidence. A more direct connection could be provided by spectrally resolving the absorption associated with the transient absorption in YAG and Nd:YAG samples. Since the lifetimes of the transient absorption processes at room temperature are at least in the tens of microseconds, such an experiment should be feasible. It could rely on a white light source and a grating-CCD spectrometer using gated data collection, where the collection window would be synchronized with the excitation pulse.

It has also been claimed that formation of oxygen vacancies is at least partially due to presence of the *Ca* and *Mg* ions. This connection should be explored more quantitatively by examining a series of samples with controlled low levels of doping of

these elements. If a means of detecting vacancies directly is not available, simply repeating in-situ experiments (with either gamma or UV) should reveal the possible connection. If the claims made in the preceding chapters hold, then an increase in concentration of these elements should increase the amplitude of the transient absorption.

Another issue that may be addressed through additional experiments is dependence of the Fe^{2+} color center formation on the excitation wavelength. Since photo-bleaching of these color centers is possible, the balance of the Fe ions that re-charges may depend on the excitation wavelength. This may also provide insights on using light of certain wavelengths for relaxation of color centers formed in YAG materials that are not radiation-hardened.

Section 6.4

Report Summary and Conclusions

In this report, a family of materials – single-crystal YAG, Nd:YAG, Cr³⁺:YAG, and Cr³⁺,Nd:YAG – were tested in pulsed ionizing radiation environments (gamma and UV). Their response of these tests were measured in terms of instantaneous transient absorption at 1064 nm and steady-state differential absorption tracking changes across the UV, visible, and NIR parts of the optical spectrum.

In these tests, it was observed that undoped YAG and Nd:YAG experience the greatest extent of induced color center activity. The transient absorption was largely attributed to *F*-type color center activity, which consists of unstable charge traps where an electron is captured by an oxygen vacancy. The permanent changes in absorption were attributed to formation of the divalent iron color centers.

The chromium-bearing samples largely resisted formation of both of these types of color centers. Only the samples with the lowest chromium content formed color centers that were at all stable at room temperature. The rest of the chromium-bearing samples recovered their original absorption characteristics within 24-48 hours. Furthermore, the absorption induced in these samples was attributed to photoionization of the Cr³⁺ ions, forming the color centers. Therefore, the original thesis that addition of chromium can yield a radiation-hard YAG-based material appears largely supported by the experimental observations.

The significantly improved radiation resistance of these materials is attributed to trivalent chromium doping. It is suggested that chromium blocks formation of common

color centers by passivating divalent impurities (such as Ca^{2+} and Mg^{2+}) by donating an extra electron to those sites and further restricting the iron impurity to exclusively occupy tetrahedral sites.

The charge compensation mechanism prevents formation of oxygen vacancies, which blocks formation of *F*-type color centers. The site restriction of iron blocks formation of the divalent iron color centers because only iron in octahedral sites can trap electrons, as suggested by previous researchers (Akhmadulin et al. 1992).

Furthermore, these tests revealed extensive correlation between test results from the two environments. The types of color centers – both transient and permanent – accessed by the two types of radiation were largely similar. This provides a technique for pre-qualifying modified Nd:YAG materials for authentic radiation-effects testing that is cheaper, more accessible, and involves fewer hazards.

Overall, this research confirmed that co-doping Nd:YAG with Cr^{3+} improves the material's resistance to ionizing radiation. Furthermore, a model explaining the radiation-hardening action of Cr^{3+} co-doping has been proposed.

REFERENCES

- I.Sh. Akhmadullin, S.A. Migachev, S.P. Mironov (1992). “*Thermo- and photoinduced defects in $Y_3Al_5O_{12}$* ,” Nuclear Instruments and Methods in Physics Research B, v65, p270.
- I. Akhmadulin, V. Golenischev-Kutuzov, S. Migachev, M. Korzhik (1993). “*Investigation of the substitutional Fe^{2+} center in $Y_3Al_5O_{12}$ by acoustic EPR*,” Journal of Physics and Chemistry of Solids, v54, p117.
- R.B. Allen, S.J. Scalise (1969). “*Continuous operation of a YAlG:Nd laser by injection luminescent pumping*,” Applied Physics Letters, v7, p127.
- J.A. Anderson (1907). “*Absorption and emission spectra of neodymium and erbium compounds*,” Astrophysical Journal, v26, n2, p73.
- C.M. Barshik (2000). “*Glow discharge mass spectroscopy*,” in “*Inorganic mass spectroscopy: fundamental and applications*,” ed. C.M. Barshik, D.C. Duckworth, D.H. Smith. New York: Marcel Dekker.
- M. Bass, A.E. Paladino (1967). “*Color centers in Yttrium Gallium Garnet and Yttrium Aluminum Garnet*,” Journal of Applied Physics, v38, p2706.
- Hj. Bernhardt (1974). “*On the coloration behaviour of undoped YAlO₃ crystals*,” Physica Status Solidi (a), v21, n1, p95.
- Hj. Bernhardt (1976). “*Comparative studies of the LNT coloration of $Y_3Al_5O_{12}$, YAlO₃, and LiNbO₃ crystals*,” Physica Status Solidi (a), v33, p211.
- Hj. Bernhardt (1980). “*Investigations on the thermoluminescence of x-rayed YAG crystals*,” Physica Status Solidi (a), v61, n2, p357.

- Bertaut, Forrat (1956). *Comptes Rendus*, v242, p382.
- Bertaut, Forrat (1957). *Journal de Physique et Le Radium*, v18, p305.
- K. Čermák, A. Linka (1981). “*Transient colour centre in YAG:Nd*,” *Czechoslovak Journal of Physics*, v31, p652.
- K. Chakrabarti (1988). “*Photobleaching and photoluminescence in neutron-irradiated YAG*,” *Journal of Physics and Chemistry of Solids*, v49, n9, p1009.
- S.S. Cristy (2000). “*Secondary Ion Mass Spectroscopy*,” in “*Inorganic mass spectroscopy: fundamental and applications*,” ed. C.M. Barshik, D.C. Duckworth, D.H. Smith. New York: Marcel Dekker.
- D.M.J. Compton, R.A. Cesena (1967). “*Mechanisms of radiation effects on lasers*,” *IEEE Transactions on Nuclear Science*, v14, p55.
- Die Dong, Kuang Xiao-Yu, Guo Jian-Jun, Wang hui, Zhou Kang-Wei (2005). “*Optical absorption and EPR study of the octahedral Fe^{3+} center in yttrium aluminum garnet*,” *Physical Review B*, v72 p073101.
- F. Euler, J.A. Bruce (1965). “*Oxygen coordinates of compounds with garnet structure*,” *Acta Crystallographica*, v19, p971.
- B.R. Frieden (2001). *Probability, Statistical Optics, and Data Testing*, 3rd edition. Springer.
- J.E. Geusic, H.M. Marcos, L.G. Van Uitert (1964). “*Laser oscillations in Nd-doped yttrium aluminum, yttrium gallium and gadolinium garnets*,” *Applied Physics Letters*, v4, n10, p182.

- M.A. Gilleo, S. Geller (1957). "*Structure and ferrimagnetism of yttrium and rare-earth-iron garnets,*" Acta Crystallographica, v10, p239.
- M.A. Gilleo, S. Geller (1958). "*Substitution of Iron in Ferrimagnetic Yttrium-Iron Garnet,*" Journal of Applied Physics, v29, n3, p380.
- W. Heitmann, A. Moeller, G.V. Schultz (1964). "*Fluorescence of Nd($4f^3$) by irradiation into the chromium absorption bands of the system $Al_2O_3:Cr, Nd,$ " Physics Letters, v10, n1, p26.*
- International Tables for Crystallography.* Hahn, Theo; Shmueli, U.; Wilson, A.J.C. Kluwer Academic Publishing Group (1984).
- L.F. Johnson, G.D. Boyd, K. Nassau, R.R. Soden (1962). "*Continuous operation of a solid-state optical maser,*" Physical Review, v126, p1406.
- B.R. Judd (1959). "*An analysis of the fluorescence spectrum of neodymium chloride,*" Proceedings of the Royal Society of London A, v251, n1264, p134.
- B.R. Judd (1962). "*Optical absorption intensities of rare-earth ions,*" Physical Review, v127, n3, p750.
- S.M. Kaczmarek, R. Jablonski, Z. Moroz, I. Pracka, T. Lukasiewicz (1999). "*Radiation defects in oxide compounds,*" Crystal Research and Technology, v34, p1183.
- L.G. Karaseva, N.Yu. Konstantinov, V.V. Gromov (1985). "*Nature of radiation colour centers in single crystals of yttrium aluminum garnet,*" Radiation Physics and Chemistry, v26, n6, p723.
- A.S. King (1933). "*Temperature classification of the spectrum of neodymium,*" Astrophysical Journal, v78, p9.

- Z.J. Kiss, R.C. Duncan (1964). "Cross-pumped Cr^{3+} - Nd^{3+} :YAG laser system," Applied Physics Letters, v5, p200.
- J.A. Koningstein, J.E. Geusic (1964). "Energy levels and crystal-field calculations of Neodymium in yttrium aluminum garnet," Physical Review, v136, p711.
- R.A. Lefever, A.B. Chase (1960). "Substitutional incorporation of divalent iron in yttrium iron garnet," Journal of Chemical Physics, v32 n5 p1575.
- R.A. Lefever, J.W. Torpy, A.B. Chase (1961). "Growth of single crystals of yttrium aluminum garnet from lead oxide-lead fluoride melt," Journal of Applied Physics, v32, p962.
- R.C. Linares (1962). "Growth of yttrium-aluminum garnet single crystals," Journal of the American Ceramics Society, v45, n3, p119.
- A.O. Matkovskii, D.Yu. Sugak, A.N. Durygin, S. Kaczmarek, K. Kopczynski, Z. Mierczyk, Z. Frukacz, T. Klasiewicz, A.P. Shakov (1996). "Effect of ionizing radiation on optical and lasing properties of $Y_3Al_5O_{12}$ single crystals doped with Nd, Er, Ho, Tm, Cr ions," Optical Materials, v6, p353.
- A. Matkovskii, D. Sugak, S. Melnyk, P. Potera, A. Suchocki, Z. Frukacz (2000). "Colour centers in doped $Gd_3Ga_5O_{12}$ and $Y_3Al_5O_{12}$ laser crystals," Journal of Alloys and Compounds, v300-301, p395.
- K. Mori (1973). "Detection of transient absorption in YAG laser crystals using combined laser," Japanese Journal of Applied Physics, v12, n2, p325.
- K. Mori (1977). "Transient colour centres caused by UV light irradiation in yttrium aluminium garnet crystals," Physica Status Solidi (a), v42, n1, p375.

- J. Murphy, R.C. Ohlmann, R. Mazelsky (1964). “*Energy transfer from 3d to 4f electrons in LaAlO₃:Cr, Nd,*” Physical Review Letters, v13, n4, p135.
- F.W. Paul (1936). “*Absorption spectra of cerium, neodymium and samarium,*” Physical Review, v49, p156.
- Juan J. Ramirez, K.R. Prestwich, D.L. Johnson, J.P. Corley, G.J. Denison, J.A. Alexander, T.L. Franklin, P.J. Pankuch, T.W.L. Sanford, T.J. Sheridan, L.L. Torrison, G.A. Zawadzkas (1989). “*Performance of the Hermes-III gamma ray simulator,*” IEEE Pulsed Power Conference 1989, v7, p26.
- T.S. Rose, M.S. Hopkins, R.A. Fields (1995). “*Characterization and control of gamma and proton radiation effects on the performance of Nd:YAG and Nd:YLF lasers,*” IEEE Journal of Quantum Electronics, v31, p1593.
- R.D. Shannon, C.T. Prewitt (1969). “*Effective ionic radii in oxides and fluorides,*” Acta Crystallographica B, v25, p925.
- J. Singleton (2006). *Band theory and electronic properties of solids*, Oxford University Press.
- Joseph R. Smyth (2001). *Mineral structure data – garnet*. University of Colorado. <http://ruby.colorado.edu/~smyth/min/garnet.html>. Accessed on December 3rd, 2010.
- E. Snitzer (1961). “*Optical maser action of Nd³⁺ in a barium crown glass,*” Physical Review Letters, v7, n12, p444.

- A. Vedda, D. Di Martino, M. Martini, J. Mares, E. Mihokova, M. Nikl, N. Solovieva, K. Blazek, K. Nejezchleb (2004). "Trap levels in Y-aluminum garnet scintillating crystals," *Radiation Measurements*, v38, p673.
- K.A. Wickersheim, R.L. White (1960). "Optical observation of exchange splitting in ytterbium iron garnet," *Physical Review Letters*, v4, n3, p123.
- J.B. Willis and M. Dixon (1968). "Assessment and control of imperfections in crystals for laser devices," *Journal of Crystal Growth*, v3,4, p236.
- D.L. Wood, J. Ferguson, K. Knox, J.F. Dillion, Jr. (1963). "Crystal-field spectra of $d^{3,7}$ ions. III. Spectrum of Cr^{3+} in various octahedral crystal fields," *Journal of Chemical Physics*, v39, p890.
- H.S. Yoder, M.L. Keith (1951). "Complete substitution of aluminum for silicon: the system $3MnO \cdot Al_2O_3 \cdot 3SiO_2 - 3Y_2O_3 \cdot 5Al_2O_3$," *American Mineralogist*, v36, p519.
- G. Zeidler (1968). "Pump-powered-dependent efficiency in a YAG: Na^{3+} laser," *IEEE Journal of Quantum Electronics*, v4, n12, p1016.